ANNUAL REPORT 2000

Optoelectronics Department

University of Ulm

Contents

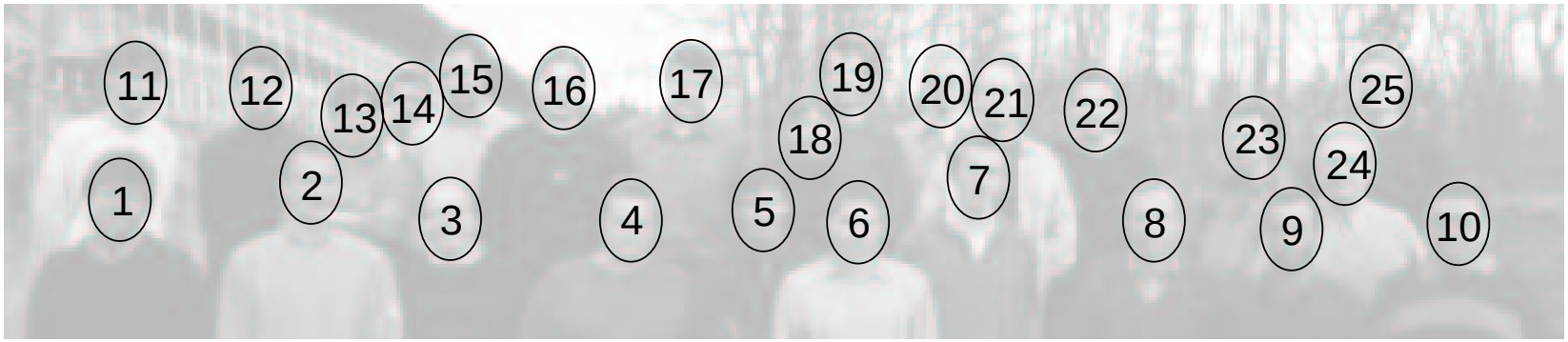

1: Peter Unger
2: Matthias Golling
3: Jürgen Joos
4: Marcus Scherer
5: Felix Mederer
6: Thomas Knödl
7: Rainer Michalzik
8: Karl J. Ebeling
9: Safwat W.Z. Mahmoud
10: Josef Theisz
11: Roland Jäger
12: Eckart Schiehlen
13: Christine Bunk
14: Max Kicherer
15: Roger King
16: Frank Demaria
17: Manfred Mundbrod
18: Irene Ecker
19: Michael Miller
20: Matthias Seyboth
21: Heiko J. Unold
22: Sven S. Schad
23: Ulrich Martin
24: Georgi Stareev
25: Michael C. Riedl

Missing in the picture

26: Rainer Blood
27: Eckard Deichsel
28: Susanne Döttinger
29: Martin Grabherr
30: Markus Kamp
31: Sükran Kilic
32: Jürgen Mähnß
33: Gerlinde Meixner
34: Susanne Menzel
35: Sophie Pfetsch
36: Wolfgang Schmid
37: Veit Schwegler
38: Dieter Wiedenmann

Optoelectronics Department
University of Ulm

Albert-Einstein-Allee 45, D-89069 Ulm, Germany
Fax: +49–731/50–2 60 49
Phone: +49–731/50–

Head of Department

Prof. Dr.	Karl Joachim Ebeling	–2 60 51	karl.ebeling@e-technik.uni-ulm.de

Assistant Head of Department

Prof. Dr.	Peter Unger	–2 60 54	peter.unger@e-technik.uni-ulm.de

Senior Research Assistant

Dr.-Ing.	Rainer Michalzik	–2 60 48	rainer.michalzik@e-technik.uni-ulm.de

Cleanroom Management

Dr.-Ing.	Jürgen Mähnß	–2 60 53	juergen.maehnss@e-technik.uni-ulm.de

Secretaries

	Christine Bunk	–2 60 50	christine.bunk@e-technik.uni-ulm.de
	Sükran Kilic	–2 60 59	suekran.kilic@e-technik.uni-ulm.de

Research Staff

Dipl.-Ing.	Eckard Deichsel	–2 60 57	eckard.deichsel@e-technik.uni-ulm.de
Dipl.-Phys.	Frank Demaria	–2 60 46	frank.demaria@e-technik.uni-ulm.de
Dipl.-Ing.	Irene Ecker	–2 60 41	irene.ecker@e-technik.uni-ulm.de
Dipl.-Ing.	Mattias Golling	–2 60 35	matthias.golling@e-technik.uni-ulm.de
Dr.-Ing.	Martin Grabherr	–2 60 43	martin.grabherr@e-technik.uni-ulm.de
Dipl.-Phys.	Roland Jäger	–2 60 40	roland.jaeger@e-technik.uni-ulm.de
Dipl.-Ing.	Jürgen Joos	–2 60 35	juergen.joos@e-technik.uni-ulm.de
Dr.rer.nat.	Markus Kamp	–2 64 54	markus.kamp@e-technik.uni-ulm.de
Dipl.-Phys.	Max Kicherer	–2 60 37	max.kicherer@e-technik.uni-ulm.de
Dipl.-Ing.	Roger King	–2 60 40	roger.king@e-technik.uni-ulm.de
Dipl.-Ing.	Christoph Kirchner	–2 64 54	christoph.kirchner@e-technik.uni-ulm.de
Dipl.-Ing.	Thomas Knödl	–2 60 38	thomas.knoedl@e-technik.uni-ulm.de
M.S.	Safwat W.Z. Mahmoud	–2 60 44	safwat.mahmoud@e-technik.uni-ulm.de
Dipl.-Ing.	Ulrich Martin	–2 60 46	ulrich.martin@e-technik.uni-ulm.de
Dipl.-Ing.	Felix Mederer	–2 60 37	felix.mederer@e-technik.uni-ulm.de
Dipl.-Phys.	Michael Miller	–2 60 36	michael.miller@e-technik.uni-ulm.de
Dipl.-Phys.	Manfred Mundbrod	–2 60 39	manfred.mundbrod@e-technik.uni-ulm.de
Dipl.-Ing.	Michael C. Riedl	–2 60 36	michael.riedl@e-technik.uni-ulm.de
Dipl.-Ing.	Sven-Silvius Schad	–2 61 95	sven-silvius.schad@e-technik.uni-ulm.de
Dipl.-Ing.	Marcus Scherer	–2 61 95	marcus.scherer@e-technik.uni-ulm.de
Dipl.-Ing.	Eckart Schiehlen	–2 60 57	eckart.schiehlen@e-technik.uni-ulm.de
Dipl.-Ing.	Wolfgang Schmid	–2 60 44	wolfgang.schmid@e-technik.uni-ulm.de
Dipl.-Ing.	Veit Schwegler	–2 64 52	veit.schwegler@e-technik.uni-ulm.de
Dipl.-Phys.	Matthias Seyboth	–2 64 52	matthias.seyboth@e-technik.uni-ulm.de
Dr.-Ing.	Georgi Stareev	–2 61 98	georgi.stareev@e-technik.uni-ulm.de
Dipl.-Ing.	Heiko J. Unold	–2 60 36	heiko.unold@e-technik.uni-ulm.de
Dr.-Ing.	Dieter Wiedenmann	–2 60 43	dieter.wiedenmann@e-technik.uni-ulm.de

Technical Staff

Rainer Blood	–2 60 44	rainer.blood@e-technik.uni-ulm.de
Susanne Döttinger	–2 60 38	susanne.doettinger@e-technik.uni-ulm.de
Susanne Menzel	–2 60 41	susanne.menzel@e-technik.uni-ulm.de
Gerlinde Meixner	–2 60 41	gerlinde.meixner@e-technik.uni-ulm.de
Sophie Pfetsch	–2 60 41	sophie.pfetsch@e-technik.uni-ulm.de
Josef Theisz	–2 60 30	josef.theisz@e-technik.uni-ulm.de
Hansjörg Wolf	–2 60 43	hansjoerg.wolf@e-technik.uni-ulm.de

Preface

The Millennium Year 2000 has been another spectacular one for the Department of Optoelectronics. Research still concentrated on high power laser diodes, GaN based electronic and optoelectronic devices, vertical-cavity surface-emitting laser diodes (VCSELs), and high-speed optical data transmission in optical interconnects. Remarkable progress has been achieved including above 50 % external quantum efficiency LEDs, optically pumped vertical external cavity surface emitting lasers (VECSELs) with high quality beam profiles, surface relief and extended cavity single-mode VCSELs, record high 900 mW broad area VCSELs as well as world's first room temperature continuous wave diode cascade VCSEL with more than 100 % quantum efficiency. Moreover, in a fruitful collaboration with the Department of Electronic Devices and Circuits successful operation of InGaN-GaN FETs was demonstrated for the first time.

In early spring, Prof. Selim Ünlü from Boston University joined the GaN group as a distinguished Guest Professor for almost six months. We all appreciated his most valuable seminar talks and his outstanding support in this extremely useful cooperation. We now miss exciting discussions with Selim and his critical comments on our way of doing research. We are grateful that in the fall Veit Schwegler had a chance to spend about two months in Selim's lab in Boston working on time resolved spectroscopy. In September, Prof. Larry Coldren from the University of California at Santa Barbara visited us. He gave an exciting talk on VCSEL activities in his group and we had a good time extensively discussing VCSEL future demands and prospects.

As always, we had major changes in our staff. Rainer Michalzik returned from a one year absence spent at Lucent Bell Laboratories. In May after 10 years of service in our Department Sophie Pfetsch retired from her regular duties. We certainly miss her kind help and warm personality but are happy that she continues in a one day per week part time job. Gerlinde Meixner and Rainer Blood took over technical positions being involved in, respectively, art work and processing and packaging technology. After having spent about one year at German Aerospace Dieter Wiedenmann rejoined the Department to strengthen our VCSEL activities.

Markus Kamp, having established our strong and successful GaN group, submitted his habilitation thesis and finally left us for starting a career in industry. Peter Schnitzer, Markus Mayer, Günter Jost, Martin Grabherr and in an external cooperation Stefan Morgott received their Ph.D. degrees in Electrical Engineering. All of them were employed in established companies or startups when they passed their Ph.D. examination. Moreover, we had three diploma theses and three semester projects completed.

At Photonics West 2000 a group with Christian Jung and Heiko Unold as the first author and presenter received the best paper award for their work on high performance VCSEL arrays. Dieter Wiedenmann received the Prize of the Ulmer Universitätsgesellschaft for

his Ph.D. thesis on the dynamics and noise properties of VCSELs. Martin Grabherr was awarded the distinguished International Berthold Leibinger Innovation Prize 2000 for his work on high power VCSELs. As a special highlight, in an initiative of Martin Grabherr, Roger King, Roland Jäger, and Dieter Wiedenmann the startup company U-L-M photonics was founded. It has been a new experience having production oriented VCSEL development and University based VCSEL research being dealt with in adjacent lab space. Hansjörg Wolf, our talented young technician already transferred to the new company.

Research projects have been prospering and our gratitude is expressed to all public funding organizations and industrial partners that generously supported our work. In 2000, fund raising has been particularly successful in Peter Unger's group. Last but not least the Head of the Department declined an offer to become a Member of the Board of the Karlsruhe Research Center.

Karl Joachim Ebeling January 2001

Low Threshold GaAsSb/GaAs Broad Area Laser Diodes for the Long-Wavelength Range

Irene Ecker, Jürgen Joos and Susanne Menzel

From the viewpoint of realizing long-wavelength vertical-cavity surface-emitting lasers (VCSELs) on GaAs substrates, novel material systems grown on GaAs that emit at 1.3 µm have been attracting great interest. We demonstrate broad area laser diodes with emission wavelengths up to 1254 nm in the GaAsSb/GaAs material system.

1. Introduction

In fiber-optic communication systems light emitting devices at 1.3 µm are widely used. GaAs based devices might be superior to their InGaAsP counterparts in different aspects. Possible advantages are improvement of thermal stability, single epitaxial growth of VCSELs and use of large-area high-quality inexpensive GaAs substrates [1]. Until now various approaches for the growth of VCSEL structures have been investigated. These concentrate mainly on InAs/InGaAs quantum dots, GaAsSb and InGaAsN quantum films. Recently an InAs/InGaAs quantum dot VCSEL at 1.3 µm in pulsed operation at room temperature was reported by Lott et.al. [2]. Yamada et.al. demonstrated a 1.23 µm GaAsSb-VCSEL (cw, room temperature) [3]. An InGaAsN VCSEL with an emission wavelength up to 1294 nm (cw, room temperature) was shown by Choquette et.al. [4]. We focus on the epitaxial growth of compressively strained GaAsSb quantum well structures.

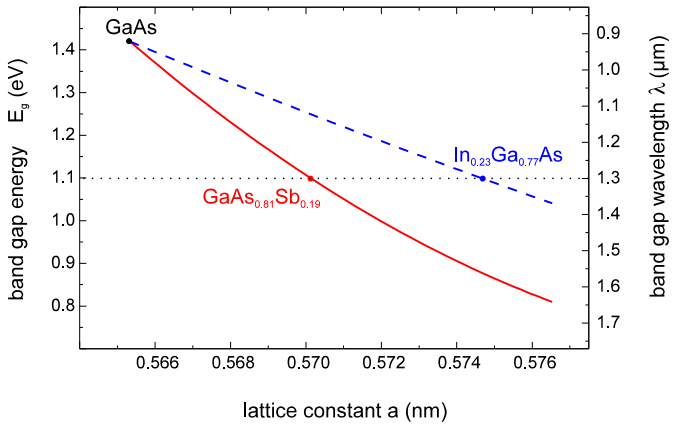

Fig. 1. Bandgap energy of GaAsSb versus InGaAs [5].

The well-established material system InGaAs for laser diodes below 1 μm is not suited for the realization of long-wavelength emitting devices on GaAs substrate. Though the bandgap energy varies from 0.35 to 1.42 eV (0.87–3.5 μm) dependent on indium content crystal growth of InGaAs quantum wells of good quality with an emission wavelength of 1.3 μm on GaAs substrate is not possible. The large lattice mismatch between InGaAs and GaAs ($\varepsilon = 7.16\,\%$ for InAs) results in crystal defects, especially along heterointerfaces. The lattice constant of the binary semiconductors GaSb ($a = 0.6096$ nm) and InAs (0.6058 nm) do not differ very much. In the case of GaSb the lattice mismatch is $\varepsilon = 7.83\,\%$ relative to GaAs. The materialsystem GaAsSb covers a wavelength range from 0.87 to 1.7 μm (0.73–1.42 eV). According to literature there exists a miscibility gap in a region of 39 to 62 % antimony content. However the conditions for the fabrication of long-wavelength emitting laser diodes in the GaAsSb materialsystem are better. This relation is depicted in Fig. 1. Adding In as well as Sb to GaAs reduces bandgap energy and increases lattice constant. But because of the advantageous bowing parameter of GaAsSb it is possible to obtain longer wavelengths at less strain in comparison to InGaAs.

2. Epitaxial Growth

Epitaxial growth is carried out in a modified Riber 32 P GSMBE (gas source molecular beam epitaxy). The MBE system provides the group-III-elements Ga and Al ellementally by effusion cells. The hydride arsine (AsH_3) serves as group-V-precursor and is injected through a high temperature injector (HTI) where it is thermally decomposed at 900 °C to As_2 with an efficiency larger than 99 %. The group-V-element Sb is provided by a special cracker cell. At a temperature of 900 °C the polyatomic Sb-molecules are cracked into dimeres. Si is used as n-type dopant. For p-doping CBr_4 is injected through a low temperature injector (LTI). Si-doped (100) GaAs of epi-ready quality is used as substrate for all samples.

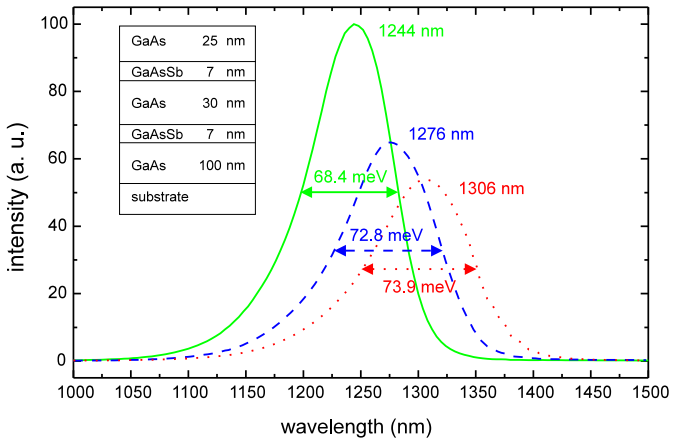

Fig. 2. PL spectra of GaAsSb-DQW structures with varying antimony content.

To investigate the optical quality of GaAsSb, structures for photoluminescence (PL) measurements were grown. The structure – shown as inset in Fig. 2 – contains two 7 nm thick GaAsSb quantum wells which are separated by a 30 nm GaAs layer. By adjusting the antimony to arsine ratio it has been possible to achieve wavelengths longer than 1300 nm. However, with increasing antimony incorporation PL intensity decreases and full width at half maximum (FWHM) slightly increases. Probably the crystal quality suffers a little bit by larger strain caused by higher antimony content. These spectra indicate the possibility to fabricate laser diodes with emission wavelength near 1.3 μm.

3. Laser Design and Device Fabrication

The standard edge emitting devices as well as preliminary and complete VCSEL structures are processed as broad area laser diodes. The active material of all devices is similar: It consists of two compressively strained GaAsSb quantum wells embedded in GaAs. The preliminary stages provide 9.5 n-doped AlGaAs/GaAs mirror pairs and 7 p-doped mirror pairs. For complete VCSEL structures the number of mirror pairs of n- and p-DBR is accordingly increased.

4. Characterization

A) Edge Emitting Devices

Low Threshold Laser Diodes

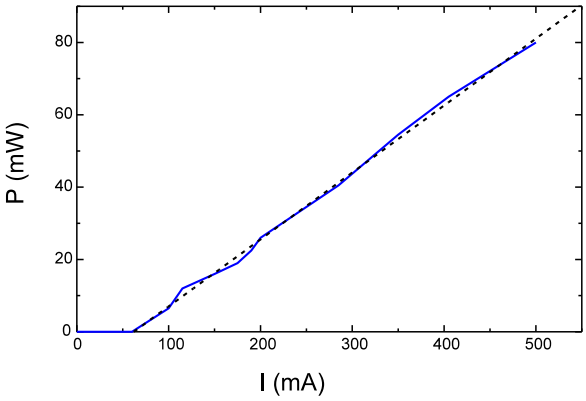

Fig. 3. Light output-current characteristics of GaAsSb/GaAs DQW laser diode under pulsed operation at room temperature.

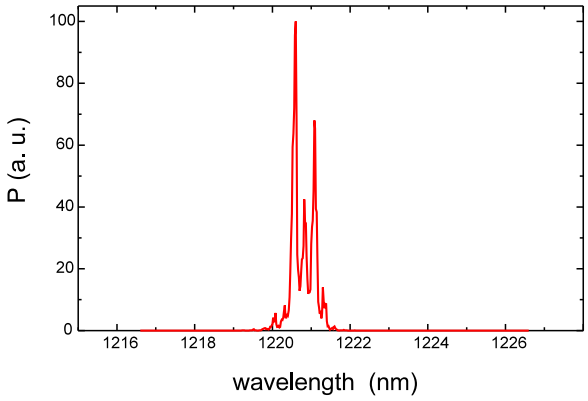

Fig. 4. Emission spectrum of GaAsSb/GaAs laser. The laser oscillates at a wavelength of 1221 nm.

In Fig. 3 and 4 the output characteristics of a low threshold broad area laser diode are shown. The device is driven unmounted with uncoated facets at room temperature and pulsed conditions. The investigated structure has a length of 800 μm and a width of

20 μm. The pulse length is 50 ns and the repetition rate 1 kHz. The threshold current is 60 mA and the threshold current density is calculated to be 375 $\mathrm{Acm^{-2}}$. The spectrum was recorded at a current of 150 mA. The center wavelength exceeds 1220 nm.

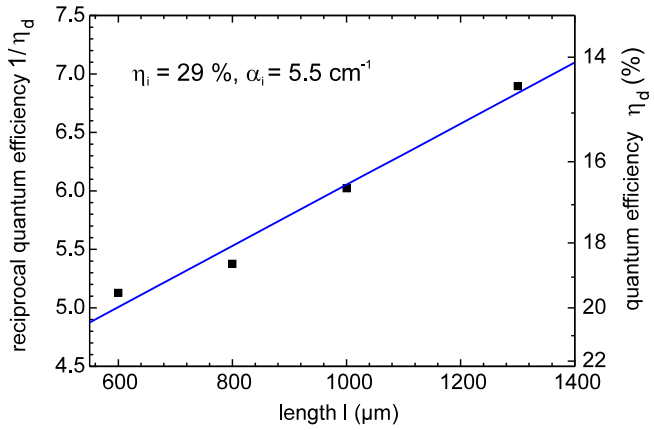

Fig. 5. Internal quantum efficiency η_i and internal losses α_i of edge emitting devices.

Internal quantum efficiency η_i and internal losses α_i were determined according to a plot of the reciprocal quantum efficiency η_d as a function of resonator length (Fig. 5). A value of 29 % for η_i and of 5.5 $\mathrm{cm^{-1}}$ for α_i were found for 20 μm wide laser diodes.

Laser Diodes with Carbon-Doped Barriers

Generally it is observed that lasing occurs at lower wavelength in comparison to the peak wavelength of PL spectrum. The wavelength shift usually varies between 20 to 35 nm which can be clearly seen in the two upper spectra depicted in Fig. 6. This substantial blue shift may originate from a type II GaAsSb/GaAs band alignment or a weak type I alignment. P-doping the GaAs barrier between the quantum wells might counteract the large valence band discontinuity. This could not only result in more uniform hole injection into both of the quantum wells, but also in an improvement of electron-hole wavefunction. In the third comparison between electroluminescence (EL) and PL spectra the wavelength difference is reduced to 14 nm by incorporation of a carbon-doping in the barrier material between the two quantum wells.

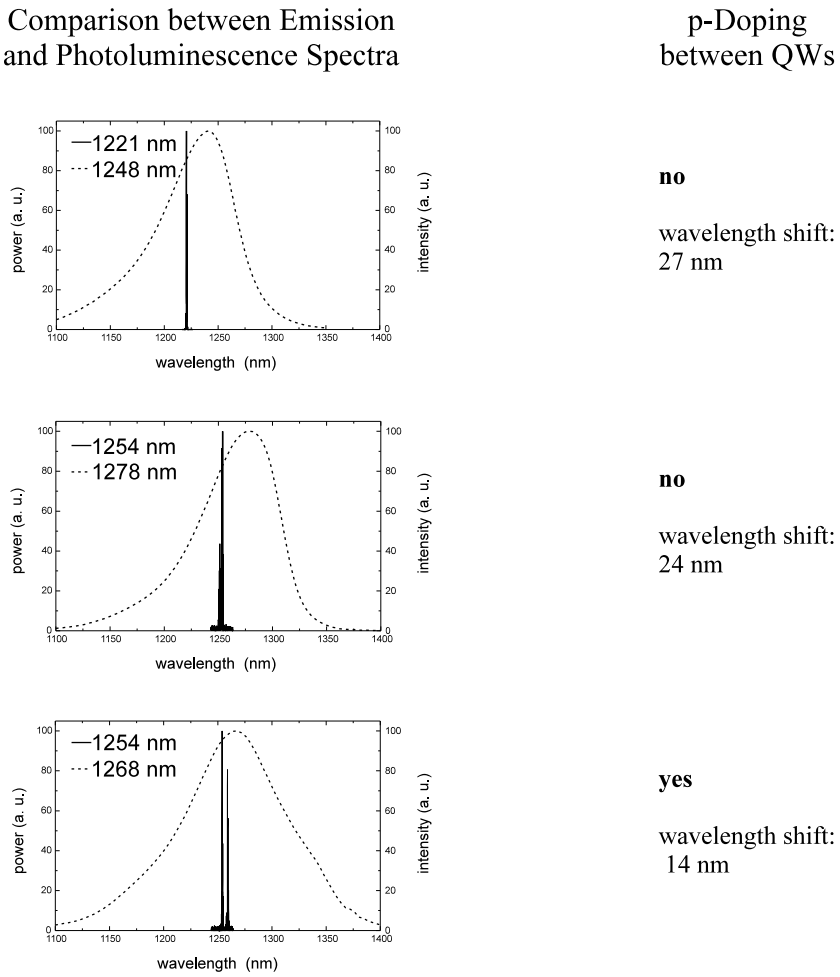

Fig. 6. Influence of p-doping of active zone on emission wavelength.

B) Preliminary and Complete VCSEL Structures

Growth Temperature

The results in the field of edge emitters could be partially transferred to preliminary stages and complete VCSEL structures. In Fig. 7 the output characteristics of a preliminary stage is shown. The threshold current density is 470 Acm^{-2} at a wavelength of 1200 nm under pulsed conditions. At the beginning it was not possible to achieve lasing with complete VCSEL structures. One of the reasons was the growth temperature. During the growth of a complete VCSEL structure the active zone suffers from being at elevated temperature, which is used for the growth of a full p-DBR. To proof this, a preliminary stage was annealed for several hours at a temperature of about 600 °C. After the annealing process the laser diodes had a threshold current density of 1.3 kAcm^{-2} (Fig. 8). This means a triplication of the value. Therefore the growth temperature in the p-DBR was decreased for complete VCSEL structures.

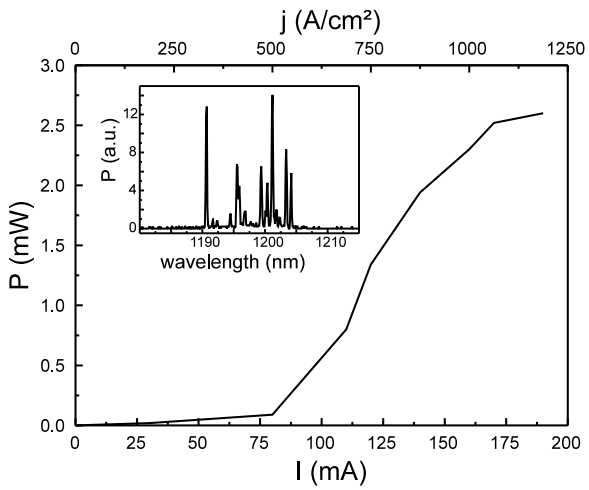

Fig. 7. Light output-current characteristic of a preliminary stage of a VCSEL structure.

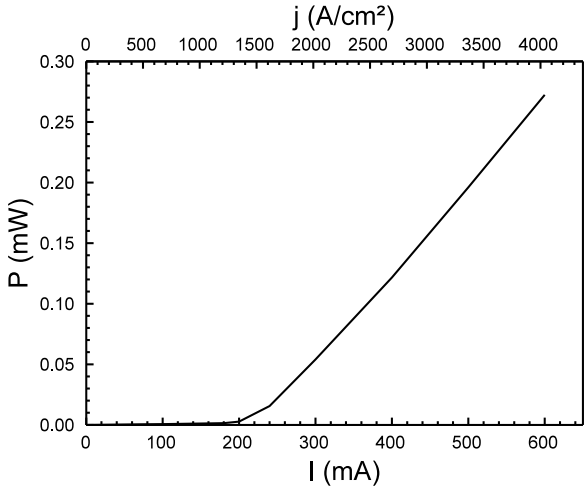

Fig. 8. Light output-current characteristic after annealing process.

Spacer Layer

Through reducing the growth temperature of the p-DBR it was possible to achieve laser emission with complete VCSEL structures. However the threshold current densities were extremely high. The starting base for the growth of the active zone in a preliminary stage is different from a complete VCSEL structure: 9.5 n-doped mirror pairs versus 20 n-doped mirror pairs. Therefore a complete structure containing a spacer layer consisting of pure GaAs was built within the n-DBR. Fig. 9 shows a transmission electron microscopy (TEM) photograph of the layer structure. With this structure it was possible to demonstrate laser oscillation at 1187 nm with threshold current densities of 0.9 kAcm^{-2} under pulsed condition (see Fig. 10).

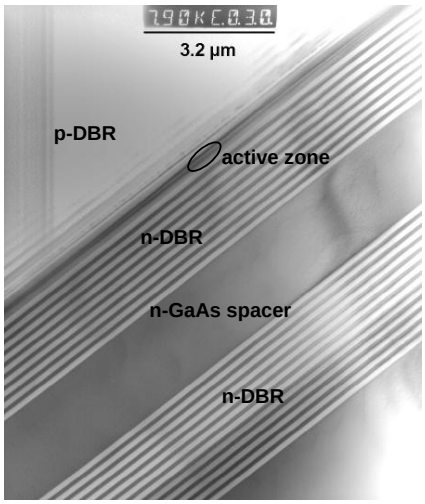

Fig. 9. TEM photograph of a complete VCSEL structure with GaAs spacer within the n-DBR.

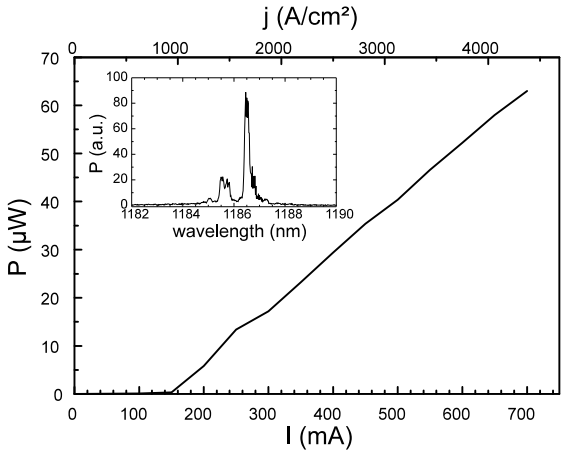

Fig. 10. Light output-current characteristic of a complete VCSEL structure processed as broad area laser diode.

5. Summary

With PL measurements on structures containing two quantum wells the potential of the material system GaAsSb for long-wavelength devices near 1.3 μm could be shown. Broad area laser diodes with threshold current density of 375 Acm^{-2} were presented. The blue shift between PL peak and lasing wavelength could be reduced by p-doping of the barrier within the active zone.

Through optimization of growth process and incorporation of spacer layers laser oscillation at 1187 nm with a threshold current density of 0.9 kAcm^{-2} could be demonstrated on complete VCSEL structures processed as broad area laser diodes.

These results indicate that the material system GaAsSb is a promising candidate for long-wavelength VCSELs.

References

[1] V.M. Ustinov, and A.E. Zhukov, "GaAs-based long-wavelength lasers", *Semicond. Sci. Technol.*, vol. 15, pp. R41–R54, 2000.

[2] J.A. Lott, N.N. Ledentsov, V.M. Ustinov, N.A. Maleev, A.E. Zhukov, A.R. Kovsh, M.V. Maximov, B.V. Volovik, Zh.I. Alferov, and D. Bimberg, "InAs-InGaAs quantum dot VCSELs on GaAs substrates emitting at 1.3 μm", *Electron. Lett.*, vol. 36, pp. 1384–1386, 2000.

[3] M. Yamada, T. Anan, K. Kurihara, K. Nishi, K. Tokutome, A. Kamei, and S. Sugou, "Room temperature low-threshold CW operation of 1.23 μm GaAsSb VCSELs on GaAs substrates", *Electron. Lett.*, vol. 36, pp. 637–638, 2000.

[4] K.D. Choquette, J.F. Klem, A.J. Fischer, O. Blum, A.A. Allerman, I.J. Fritz, S.R. Kurtz, W.G. Breiland, R. Sieg, K.M. Geib, J.W. Scott, and R.L. Naone, "Room temperature continous wave InGaAsN quantum well vertical-cavity lasers emitting at 1.3 μm", *Electron. Lett.*, vol. 36, pp. 1388–1390, 2000.

[5] M. Levinstein, S. Rumyantsev, and M. Shur, "Handbook Series on semiconductor parameters", *Ternary and quaternary III-V compounds*, vol. 2, World Scientific Publishing, 1999.

[6] J. Joos, I. Ecker, and K.J. Ebeling, "Low threshold GaAsSb/GaAs broad area laser diodes emitting at 1220 nm", *Conf. Proc. CLEO/Europe 2000*, Nice, France, Sep. 2000.

Bipolar Cascade VCSEL with 130 % Differential Quantum Efficiency

Thomas Knödl and Matthias Golling

The room temperature, continuous-wave (CW) operation of a fabricated multi-diode cascade vertical-cavity surface-emitting laser at 980 nm wavelength, with a differential quantum efficiency exceeding unity is demonstrated. For the wallplug efficiency, the maximum of 16 % is obtained at a driving current of three times the threshold.

1. Introduction

The performance of conventional vertical-cavity surface-emitting lasers (VCSELs) is generally limited by the extremely low roundtrip gain in the cavity. Thus, VCSEL devices require high mirror reflectivity but also are characterized by an increase in the threshold current density compared to edge emitting lasers. To overcome this distinct disadvantage, diode cascade VCSELs (also called bipolar cascade VCSELs) are proposed as excellent candidates to improve the performance of VCSEL structures with bulk [1] and quantum well [2] active layers. Such a VCSEL can also exhibit high differential quantum efficiency well exceeding unity that may be interesting for low noise applications. The increase in roundtrip gain is also of interest for high-power VCSEL applications. Recently, long wavelength diode cascade VCSELs with CW operation up to 6°C were reported [3]. CW oscillation with diode cascade devices at room temperature was so far only obtained at 980 nm wavelength [4, 5]. All demonstrated devices still suffered from comparatively low slope efficiencies. Recently, we fabricated the first CW room temperature operating multi-diode cascade VCSEL with a differential quantum efficiency exceeding unity [6].

2. Device Structure

Fig. 1 shows a schematic diagram of the device structure that is grown by molecular beam epitaxy. The top and bottom Bragg reflector stacks consist of 14 and 32 $Al_{0.9}Ga_{0.1}As$/GaAs layer pairs, respectively. The inner cavity of the multi-diode cascade VCSEL contains three active pn-junctions in series, each of which comprises three undoped 8 nm thick $In_{0.2}Ga_{0.8}As$ quantum wells separated by 8 nm thick GaAs barriers. The active regions are coupled by two highly doped GaAs Esaki junctions of 21 nm thickness each to realize low resistance quasi-Ohmic inter-contacts for carrier recycling as schematically shown in Fig. 2. Thus, an injected electron can theoretically generate a new photon in each additional active region of the multi-diode cascade VCSEL, exhibiting a differential quantum

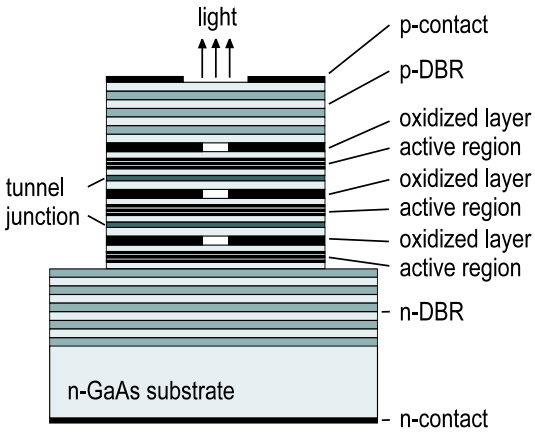

Fig. 1. Device schematic of the investigated top surface emitting multi-diode cascade VCSEL structure.

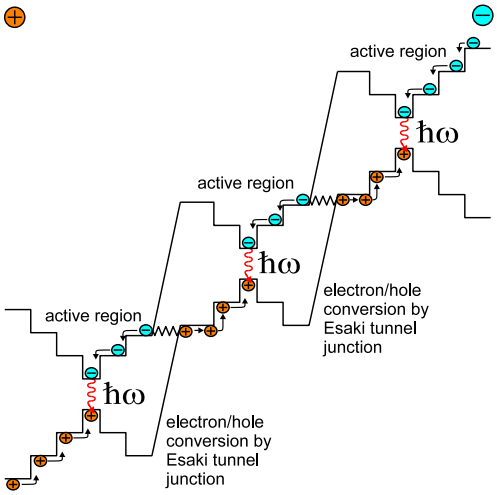

Fig. 2. Schematic band diagram of a three stage diode cascade VCSEL.

efficiency well exceeding unity. Moreover, the reverse biased Esaki junctions are placed in the nodes of the standing wave pattern to reduce free-carrier absorption. For the p- and n-type doping we use C and Si, respectively. Current confinement is achieved by mesa etching and subsequent homogeneous selective oxidation of three 30 nm AlAs layers incorporated above each active region. Thus, it is possible to reduce current spreading in the cavity that is an important issue for the improvement of cascade VCSEL performance [5]. Finally, a ring contact deposited on the mesa allows for top surface emission.

3. Esaki Junction

The performance of cascade VCSELs essentially depend on the implementation of low resistance tunnel junctions to minimize additional device heating. However, the realization is dominated by the n-type doping compensation effect in GaAs. With increasing n-dopant species concentration, eventually the dopant begins to substitute on the acceptor sites limiting the maximum donor incorporation. Our typical GaAs Esaki diode has an p- and n-type doping level of $1\times10^{20}\,\mathrm{cm}^{-3}$ and $2.5\times10^{19}\,\mathrm{cm}^{-3}$, respectively. The minimum zero-bias resistance is about $2.5\times10^{-4}\,\Omega\mathrm{cm}^2$, determined by a four-terminal measurement including contact and substrate resistivity.

4. Multi-Diode Cascade VCSEL

Fig. 3 illustrates the CW, room temperature output characteristics of a fabricated multi-diode cascade VCSEL with three oxide apertures of approximately 9 μm in diameter. The device can be driven far above roll-over without damaging and shows no saturable

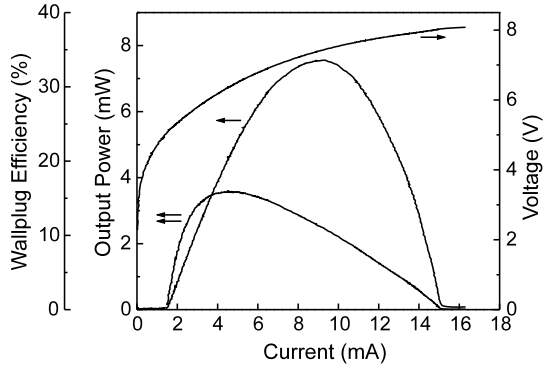

Fig. 3. CW, room temperature output characteristics versus driving current of a multi-diode cascade VCSEL. The measured active diameters are about 9 μm.

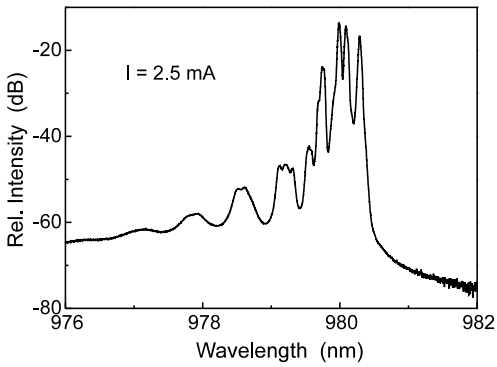

Fig. 4. Optical spectrum of the multi-diode cascade VCSEL at a driving current of 2.5 mA. The measured active diameters are about 9 μm.

absorber behavior as one might expect for a none homogenous current pumping profile between the active regions. At threshold, the emission wavelength is located at 980 nm with a current of 1.5 mA. The threshold voltage of 5 V is about 1.2 V higher than three times the bandgap voltage, indicating a successful implementation of low resistance Esaki junctions. Maximum output power of about 7.2 mW is obtained at a driving current of 9.2 mA. The observed differential quantum efficiency of 130 % also confirms the successful realization of the cascade concept. For the wallplug efficiency we obtain a maximum value of about 16 % at a current of 4.5 mA. The continuous wave spectrum for a driving current of 2.5 mA is displayed in Fig. 4. It shows strong multi-mode emission due to an increase in the optical guiding introduced by the additional oxide apertures.

5. Conclusion

We have demonstrated the first CW operating multi-diode cascade VCSEL at room temperature with a differential quantum efficiency well exceeding unity. The measurement results clearly demonstrate the successful implementation of low resistance Esaki junctions in the cavity for carrier recycling. Further work will include optimizing the Esaki junction and the cascade device structure but also the investigation of the modulation and noise properties of cascade VCSELs.

References

[1] Y. Kotaki, S. Uchiyama, and K. Iga, "GaInAsP/InP Surface Emitting Laser with Two Active Layers", *Conf. Solid State Devices and Materials*, pp. 133–136, 1984.

[2] W. Schmid, D. Wiedenmann, M. Grabherr, R. Jäger, R. Michalzik, and K.J. Ebeling, "CW operation of a diode cascade InGaAs quantum well VCSEL", *Electron. Lett.* **34**, pp. 553–555, 1998.

[3] J.K. Kim, S. Nakagawa, E. Hall, and L.A. Coldren, "Near-room-temperature continuous-wave operation of multiple-active-region 1.55 μm vertical-cavity lasers with high differential efficiency", *Appl. Phys. Lett.* **77**, pp. 3137–3139, 2000.

[4] T. Knödl, R. Jäger, M. Grabherr, R. King, M. Kicherer, M. Miller, F. Mederer, and K.J. Ebeling, "CW room temperature operation of a diode cascade InGaAs-AlGaAs quantum well VCSEL", *in Proc. LEOS Annual Meeting 1999* **2**, pp. 143–144, 1999.

[5] T. Knödl, R. Jäger, M. Golling, M. Miller, and K.J. Ebeling, "Improvement of Diode Cascade VCSEL Performance", *in Proc. CLEO/Europe 2000*, pp. 347, 2000.

[6] T. Knödl, M. Golling, A. Straub, and K.J. Ebeling, "Multi-Diode Cascade VCSEL with 130 % differential quantum efficiency at CW room temperature operation", *Electron. Lett.*, **37**, pp. 31–33, 2001.

Improved Output Performance of High-Power VCSELs

Michael Miller

This paper reports on state-of-the-art single device high-power vertical-cavity surface-emitting laser diodes (VCSELs). The laser diodes are studied in terms of electro-optical characteristics, beam performance and scaling behavior. The maximum cw output power at room temperature of large-area bottom-emitting devices with active diameters up to 320 μm is as high as 0.89 W which is to our knowledge the highest value reported for a single device. Measurements under pulsed conditions show more than 10 W optical peak output power.

1. Introduction

Small diameter VCSELs are accepted devices for datacom applications due to their distinguished performance. One of those is the high conversion efficiency of more than 40 % which is also a basic for high-power devices. But most of the datacom VCSELs have output powers in the range of a few mW. For higher powers edge-emitting lasers are more suited because they achieve up to several W at high conversion efficiencies [1, 2]. Disadvantages of these devices are the strongly elliptical beam with a large divergent far-field angle in the fast axis and the high effort in testing and mounting. To close the gap between low power datacom VCSELs and high power edge-emitting lasers large-area single device VCSELs [3] have been investigated. Our aim is to fabricate devices which combine high optical output powers in the Watt regime and high conversion efficiencies above 20 % in cw-operation at room temperature. As carried out in this previous work [4, 5], large-area top-emitting VCSELs are not suited because of the decreasing efficiencies with increasing device size and the poor beam quality due to the ring-shaped near field caused by the inhomogeneous carrier injection through the top ring contact. Therefore we have concentrated the work on bottom-emitting devices which provide a homogeneous current injection also for large-area devices and are suited for a sophisticated mounting technique.

2. Device Structure

The layer structure is grown by solid-source molecular beam epitaxy on GaAs substrate. A schematic cross-sectional view of a VCSEL array is shown in Fig. 1. The Carbon doped p-type Bragg reflector consists of 30 pairs of $Al_{0.9}Ga_{0.1}As$/GaAs layers. The active region

is composed of three 8 nm thick $In_{0.2}Ga_{0.8}As$ quantum wells for an emission wavelength of about 980 nm. Above the p-type cladding layer a 30 nm thick AlAs layer is inserted. Wet chemical etching with Sulphuric acid is used to define mesa type active regions. The exposed AlAs layer is laterally oxidized in a water vapor atmosphere using Nitrogen as carrier gas at a temperature of 410°C in order to form the current aperture and determine the active diameter of the device. For light emission through the GaAs substrate the Silicon doped n-type distributed Bragg reflector has only 20 layer pairs of the same composition as the p-type mirror. On top of the mesa a full size p-contact consisting of Ti/Pt/Au is evaporated which provides a homogeneous current distribution and serves as a wettable metal pad for soldering. After mechanically polishing the GaAs substrate down to a thickness of 150 μm, an anti-reflection coating of Si_3N_4 with refractive index of 1.89 and quarter-wavelength thickness is deposited using plasma enhanced chemical vapor deposition. The Si_3N_4 layer is opened selectively with reactive ion etching for evaporating Ge/Au/Ni/Au large-area contacts surrounding the emission windows. After annealing the n-type contact at 400°C the processing is completed by depositing an electroplated Au layer of 1–2 μm thickness.

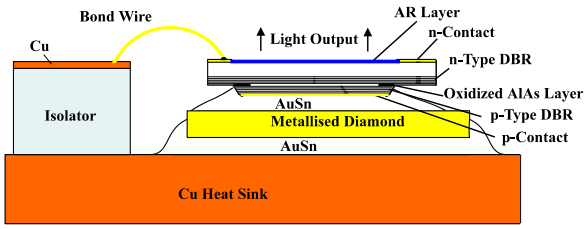

Fig. 1. Cross-sectional view of the oxidized VCSEL array.

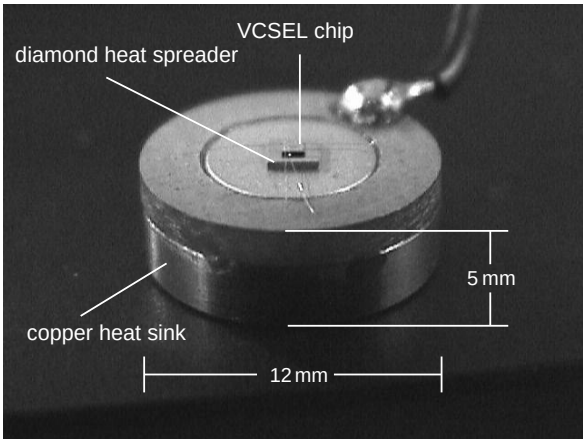

Fig. 2. Mounted semiconductor chip on metalized Diamond and Copper heat sink.

3. Mounting on Heat Sinks

VCSELs with active diameters up to 100 μm can be operated without mounting on heat sinks and are generally capable for on-wafer-testing of electro-optical device performance like threshold current density, threshold voltage, differential resistance, differential efficiency and emission wavelength. Due to a slight gradient in layer thickness across the grown wafer and corresponding detuning of gain and cavity resonance, device performance depends on wafer position. Only large active diameter VCSELs with matched gain and cavity resonance are suited for highest output powers since not optimized detuning increases threshold current and dissipated power and thus device heating drastically.

On-wafer tests are performed in order to select appropriate large-area devices or arrays for mounting. The standard mounting technique is shown in Fig. 2. The cleaved semiconductor chip with dimensions of $0.5\times0.5\,\mathrm{mm}^2$ is soldered junction-down with eutectic $Au_{80}Sn_{20}$-solder on a metalized diamond heat spreader of $2\times2\,\mathrm{mm}^2$ size. The same AuSn solder is used to attach the Diamond on a small Copper heat sink. Soldering is achieved in a single-step heating process at a temperature of about 300°C. The cylindrical Copper mount has a diameter of 12 mm and a height of 5 mm. In the backside a thread is cut for easy mounting on a larger heat sink. Heat dissipation predominantly occurs through the p-type contact. Mounting can be done automatically by pick-and-place machines because alignment tolerances are much more relaxed compared to edge-emitting lasers. Electrical connections are achieved using wire-bonding.

4. Output Characteristics

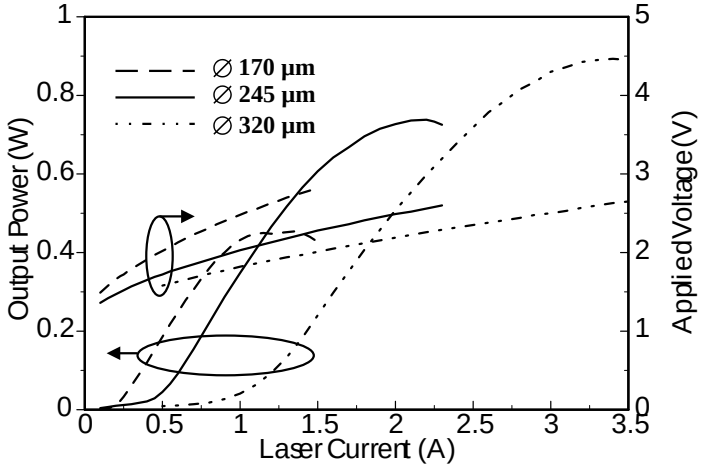

Fig. 3. Output characteristics for large-area single devices with 170, 245, and 320 μm active diameter.

Fig. 3 shows the output characteristics for 3 different device sizes of 170, 245, and 320 μm. The threshold currents are 215 mA, 465 mA, and 1.1 A, respectively, corresponding to a threshold current density of 1 kA/cm^2. The maximum output powers are 450 mW, 740 mW, and 890 mW which are to be compared with 350 mW for a device of 200 μm active diameter reported earlier [6]. Progress is mainly due to improved mounting and soldering techniques.

Various applications like free space data transmission, optical sensing or Light Detecting And Ranging (LIDAR) request pulsed operation. Therefore, we have investigated dynamic behavior. Fig. 4 shows time resolved output power characteristics for excitation with electrical pulses of approximately 10 ns width and a 67 kHz repetition rate where impedance matching of electrical supply lines was not yet optimized. The maximum peak output power of 10 W is achieved at a current of 14 A which was the limit of the current source used. Fig. 5 compares cw and pulsed operation. Obviously, thermal roll-over limits the cw maximum output power whereas pulsed power shows a linear increase with driving current up to 14 A corresponding to a current density of 17.5 kA/cm^2.

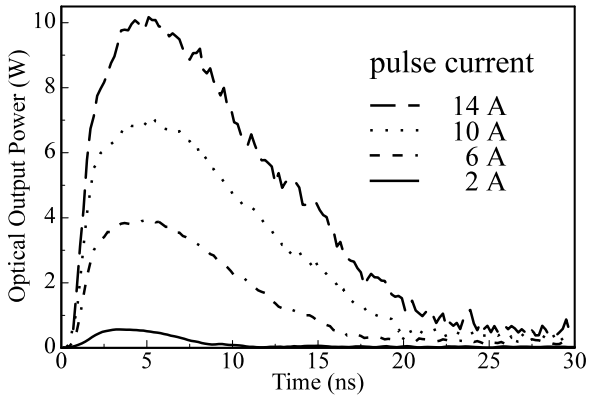

Fig. 4. Optical pulses measured by a fast photodiode at different laser currents. The width of the electrical pulses was about 10 ns and the repetition rate 67 kHz.

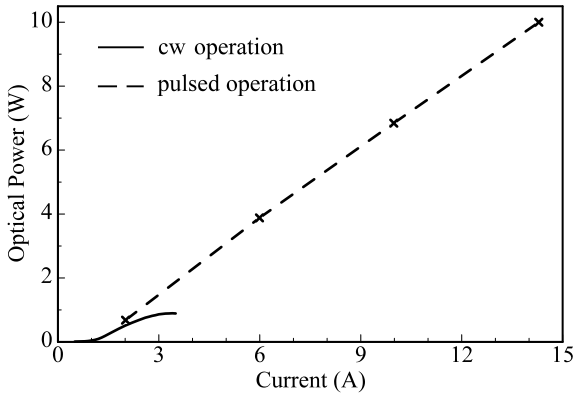

Fig. 5. Comparison of cw operation (solid line) with 0.89 W maximum optical output power and pulsed operation (dashed line) with 10 W maximum peak power.

Due to the large VCSEL diameter the emitted light is strongly multi-mode. For spectral measurements care has to be taken that all light is fed into the spectrum analyzer. For light coupling we have used a 600 μm core diameter Silica fiber with 0.37 numerical aperture at the expense of a resulting comparatively low spectral resolution of about 0.5 nm. Fig. 6 shows measured spectra where individual transverse modes are not resolved. The

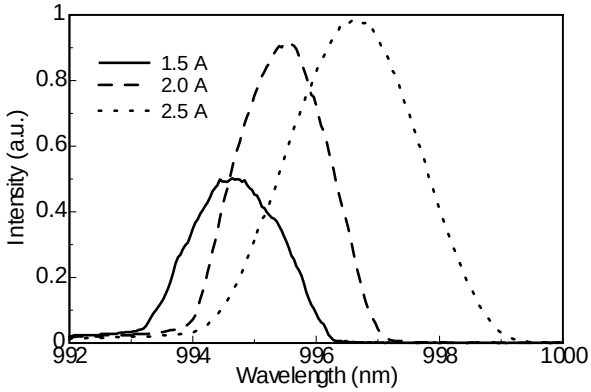

Fig. 6. Spectra of the 320 μm active diameter device for different laser currents.

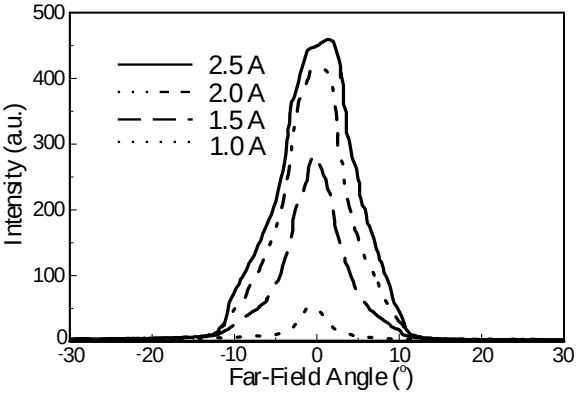

Fig. 7. Far-field profiles of the 320 μm active diameter device for different laser currents.

peak wavelength is in the range of 995 nm due to the cavity resonance but devices can easily be designed for emission wavelengths between 940 nm and 1020 nm. The full width at half-maximum (FWHM) of the spectra is smaller than 5 nm for all currents which is attractive for applications like pumping of Er- or Yb-doped fibers and Nd-YAG microdisk lasers.

The cw far-field patterns of the laser studied are shown in Fig. 7 for different excitation currents. The graphs show a single lobe with less than 12° FWHM for all currents. No side-lobes or amplified spontaneous emission are observed. Due to the circularly symmet-

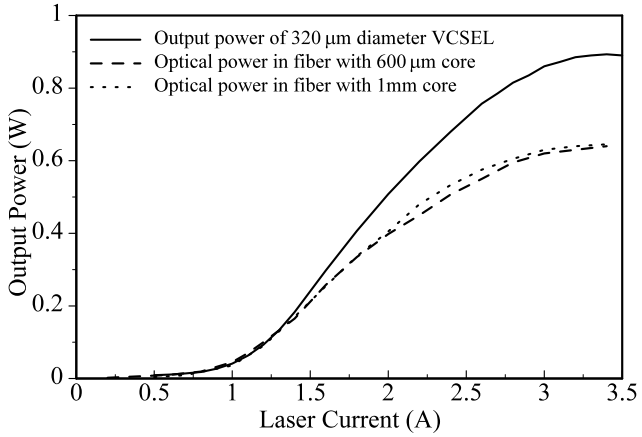

Fig. 8. Optical output power of the laser and launched power at the far end of two 10 meter long large-core fibers of different diameters.

ric far-field pattern the beam can easily be focused or collimated using a single simple lens. In comparison to edge-emitting lasers the low divergence beam is astigmatism free and shows no filamentations.

In order to demonstrate the favorable beam characteristics we have coupled light from a 320 μm diameter VCSEL into two large-core 0.6 and 1.0 mm diameter fibers in a simple butt-coupling arrangement. As indicated in Fig. 8, more than 600 mW of fiber coupled power is measured at the far end of the 10 m long fibers of 0.37 numerical aperture, corresponding to more than 70 % coupling efficiency.

5. Conclusion

In conclusion we have fabricated high-power VCSELs with proven potential for applications requiring output power in the Watt regime. Single devices with active diameters of 320 μm show record high output powers of 0.89 W in cw-operation at room temperature and up to 10 W under pulsed condition which is only limited by the current source. The launched optical power in a large-core diameter fiber by simple butt-coupling is more than 600 mW corresponding to a coupling efficiency of more than 70 %.

References

[1] A. Al-Muhanna, L.J. Mawst, D. Botez, D.Z. Garbuzov, R.U. Martinelli, and J.C. Connolly, "High-power (> 10 W) continuous-wave operation from 100-μm-aperture 0.97-μm-emitting Al-free diode lasers", *Appl. Phys. Lett.*, vol. 73, pp. 1182–1184, 1998.

[2] J. Braunstein, M. Mikulla, R. Kiefer, M. Walther, J. Jandeleit, W. Brandenburg, P. Loosen, R. Poprawe, and G. Weimann, "267 W cw AlGaAs/GaInAs diode laser bars", in *Laser Diodes and LEDs in Industrial, Measurement, Imaging, and Sensors Applications II; Testing, Packaging, and Reliability of Semiconductor Lasers V*, Proc. SPIE, vol. 3945, pp. 17–22, 2000.

[3] F.H. Peters, M.G. Peters, D.B. Young, J.W. Scott, B.J. Thibeault, S.W. Corzine, and L.A. Coldren, "High power vertical-cavity surface-emitting lasers", *Electron. Lett.*, vol. 29, pp. 200–201, 1993.

[4] M. Grabherr, M. Miller, R. Jäger, R. Michalzik, U. Martin, H. Unold, and K.J. Ebeling, "High-power VCSELs: Single devices and densely packed 2-D-arrays", *IEEE J. Select. Topics Quantum Electron.*, vol. 5, pp. 495–502, 1999.

[5] R. Michalzik, M. Grabherr, and K.J. Ebeling, "High-power VCSELs: Modeling and experimental characterization", *Vertical-Cavity Surface-Emitting Lasers II*, Proc. SPIE, vol. 3286, pp. 206–219, 1998.

[6] M. Grabherr, R. Jäger, M. Miller, C. Thalmaier, J. Heerlein, R. Michalzik, and K.J. Ebeling, "Bottom-emitting VCSELs for high-cw optical output power", *Photon. Technol. Lett.*, vol. 10, pp. 1061–1063, 1998.

Approaches for Polarization Control in VCSELs

Michael C. Riedl and Thomas Knödl

The polarization behavior found in standard VCSELs is described. Approaches for polarization control especially stable polarization and polarization multiplex found in literature are presented. Own attempts to control the polarization of our VCSELs include devices with non-cylindrical resonators, polarization selective mirrors, asymmetric current injection and lateral illumination of the mesas.

1. Introduction

Recent progress in longitudinal and transverse single-mode VCSELs has led to devices with optical output powers of more than 5 mW [1]. In addition to the well known advantages of VCSELs over edge emitting lasers like a circular beam, the possibility of two dimensional arrays and on-wafer testing of the devices, these single-mode VCSELs show a Gaussian shaped, low divergence beam and a low relative intensity noise (RIN) due to the absence of mode competition. These properties make single-mode VCSELs a very attractive light source for applications that require the light to be focused to very small spot sizes and low-noise applications. In datacom applications optical fibers can simply be butt-coupled to the circular output facet of the VCSELs resulting in a cheap and highly efficient coupling of the light. Data rates of up to 12.5 Gb/s have been achieved with those devices. Yet these devices can not be used for applications that require linear polarized light stable in certain direction such as magneto-optical recording, coherent detection, polarization multiplex and very low noise applications. Therefore the direction of polarization has to be controlled in order to make VCSELs an interesting light source for these applications as well.

2. Polarization Behavior of Standard Devices

VCSELs although having a cylindrical resonator always emit linear polarized light, which for standard devices grown on (100) substrate is polarized along the crystal directions [011] and $[01\bar{1}]$ with one of them strong and the other one weak. The dominating direction of polarization usually changes with the laser current, showing sometimes gradually changes but more often an abrupt switching behavior even with hysteresis suggesting the influence of non-linear effects as shown in Fig. 1. It is reported [2] that the switching currents can be shifted by applying mechanical stress to the VCSEL sample as well as by changing the temperature of the heat sink. Also, the switching dynamics modulating the current around the switching point have been investigated [2] revealing characteristic times as well as jitter and maximum polarization switching frequency.

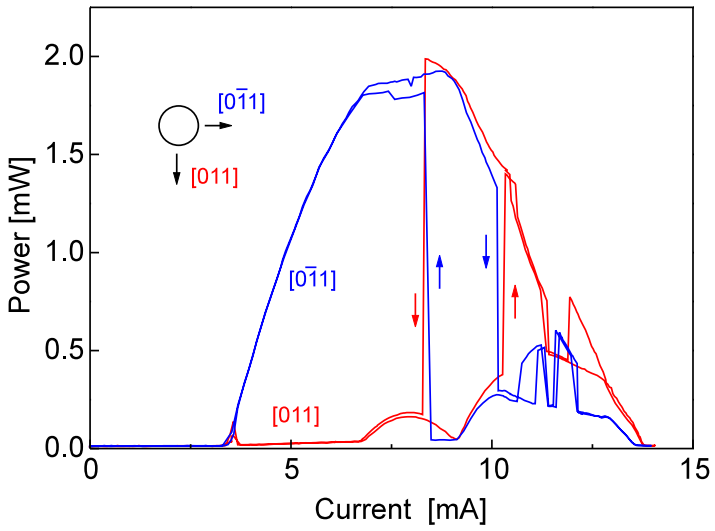

Fig. 1. Typical polarization resolved electro-optic characteristics of a standard VCSEL without polarization control

3. Approaches for Polarization Control

One important approach in literature is growing on non (100) substrate, typically the higher order index plane (311) is chosen [3], resulting in stable polarization in the [$\bar{2}$33] direction and not in the perpendicular [01$\bar{1}$] direction. This proves the influence of anisotropic strain on the polarization. A major drawback is the increased defect density compared to standard (100) substrates.

Non cylindrical resonators being one of the basic and straight forward ideas are also reported to work [4]. As guiding in oxidized VCSELs is provided by the thin oxide layer only, it's position in the standing wave pattern is crucial for the strength of guiding. Weak guiding as desired for single mode devices may inhibit a strong enough impact of the shape of the aperture on the shape of guiding. Unlike standard VCSELs these devices no longer have the advantage of a circular beam.

Polarization selective mirrors can be realized in several ways. The contact at the highly reflective DBR can be realized as a metal grating consisting of lines of two alternating metals, i. e. Au and Cr [5]. Also transmission gratings can be fabricated on the surface of the low reflective mirror by etching the grating into the top semiconductor layer, a dielectric layer [6] or structuring a metal layer.

Asymmetric current injection is also a way to control polarization [7]. As the large number of heterojunctions in the DBRs spreads the current laterally, intra-cavity contacts have to be used in order to have a direct access to the current distribution in the active layers by varying the contact geometry. Using two contact pairs arranged perpendicular, not only stable polarization but also polarization multiplexing can be achieved.

More fancy approaches include etching of a deep trench close to one side of an ion-implanted VCSEL [8], resulting in stress, strain and heat flux being anisotropic, or to introduce a non-symmetric temperature gradient in the VCSEL by placing a heat source close to one side of the VCSEL. Lateral illumination of the VCSEL mesa using a monolithically integrated edge emitting laser might also influence the polarization, although it seems difficult to get an optical power density high enough to actually reach the inner part of the active layer of the VCSEL.

4. Fabrication

Compared to the standard processing of oxide confined top-emitting VCSELs, the four approaches we tried required some changes in fabrication. In the case of non-cylindrical resonators only the mask set needs to be modified in order to achieve the desired shapes of the mesas and adjusting the p-contact rings, passivation and bondpads accordingly. The intra-cavity contacts needed for the asymmetric current injection not only require an additional etching step but also extra epitaxial spacer layers for the lateral current transport and a highly doped p-contact layer combined with an etch stop layer. Fig. 2 shows a cross section and a top view of a preliminary stage of asymmetric current injection with only the n-contact intra cavity. The subwavelength gratings used as polarization selective mirrors can only be defined using E-Beam lithography as the pitch of the gratings is required to be below 300 nm for our standard wavelength of $\lambda = 980$ nm. We etched gratings in the top semiconductor layer and fabricated a metal grating by lift-off of an evaporated 10 nm gold layer each with a pitch of 250 nm as depicted in Fig. 3. For lateral illumination at least the edge emitting laser's facet facing the VCSEL has to be dry-etched with etching parameters optimized to result in an exactly vertical and smooth facet surface. In the mask design the gap between the facet and the VCSEL mesa has to be minimized in order to get as much light into the VCSEL's active layer as possible.

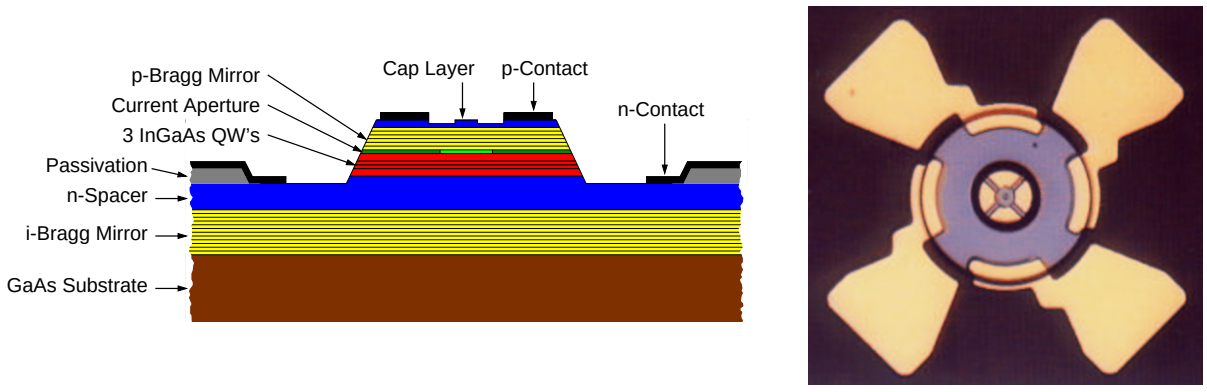

Fig. 2. Preliminary stage of asymmetric current injection with only the n-contact intra cavity before adding the p-Bondpads

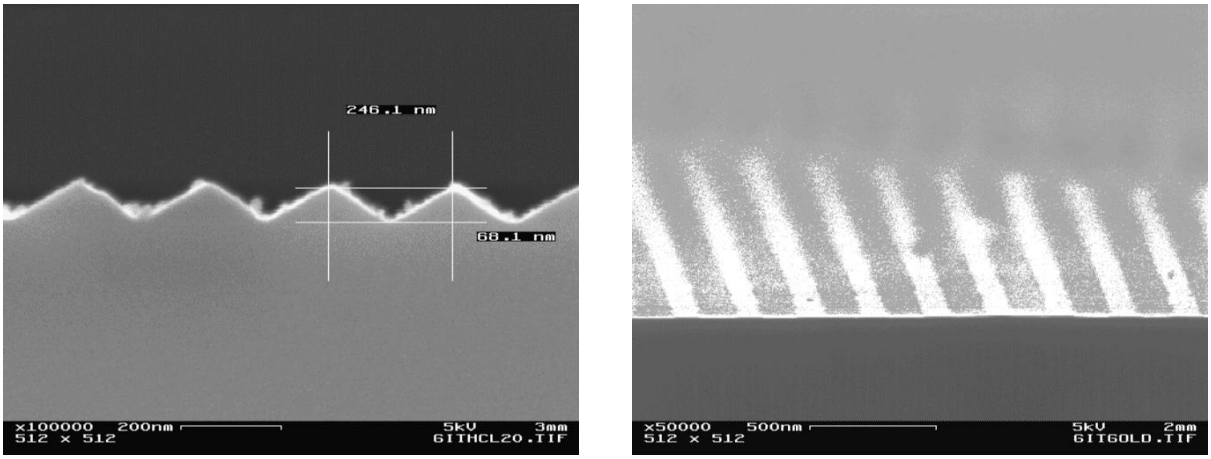

Fig. 3. Sub-wavelength gratings etched into the semiconductor surface (left) and lifted from an evaporated 10 nm gold layer (right)

5. Characterization

As facet etching for the edge emitting lasers did not work too well, only very low optical output powers of these devices could be achieved. Also the gap between the edge emitter and the VCSEL seems to be too large which further decreases the light that actually reaches the active layer in the VCSEL's mesa. Due to these reasons, no influence on polarization can be expected to be seen, as could be confirmed by measurements.

The processing of the polarization selective subwavelength gratings and the non-cylindrical resonators was more successful, unfortunately measurements did not reveal any significant improvement in the polarization characteristics. Just above threshold the non-cylindrical resonators were able to force the polarization to be parallel to the shorter edge of the rectangular resonators, unfortunately without any influence on the polarization switching when increasing the current.

Finally the asymmetric current injection has only been tried with non-intra-cavity contacts so far. These devices did not show any enhanced stability in their polarization behavior. The additional sample made from the preliminary layer structure for just an n-intra-cavity contact did not lase, just very dim spontaneous emission could be observed. It is assumed that a temperature step during processing may have caused relaxation of the lattice in the strained quantum wells thus lowering the gain significantly. As the next sample will be made from the final layer structure the preliminary structure has not been looked into in more detail.

6. Conclusion and Outlook

As none of the approaches worked so far, either due to problems in processing or just without any obvious reason, no improved polarization behavior could be achieved.

In order to improve the combination of an edge emitter with a VCSEL we would suggest to incorporate the VCSEL inside the edge emitter. By doing so, both facets of the edge emitter could be cleaved. In order to avoid any air gaps in the cavity of the edge emitter, electrical isolation between the VCSEL and the two parts of the edge emitter would have to be realized by ion-implantation. Therefore work on this approach is not continued.

Instead, our work will concentrate on asymmetric current injection as this seems to be the most promising approach when p and n intra-cavity contacts are used. First experiments for selective etching as needed for p intra-cavity contacts have been successful, also. Epitaxy of a layer structure incorporating all necessary spacer, contact and etch-stop layers has just been finished on a wafer.

References

[1] H.J. Unold, M. Golling, F. Mederer, R. Michalzik, D. Supper, and K.J. Ebeling, "Single-Mode Output Power Enhancement of InGaAs VCSELs by Reduced Spatial Hole Burning via Surface Etching", submitted to *Electronics Letters*.

[2] G. Verschaffelt, J. Albert, M. Peeters, K. Panajotov, J. Danckaert, I. Veretennicoff, H. Thienpont, F. Monti di Sopra, S. Eitel, R. Hoevel, M. Moser, H.P. Zappe, and K. Gulden, "Polarization switching and modulation dynamics in gain- and index-guided VCSELs", *Proceedings of SPIE*, **3946**, pp. 246–257, 2000.

[3] N. Nishiyama, A. Mizutani, N. Hatori, M. Arai, F. Koyama, and K. Iga, "Lasing Characteristics of InGaAs-GaAs Polarization Controlled Vertical-Cavity Surface-Emitting Lasers Grown on GaAs (311) B Substrate", *IEEE Journal of Selected Topics in Quantum Electronics*, **vol. 5**, no. 3, pp. 530–536, May/Jun 1999.

[4] T. Yoshikawa, T. Kawakami, H. Saito, H. Kosaka, M. Kajita, K. Kurihara, Y. Sugimoto, and K. Kasahara, "Polarization-Controlled Single-Mode VCSEL", *IEEE Journal of Quantum Electronics*, **vol. 34**, no. 6, pp. 1009–1015, June 1998.

[5] C.-A. Berseth, B. Dwir, I. Utke, H. Pier, A. Rudra, V.P. Iakovlev, and E. Kapon, "Vertical cavity surface emitting lasers incorporating structured mirrors patterned by electron-beam lithography", *Journal of Vacuum Science Technology*, **B 17(6)**, pp. 3222–3225, Nov/Dec 1999.

[6] L. Zhuang, S. Schablitsky, R. C. Shi, and S.Y. Chou, "Fabrication and performance of thin amorphous Si subwavelength transmission grating for controlling vertical cavity surface emitting laser polarization", *Journal of Vacuum Science Technology*, **B 14(6)**, pp. 4055–4057, Nov/Dec 1996.

[7] R. C. Strijbos, G. Verschaffelt, M. Creusen, W.C. van der Vleuten, F. Karouta, T.G. van de Roer, M. Buda, J. Danckaert, B. Ryvkin, I. Veretennicoff, and H. Thienpont, "Intra-cavity Contacted VCSELs with Polarization Control", *Proceedings of SPIE*, **3946**, pp. 69–77, 2000.

[8] K. Tastavridis, K. A. Williams, L. J. Sargent, P.J. Heard, J.M. Rorison, R.V. Penty, and I.H. White, "Polarization pinning of a VCSEL array", *Proceedings of SPIE*, **3946**, pp. 78–85, 2000.

Large-Area Single-Mode VCSELs and the Self-Aligned Surface Relief

Heiko J. Unold

The effect of mode-profile specific etching of the top layer in selectively oxidized VCSEL structures at 850 nm emission wavelength is examined. For high reproducibility, a self-aligned etching technique is used which aligns surface etch and oxide aperture by only one additional photoresist step. By optimizing layer structure and etch spot size, completely single-mode devices with aperture diameters up to 16 μm are obtained. Maximum single-fundamental mode output power of 3.4 mW at room temperature and over 4 mW at 0 °C is obtained with a maximum far-field angle of 5.5°. Using parameters for etch spot height and diameter, Gaussian beam spot size and phase curvature, the measured diffracted far-field distribution is fitted well over a 20 dB intensity range. The chosen fit parameters therefore enable to estimate the amount of phase curvature within the VCSEL for different operation currents, which cannot be obtained with available measurement methods.

1. Introduction

High power single-mode emission from vertical cavity surface-emitting lasers (VCSELs) is currently considered a main challenge in opening up new application fields for these promising devices. Their vertical layer structure, apart from significantly facilitating production and testing, also enables integration of one- and two-dimensional arrays which can be used conveniently in parallel data transmission or to obtain cumulative high output power. Due to the very short cavity, longitudinal single-mode operation is inherent to the VCSEL structure. Small oxide aperture VCSELs below about 4 μm diameter also operate in the fundamental transverse mode. Unfortunately, the rather large differential resistance and high current densities in these small devices can affect lifetime. When the aperture diameter is increased to obtain higher output power, however, multiple higher-order transverse modes oscillate, causing increased noise, a much broadened spectrum, and a strong increase of the far-field angle. More specifically, since the number of transverse modes oscillating depends on pumping profile and thermal conditions, these values are subject to strong variations with current, thus rendering optical properties of the VCSEL unreliable. Previous attempts in increasing single-mode output power include external reflectors and other optical elements, increasing the cavity length [1, 2], hybrid implant/oxide VCSELs [3], metal apertures [4], and surface etching [5, 6, 7, 8]. We present the application of an optimized self-aligned shallow surface etch to force oxidized VCSELs of up to 16 μm aperture diameter to operate on the fundamental mode from threshold to

thermal roll-over. Increasing the active diameter while maintaining single-mode emission promises low series resistance, long lifetime and high single-mode output power at small divergence angles.

2. Device Structure and Processing

As described previously, our self-aligned surface etching process allows to align the surface relief automatically to the oxide aperture respective mesa with high precision by only one additional photoresist step [8]. Fig. 1 displays a top view photograph along with a schematic cross-section of a finished device. By simulating the threshold gain of the structure and successively removing part of the top mirror, we can determine the optimum etch depth for any given structure. For simulation, a one-dimensional transfer matrix program is used. As can be expected, due to the periodic nature of a phase variation, the result is a periodic increase and decrease of the threshold gain. When a layer of about $\lambda/2$ thickness has been removed, the threshold gain reaches a minimum, essentially showing the behavior of a VCSEL structure with one Bragg pair less. At the anti-resonance thickness in between, at about $\lambda/4$, a rather narrow local maximum is observed. With our wet chemical etch process, a precision of about ± 3 nm can be reached, which is sufficient to achieve a strong effect but cannot guarantee maximum threshold gain contrast. The epitaxial structure of the examined sample consists of a 20-pair C-doped p-DBR, three 8 nm quantum wells between 10 nm $Al_{0.28}Ga_{0.72}As$ barriers, and a 37.5-pair Si-doped n-DBR, leading to an optimum surface etch depth of about 58 nm.

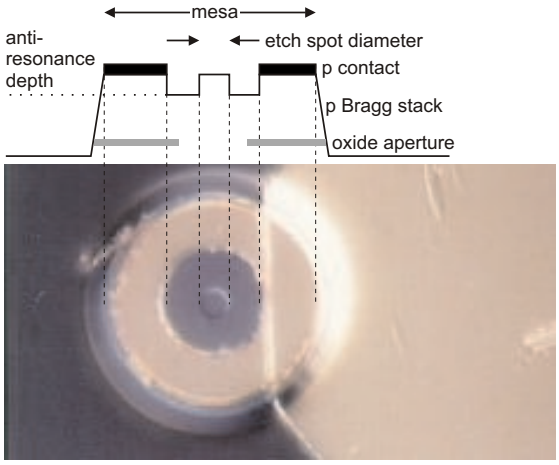

Fig. 1. Top-view photograph and schematic cross-section of the VCSEL structure. In the center the 5 μm diameter etch spot can be seen, surrounded by the anti-resonant DBR region.

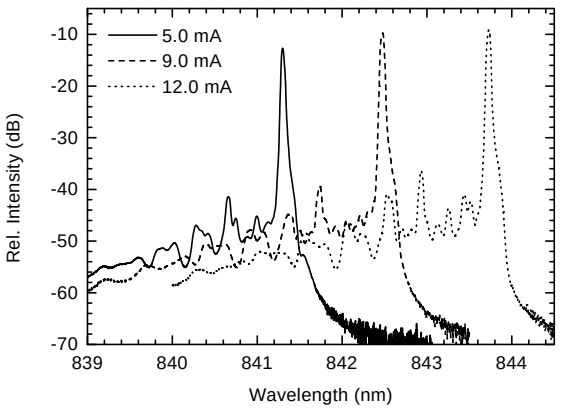

Fig. 2. Spectra measurements for currents from threshold to roll-over for the 11 μm aperture device with 5 μm etch spot diameter.

3. Output Characteristics

As opposed to previous samples, where surface etching only introduced a certain limited single-mode operation range to devices of up to 7 μm diameter [8], the improved layer structure and processing have much augmented the effect. The comparison of unetched devices and etch spots of 3 and 5 μm diameter on 11 μm oxide aperture VCSELs in Fig. 3 confirms that surface etching can have a large impact on laser operation. However, even though threshold is increased and maximum output power is decreased, the fact that the shape of the L-I curves remains smooth is important e. g. for data transmission applications. As shown by the spectra measurements in Fig. 2, although many modes exist, etched devices remain completely single-mode with more than 30 dB SMSR up to thermal roll-over. This indicates that while single-mode operation can be forced upon devices of virtually any size using a small enough etch diameter, an optimum etch diameter exists where single-mode output power is maximum. The oxide aperture size dependence for a

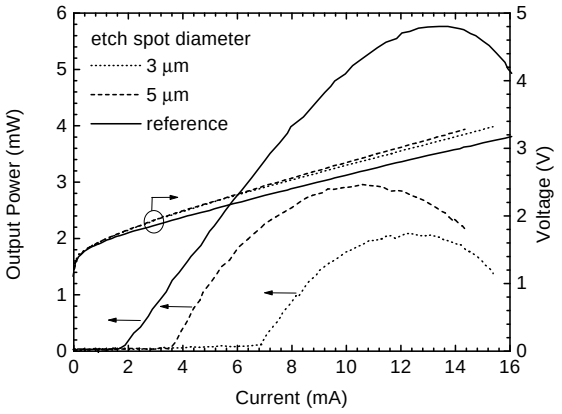

Fig. 3. LIV characteristics of 11 μm diameter devices with different etch spot diameters.

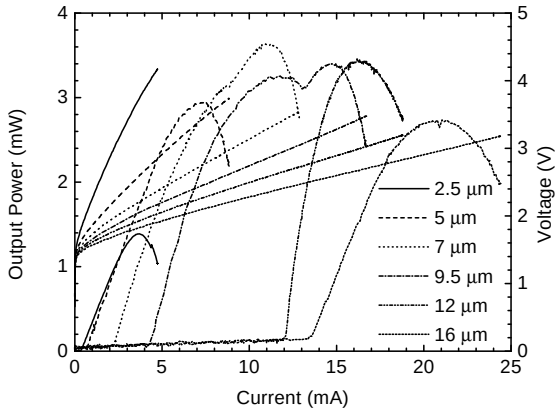

Fig. 4. LIV characteristics of devices with 5 μm etch spot having various aperture diameters.

fixed etch spot diameter of 5 μm is illustrated in Fig. 4. Small devices up to 7 μm aperture diameter exhibit threshold and power scaling as would be observed on standard devices, showing that an etch spot of this size does not influence these devices significantly. For the 12 and 16 μm devices, however, threshold is increased drastically and maximum power even decreases slightly. Since these devices are single-mode, this behavior is consistent with the above discussion on etch spot size dependence. The sudden increase in threshold for the large single-mode devices is caused by a large carrier leakage in the outer regions where no lasing occurs. The 9.5 μm device represents the transition size: having reasonable threshold, thermal roll-over occurs rather early and with less power than the 7 μm device. The device is already forced to the fundamental mode up to this point. For the second local maximum, however, a second mode of comparable intensity is observed. One last interesting feature is the extremely high differential quantum efficiency of the 12 μm device of close to 100%, indicating a continuous improvement of the overlap between the

fundamental mode and the small high reflective region by increased thermal guiding as current is increased. These results therefore confirm that a maximum etch spot size exists for single-mode emission for any given aperture diameter. Additionally, they imply that a certain thermal gradient is also necessary in the VCSEL to force operation on the fundamental transverse mode, illustrated by the high differential quantum efficiency of the 12 μm device and the rather large wavelength shift with current for devices of this size.

4. Far-Field Measurements and Fit Function

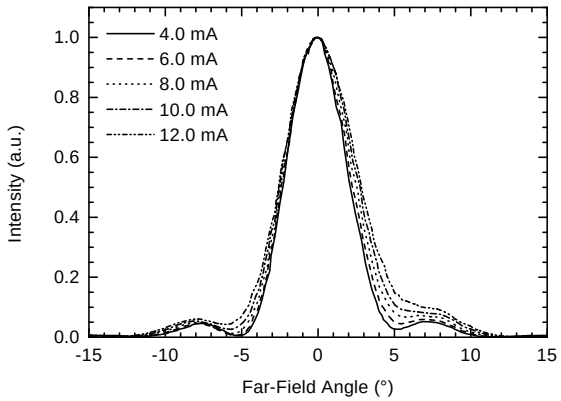

Fig. 5. Far-field measurements for currents from threshold to roll-over for the 11 μm oxide aperture, 5 μm etch spot device.

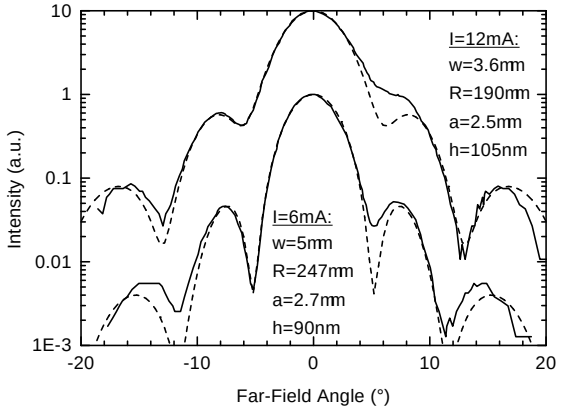

Fig. 6. Logarithmic plot of near-field fit function transformed to far-field (dashed lines) with corresponding far-field measurements (solid lines) for currents of 6 and 12 mA.

The far-field measurements on the 11 μm oxide aperture device with 5 μm etch spot diameter shown in Fig. 5 again confirm single-mode emission by the small full-width half-maximum (FWHM) far-field angle of 4.3° which only broadens by about 20 % over the whole operating range. The far-field angle of the corresponding reference device increases from 5.3° to 11° already at two times threshold. However, the stable side lobes in the far-field of the etched device indicate that diffraction already takes place at the surface etch. In order to investigate the origin of the diffraction pattern, we have adopted a model which fits a Fourier-transformed calculated near-field distribution to the measured far-field data. The near-field function is assumed to be a Gaussian profile with spot size ω and phase curvature R

$$E(r) \;=\; u(r)\cdot\hat{E}\cdot\exp\left\{-\left(\frac{r^2}{\omega^2}+i\frac{\pi\bar{n}r^2}{\lambda R}\right)\right\}, \tag{1}$$

where the phase is locally delayed by the difference in optical lengths between etched and unetched regions expressed by

$$u(r) \;=\; \exp\left\{i\,\mathrm{rect}\left(\frac{r}{a}\right)\left[\frac{2\pi h}{\lambda}\left(\bar{n}_0-\bar{n}\right)\right]\right\}. \tag{2}$$

Here, r is the radial coordinate, a describes etch spot radius, h etch depth, $\bar{n}$ and $\bar{n}_0$ refractive indices in GaAs and air, respectively, and λ the vacuum wavelength. The resulting far-field fit curves are plotted logarithmically for two currents around threshold and at roll-over along with the corresponding measured data in Fig. 6. The good agreement over 20 dB in intensity confirms the validity of the model, especially the choice of fitting parameters. More specifically, the measured data, namely the radial position of the minima, cannot be fitted sufficiently without assuming a curved wavefront in the Gaussian near-field. The geometric parameters a and h can be measured directly and ω is obtained by near-field measurements. We can therefore, to our knowledge for the first time, estimate the phase curvature of the Gaussian beam within an experimental VCSEL by a simple fit to measured data. The obtained values range from 190 to 250 μm for a 11 μm aperture device depending on pumping current. It can therefore be concluded that thermal guiding influences the phase curvature strongly, i. e. it significantly contributes to guiding in these weakly index guided devices having a thin oxide aperture in a standing wave pattern node.

5. Conclusion

We have investigated oxidized VCSELs with self-aligned circular surface etch patterns between 3 and 10 μm diameter having aperture diameters between 2.5 and 16 μm. Single-fundamental mode emission with a side-mode suppression ratio of 30 dB is obtained from threshold to thermal roll-over for all device sizes with appropriate etch spot diameters. 12 μm-aperture devices with 5 μm etch spot diameter achieve 3.4 mW single-mode output power at room temperature and more than 4 mW at 0°C. Due to diffraction at the surface etch, the FWHM far-field angle is stabilized to below 5.5°. Comparison of the different device sizes, pulsed and cooled measurements lead us to the conclusion that increased guiding could significantly reduce threshold and thus enhance single-mode power output. A further increase in single-mode power is expected from additionally restricting the gain laterally to match the surface etch spot.

References

[1] D. G. Deppe and D. L. Huffaker, "High spatial coherence vertical-cavity surface-emitting laser using a long monolithic cavity", *Electron. Lett.*, vol. 33, pp. 211–213, 1997.

[2] H. J. Unold, S. W. Z. Mahmoud, R. Jäger, M. Kicherer, M. C. Riedl, and K. J. Ebeling, "Improving Single-Mode VCSEL Performance by Introducing a Long Monolithic Cavity", *Photon. Techn. Lett.*, vol. 12, pp. 939–941, 2000.

[3] K. D. Choquette, A. J. Fischer, K. M. Geib, G. R. Hadley, A. A. Allerman, and J. J. Hindi, "High Single Mode Operation from Hybrid Ion Implanted/Selectively Oxi-

dized VCSELs", in *Proc. IEEE 17th International Semiconductor Laser Conference*, Monterey, U.S.A., Sept. 2000, pp. 59–60.

[4] T. Nakamura, H. Nakayama, A. Sakamoto, N. Ueki, J. Sakurai, H. Otoma, Y. Miyamoto, and M. Fuse, "High Power Single-Mode 780 nm Oxide-Confined VCSEL with Metal Aperture as a Spatial Filter", in *Proc. IEEE 16th International Semiconductor Laser Conference*, Nara, Japan, Oct. 1998, pp. 7–8.

[5] P. Dowd, L. Raddatz, Y. Sumaila, M. Asghari, I. H. White, R. V. Penty, P. J. Heard, G. C. Allen, R. P. Schneider, M. R. T. Tan, and S. Y. Wang, "Mode Control in Vertical-Cavity Surface-Emitting Lasers by Post-Processing Using Focused Ion-Beam Etching", *Photon. Techn. Lett.*, vol. 9, pp. 1193–1195, 1997.

[6] L. M. A. Plouzennec, L. J. Sargent, R. V. Penty, and I. H. White, "Gaussian Beam Profile and Single Transverse Mode Emission from Previously Multi-Mode Gain Guided VCSEL using Novel Etch", in *Vertical-Cavity Surface-Emitting Lasers IV*, C. Lei K. D. Choquette, Ed., Proc. SPIE, 2000, vol. 3946, pp. 219–229.

[7] H. Martinsson, J. A. Vukušić, and A. Larsson, "Single-Mode Power Dependence on Surface Relief Size for Mode-Stabilized Oxide-Confined Vertical-Cavity Surface-Emitting Lasers", *Photon. Techn. Lett.*, vol. 12, pp. 1129–1131, 2000.

[8] H. J. Unold, M. Grabherr, F. Eberhard, F. Mederer, R. Jäger, M. Riedl, and K. J. Ebeling, "Increased-area oxidised single-fundamental mode VCSEL with self-aligned shallow etched surface relief", *Electron. Lett.*, vol. 35, pp. 1340–1341, 1999.

Analysis of Longitudinal Mode Waveguiding in VCSELs with Long Monolithic Cavity

Safwat W.Z. Mahmoud

Lasing mode switching between two longitudinal modes is observed in transverse single-mode vertical-cavity surface-emitting lasers with an extended cavity. Near- and far-field analyses carried out on devices with 2, 4, and 8 μm cavity spacers show an inherent relation between the transverse mode diameter and the calculated oxide- or thermally-induced index guiding for the oscillating modes. Depending on the designed alignment of the optical longitudinal standing wave patterns relative to the oxide layer, mode switching can either be promoted or suppressed. Record-high single-mode output powers up to 5.5 mW obtained from devices with 8 μm spacers and 8 μm active diameter indicate the potential of the given device concept for low-divergence fundamental mode emission as required for many applications.

1. Introduction

In recent years, the performance of vertical-cavity surface-emitting lasers (VCSELs) has significantly advanced. Using selectively oxidized current apertures for fabrication, low threshold current [1] and high single-mode output power [2] VCSELs have been achieved. Oxide layers influence the optical field distribution in the cavity by their reduced index of refraction, producing efficient mode guiding by the induced lateral effective index difference [3]. There has been extensive interest in large area single-mode VCSELs of low electrical resistance which are especially attractive for high-speed optical data communications and array applications. In particular, one approach based on a long monolithic cavity has resulted in single-mode devices with far-field divergence angles of only 1.6° (e^{-2}-beam half-angle) for a 30 μm aperture diameter [4]. In recent work [5], the incorporation of a lightly n-doped GaAs spacer of thickness $L_s = 4\,\mu$m directly underneath the active region of a 7 μm aperture device has led to the highest singlemode VCSEL output power of 5 mW under continuous wave (cw) operation reported to date. With this kind of device, we have observed lasing mode switching between two longitudinal modes in VCSELs with 2 and 8 μm cavity spacers. The motivation of the present work is to obtain a more detailed understanding of the experimentally observed longitudinal mode structure of these devices. This is accomplished by near- and far-field measurements as well as numerical analyses based on the transfer matrix method.

2. Device Structure and Simulations

The selectively oxidized VCSEL structures for this work are introduced in [5]. From a theoretical point of view, based on the transfer matrix method, it is found that the number of longitudinal modes is increased by increasing the cavity length, as illustrated by the reflectivity spectra (dashed curves) in Figs. 1(a)-(c) for 2, 4 and 8 μm spacers, respectively. We also see that a central mode $LP_{01}^{(0)}$ in the two cases of 2 and 8 μm spacers is present, while in case of 4 μm it is absent due to a slightly too thick inner cavity. The curves in

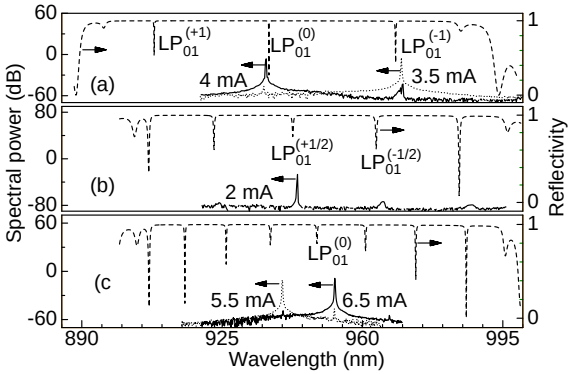

Fig. 1. Calculated reflectivity spectra (dashed curves) of VCSEL structures with (a) $L_s = 2\,\mu$m and measured spectra at 3.5 mA (dotted curve) and 4 mA (solid curve) for a $D_a = 4\,\mu$m active diameter device (b) $L_s = 4\,\mu$m and spectrum at 2 mA (solid curve) for $D_a = 7\,\mu$m (c) $L_s = 8\,\mu$m and spectra at 5.5 mA (dotted curve) and 6.5 mA (solid curve) for $D_a = 8\,\mu$m.

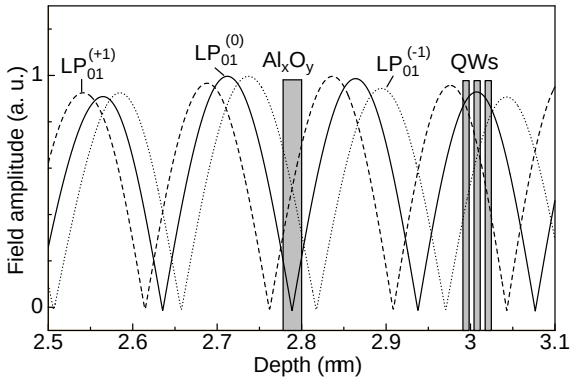

Fig. 2. Resonant standing wave patterns corresponding to the fundamental and the neighboring order longitudinal modes for the VCSEL structure of Fig. 1a).

the lower part of these figures illustrate the observed emission spectra of 4, 7 and 8 μm aperture devices, respectively. These observed spectra show the switching between two longitudinal modes except in case of $L_s = 4\,\mu$m where lasing on the same longitudinal mode is observed over the whole current range. The mode separations of these observed modes are in good agreement with the values obtained from the calculations. The calculated standing wave patterns of the optical fields are depicted in Fig. 2 for the case of Fig. 1(a). It is seen that the resonator is designed such that the oxide layer Al_xO_y is centered at a node of the $LP_{01}^{(0)}$ optical field while it is shifted from the node for the $LP_{01}^{(\pm1)}$ fields and as a result, the latter experience much stronger index guiding. Although the one-dimensional calculations show that the central mode $LP_{01}^{(0)}$ in case of 2 and 8 μm spacers has a lower threshold gain than the $LP_{01}^{(\pm1)}$ modes, the latter start oscillating first because they are more strongly index guided and thus have a higher lateral confinement factor associated with lower losses. At higher driving currents, thermal lensing reduces the mode diameter so that the central mode is finally excited. The importance of thermal lensing as an aid to

excite a weakly guided mode is also pointed out in [6]. In case of $L_s = 4\,\mu$m the situation is different. The optical fields of the modes labeled as $LP_{01}^{(\pm 1/2)}$ have the same overlap with the oxide layer and thus simply the longitudinal mode positioned closer to the center of the stop-band is dominating over the whole current range.

3. Output Characteristics

Fig. 3 shows light output characteristics for the VCSELs from Fig. 1. Emission is in the Gaussian-like fundamental transverse mode up to 7 mA for the device with $L_s = 2\,\mu$m, 9 mA for the $4\,\mu$m spacer, and 12 mA for longest spacer VCSEL, corresponding to 3.4, 5.0 and 5.5 mW maximum output powers. It is seen that the output power of the $2\,\mu$m spacer device exhibits a dip at 4 mA where switching between the $LP_{01}^{(-1)}$ and $LP_{01}^{(0)}$ modes takes place, as illustrated also by the spectra in Fig. 1(a). The $8\,\mu$m spacer device has a similar output power dip at 6 mA but in this case switching between the $LP_{01}^{(+1)}$ and $LP_{01}^{(0)}$ modes is observed, as illustrated by the spectra in Fig. 1(c). The output curve of the $4\,\mu$m spacer device shows no dip because there exists only a single longitudinal mode.

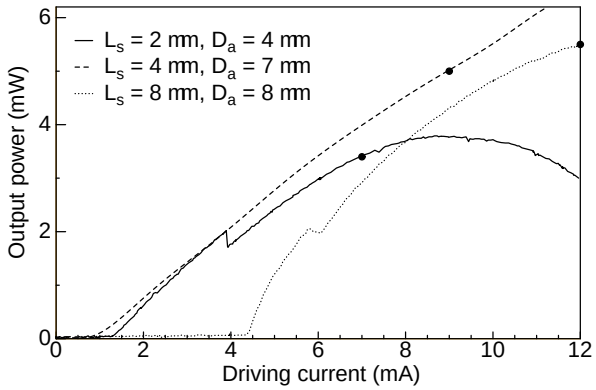

Fig. 3. Light output characteristics for VCSELs with different spacer thicknesses L_s and active diameters D_a from Fig. 1. Dots indicate the onset of higher order transverse modes, i.e. the decrease of sidemode suppression ratio below 30 dB.

4. Near- and Far-Field Analyses

To analyze the spatial profiles of the lasing modes, we have carried out near-field measurements based on a fiber tip scanning technique [7]. Fig. 4(a) shows the measured near-field intensity profiles for the $4\,\mu$m aperture device with $2\,\mu$m spacer at 3.5 mA and 4 mA current, fitted to Gaussian profiles with e^{-2}-beam half-width w of $2.55\,\mu$m and $3\,\mu$m, respectively. Fig. 4(b) shows the same measurements for the $8\,\mu$m aperture device with $8\,\mu$m spacer at 5.5 mA and 6 mA fitted to Gaussian profiles with $w = 4.25\,\mu$m (not drawn) and $4.4\,\mu$m, respectively. Figs. 4(c) and (d) represent the measured far-field

distributions around the switching point for the two cases considered including the corresponding Fourier transformations of the Gaussian profiles. It becomes apparent that the Gaussian fits represent the measured data very well. The determined e^{-2}-beam half-widths w versus cw driving current for single transverse mode operation are summarized in Fig. 5(a). The open squares represent the data for a VCSEL with $D_\mathrm{a} = 4\,\mu$m and spacer length $L_\mathrm{s} = 2\,\mu$m and show a sudden increase of w at 4 mA at which switching between the $\mathrm{LP}_{01}^{(-1)}$ and $\mathrm{LP}_{01}^{(0)}$ modes occurs. This means that the $\mathrm{LP}_{01}^{(-1)}$ mode experiences much stronger index guiding than the $\mathrm{LP}_{01}^{(0)}$ mode, in accordance with Fig. 2. The open circles illustrate the same effect for a VCSEL with $D_\mathrm{a} = 8\,\mu$m and $L_\mathrm{s} = 8\,\mu$m but in this case switching takes place between the $\mathrm{LP}_{01}^{(+1)}$ and $\mathrm{LP}_{01}^{(0)}$ modes. The open triangles stand for the VCSEL with $D_\mathrm{a} = 7\,\mu$m and $L_\mathrm{s} = 4\,\mu$m. Fig. 5(b) represents the e^{-2}-beam half-angle θ from the independent far-field measurements for the three cases considered. As expected, the sudden increases of the beam half widths in the near-fields translate into decreases of far-field angles at the switching points. To understand the measurements theoretically,

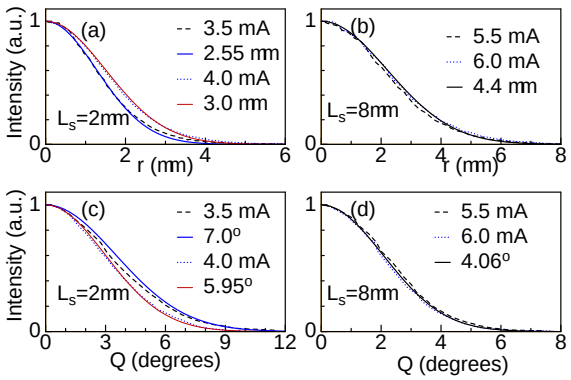

Fig. 4. (a) Measured near-field intensity distributions for a 4 μm aperture device at 3.5 mA (dashed curve) and 4 mA (dotted curve) and fit data (thick and thin solid curves) with the mode radius w given in the legend. (b) The same measurements as in (a) for a VCSEL with 8 μm active diameter at 5.5 mA (dashed curve) and 6 mA (dotted curve), the latter fitted to a Gaussian profile (thick solid curve). (c) Measured far-field intensity distributions for the same case as in (a) and the Fourier transformation of the Gaussian profiles (thick and thin solid curves) with their respective values of θ. (d) Measurements and calculations as in (c) for the device from (b).

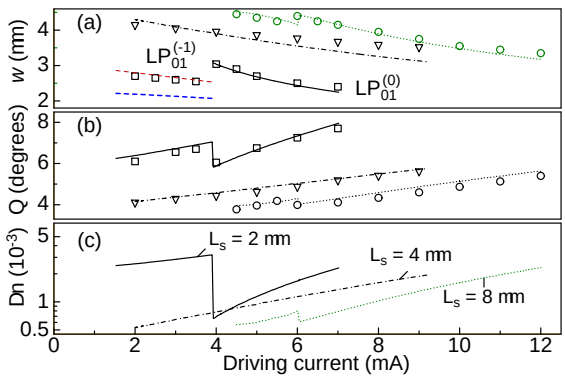

Fig. 5. For the VCSELs of Fig. 3: (a) Measured beam radius w (open squares, triangles and circles) and calculated values using (1) (thin dashed curve) and (2) (solid, thick dashed, dotted dashed and dotted curves). (b) Measured beam divergence half-angle θ (open squares, triangles and circles) and the calculated values (solid, dashed dotted and dotted curves). (c) Calculated induced index step.

we have used the same model as described in [6] to determine the total induced refractive index difference Δn taking effects of free carrier induced index Δn_fc, thermal lensing, and oxide confinement into account. For simplicity, Δn_fc is set to a constant value for each

device obtained from the fit to the measured near-field data. The heat is assumed to be distributed within a sheet of thickness d encompassing the full n-GaAs spacer plus an equivalent of 40 DBR pairs. The thickness of these mirror pairs is about two thirds of the whole DBR which is the same ratio used in [6]. A thermal conductivity $\sigma = 0.44\,\mathrm{W/(Kcm)}$ is used due to the presence of the GaAs spacer in the cavity. The e^{-2}-beam half-width w of the fundamental Gaussian mode can be obtained as in [8] to be

$$w = \frac{D_\mathrm{a}}{2\sqrt{\ln\left(\pi D_\mathrm{a}\sqrt{2n_0\Delta n}/\lambda\right)}} \quad , \tag{1}$$

under the assumption of a step index profile, whereas a parabolic index profile gives

$$w = \sqrt{\frac{\lambda D_\mathrm{a}}{2\pi\sqrt{2n_0\Delta n}}} \quad , \tag{2}$$

where λ is the emission wavelength and $n_0 = 3.3$ the average refractive index in the VCSEL. This value is taken for the center of the cylindrical waveguide while for the cladding it is assumed to have dropped to $n_0 - \Delta n$ at the radial position $r = D_\mathrm{a}/2$. The total induced index difference Δn is calculated for the three cases under investigation with the optimum value of Δn_fc and is plotted versus pumping current in Fig. 5(c). In case of the $2\,\mu$m spacer we get $\Delta n_\mathrm{fc} = -1\times10^{-3}$ and the solid curve shows a large discontinuity in Δn at 4 mA because the $\mathrm{LP}_{01}^{(-1)}$ mode experiences an induced oxide index step of about $\Delta n_\mathrm{ox} = 3\times10^{-3}$ which is nearly ten times the oxide induced index change for the $\mathrm{LP}_{01}^{(0)}$ mode. Therefore oxide-guiding is dominant for the $\mathrm{LP}_{01}^{(-1)}$ and the index profile is well approximated by a step function. This in turn results in w described by (1) which agrees well with the measured values, as illustrated by the thin dashed curve in Fig. 5(a). Using (2) fails in reproducing these data as seen from the thick dashed curve in the same figure. For the weakly confined $\mathrm{LP}_{01}^{(0)}$ mode the situation is different since at 4 mA the induced thermal lensing is dominant and the index profile is approximated well by a parabolic profile. As seen from the solid curve in the same figure, (2) nicely fits the experimental data. At the switching point these calculations show 17 % beam half-width shrinkage for the strongly confined mode $\mathrm{LP}_{01}^{(-1)}$, which is in agreement with the measured value. If a transition from step- to parabolic-like guiding is not taken into account, this value is increased to 34 %. In the case of $L_\mathrm{s} = 8\,\mu$m, corresponding to the dotted curve in Fig. 5(c), only a small difference in Δn at 6 mA is observed because the oxide induced index change for the two modes is reduced owing to the increased cavity length and thus reduced longitudinal filling factor. Thermal lensing is reduced too due to the increased spacer length and associated smaller thermal resistance but is increased of course for increasing pumping current. In total, this leads to the dominance of thermal lensing and thus the index profile can be approximated by a parabolic profile over the whole current range. The use of (2) fits the measured data when $\Delta n_\mathrm{fc} = -5\times10^{-4}$, as shown by the dotted curve in Fig. 5(a). The beam half-width shrinkage in this case for the strongly confined mode $\mathrm{LP}_{01}^{(+1)}$ is reduced to 5 % at the switching point because Δn_ox is reduced by an order of magnitude compared to the $L_\mathrm{s} = 2\,\mu$m device. In the case of $L_\mathrm{s} = 4\,\mu$m, the dashed dotted curve in Fig. 5(c)

represents Δn with $\Delta n_{\mathrm{fc}} = -2\times10^{-4}$. In this case there is no mode switching and the use of (2) reproduces the experimental data as illustrated by the dashed dotted curve in Fig. 5(a). A smaller $|\Delta n_{\mathrm{fc}}|$ is to be expected since the cumulative free carrier induced wavelength shift is dependent on the effective cavity length. The value $|\Delta n_{\mathrm{fc}}|$ for $L_{\mathrm{s}} = 4\,\mu$m is smaller than that for the $8\,\mu$m spacer because the latter shows significantly increased threshold current. The e^{-2}-beam divergence half-angle θ is calculated using the formula $\theta = \lambda/(\pi w)$ which reproduces the measured data for all lasers, as seen in Fig. 5(b).

5. Conclusion

In conclusion, we have shown that both modal gain and induced oxide index are responsible for switching between longitudinal modes in extended cavity VCSELs. Consistent spectral as well as near- and far-field analyses combined with transfer matrix calculations well describe the observed data and show that the modes are either dominantly guided by the built-in effective index step or the thermally induced index profile. As evidenced by the record values of 5 mW for $L_{\mathrm{s}} = 4\,\mu$m and 5.5 mW (if not regarding the longitudinal mode switching) for $L_{\mathrm{s}} = 8\,\mu$m, VCSELs of the extended cavity type are suitable candidates to obtain higher single-mode output power from monolithic devices. Their larger diameter and thus reduced series resistance and driving current density is expected to improve both manufacturability and reliability. The obtained understanding of guiding effects should allow for a tailoring of emission properties in future laser designs.

References

[1] D. L. Huffaker and D. G. Deppe, Appl. Phys. Lett., 71, pp. 1449–1451, 1997.

[2] R. Jäger, M. Grabherr, C. Jung, R. Michalzik, G. Reiner, B. Weigl, and K. J. Ebeling, Electron. Lett., 33, pp. 330–331, 1997.

[3] G.R. Hadley Opt. Lett.,20, pp. 1483–1485, 1995.

[4] D.G. Deppe and D.L. Huffaker, Electron. Lett., 33, pp. 211–213, 1997.

[5] H.J. Unold, S.W.Z. Mahmoud, R. Jäger, M. Kicherer, M.C. Riedl, and K.J. Ebeling, IEEE Photonics Technol. Lett., 12, pp. 939–941, 2000.

[6] M. Brunner, K. Gulden, R. Hövel, M. Moser, and M. llegems, Appl. Phys. Lett. 76, pp. 7–9 (2000).

[7] S.W.Z. Mahmoud, Annual Report 1999.

[8] A.W. Snyder and J.D. Love, Optical waveguide theory, Champan & Hall, London, 1991.

32-VCSEL Channel CMOS-Based Transmitter Module for Gb/s Data Rates

Roger King

In the implementation of optical data links, issues of power consumption, bandwidth and sensitivity have to be addressed in the design of optoelectronic components. This is especially important in high density parallel applications where large amounts of heat can cause thermal problems and performance degradation. We present a 0.6 µm-CMOS VCSEL transmitter with 32 data channels whose power consumption is 15.7 mW/ch at 1 Gb/s/ch data transmission.

1. Introduction

The ever increasing CMOS integration density and operation frequency of CMOS chips is causing electrical interconnection bottlenecks to emerge both for inter-chip and intra-chip interconnections. These bottlenecks may turn into serious roadblocks to the continuation of the growth[2] that we have witnessed over the past years. Densely packed, high-frequency electrical interconnects suffer from severe problems: reflections due to impedance mismatch, cross-talk, signal distortion, and electromagnetic interference are difficult to overcome with increasing frequencies and densities. Optical interconnects circumvent these problems and may provide a solution to the interconnect bottleneck.

One of the key components in any parallel optical interconnection system is the array of light sources. In almost all cases one chooses diode-type devices which emit the light beam vertically to the chip, in particular VCSELs. Generally speaking, the most attractive features of VCSELs include on-wafer testing capability, mounting technology familiar from the low-cost light emitting diode market, circularly symmetric beam profiles for ease of light focusing, high-speed modulation with low driving currents, temperature insensitive operation characteristics, and obvious forming of one- or two-dimensional arrays.

To explore the future applicability of direct optical interconnection on a CMOS chip-to-chip level, University of Ulm is serving as partner in a joint European research project named *Optically Interconnected Integrated Circuits* (OIIC)[3] by fabricating the VCSEL arrays [1, 2]. Flip-chip soldering is used to hybridly integrate the optoelectronic chip epitaxial side down with silicon CMOS.

[2]See the Semiconductor Industry Association's (SIA's) *National Technology Roadmap for Semiconductors, 1999 edition*, URL http://public.itrs.net/

[3]See URL http://intec.rug.ac.be/OIIC/

Different demonstrator systems are realized within the OIIC project. Here we report on a 0.6 μm-CMOS VCSEL transmitter with 32 channels which will be used in Gb/s CMOS-to-CMOS link demonstrators.

2. VCSEL Transmitter

On the CMOS driver chip shown in Fig. 1, the main block is a 4×8 array with 16 CMOS data inputs, with the option to use an on-chip pseudo random bit sequence (PRBS) generator. Individually addressable CMOS data inputs are provided to 12 channels in the other two rows of sources. The remaining four source channels are set up with direct access, which allows the verification of the performance of the source components and connections made on flip-chip assembly. For modulation each of the lasers is shunted

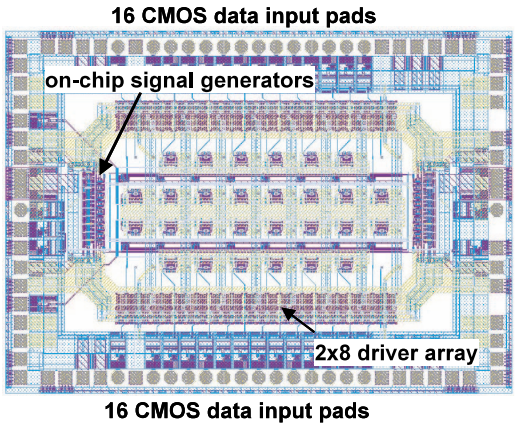

Fig. 1. CMOS VCSEL driver chip designed by ETH Zürich.

with the current I_{DC1} and a switch is used to steal the current I_{DC2}, i.e. the modulation current. It is important that the current taken from the supply is constant, i.e. it does not depend on how many optical channels are turned on or off.

Fig. 2 shows photographs of a fabricated transmitter chip where a bottom-emitting VCSEL array with 4×8 elements has been flip-chip mounted on a 0.6 μm-CMOS driver chip. The bias current of all 28 VCSELs is controlled by a single reference signal. In the left or right hand parts of Fig. 2 all lasers are biased below or above threshold, respectively. The photograph in the center part of Fig. 2 shows the transmitter chip if there is no bias applied to the VCSELs and one of the 16 on-chip PRBS generators is turned on.

Eye diagram measurements are performed by using the on-chip PRBS31 generators, a 3 GHz bandwidth DC-coupled Ge avalanche photodiode and a digital sampling scope. In Fig. 3 measured eye diagrams of 8 VCSEL channels in the first inner row of the transmitter chip at a bit rate of 1 Gb/s are depicted. 28 VCSELs on the chip are biased slightly above threshold and the 16 VCSELs of the inner rows are modulated by the 16 on-chip

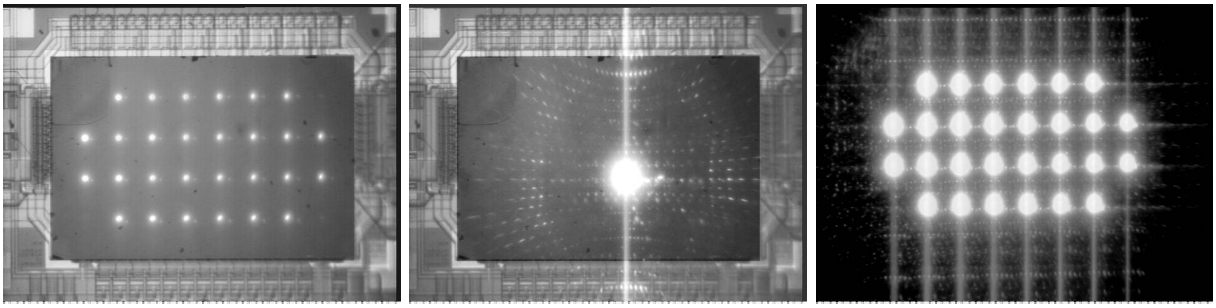

Fig. 2. 0.6 μm-CMOS VCSEL transmitter. The bias current of the 28 channels is controlled by one reference signal and can be set to below (left) or above (right) laser threshold current. VCSELs of the inner two rows can be modulated either by the on-chip PRBS generators (center) or by external CMOS signals.

generators. Good eye opening is observed. The total power consumption of the transmitter chip for these operating conditions is 365 mW resulting in 15.7 mW/ch at 1 Gb/s modulation rate. At 500 Mb/s modulation rate the dissipated power is only 5.9 mW/ch. These results indicate that the developed VCSEL based 0.6 μm-CMOS transmitter has great potential for practical use in implementing high-density and high-speed optical data links at 1 Gb/s/ch.

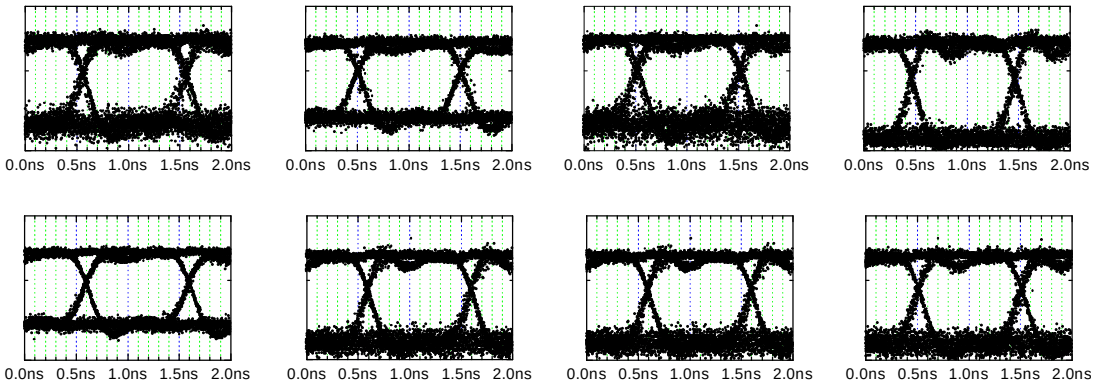

Fig. 3. Eye diagrams of 8 VCSEL-Tx outputs at 1 Gb/s operation speed. The inner 2×8 VCSELs are modulated by the 16 on-chip PRBS31 generators.

3. Conclusion

Apart from single-transmitter modules as for Gigabit Ethernet or one-dimensional parallel links, the much esteemed VCSEL capabilities are most obviously exploited in two-dimensional arrayed systems which can offer massively parallel data transmission and might thus help to avoid the electrical interconnect bottleneck to be expected in future high-performance computer environments.

In this paper, we have reported on a VCSEL based transmitter for high density CMOS-to-CMOS optical interconnection at Gb/s data rates. For the transmitters, two-dimensional VCSEL arrays of 4×8 components on a 250 μm pitch were fabricated. The lasers emit the light at 980 nm wavelength through the substrate or at 850 nm through outcoupling windows in the substrate. The III-V chips are designed for flip-chip bonding to matching pads on the 0.6 μm-CMOS driver chip. On the driver chip the main block is a 4×8 array with 28 CMOS data inputs and the option to use 16 on-chip PRBS generators. The transmitter enables CMOS-to-light signal conversion at 1 Gb/s/ch data rate and power consumption well below 20 mW/ch.

Meanwhile CMOS drivers in 0.25 μm-technology with a special pulse driver circuit are available within the OIIC consortium. A transmitter chip module with drivers in 0.25 μm-CMOS technology – shown in Fig. 4 is under investigation. It is expected to enable data rates exceeding 2.5 Gb/s.

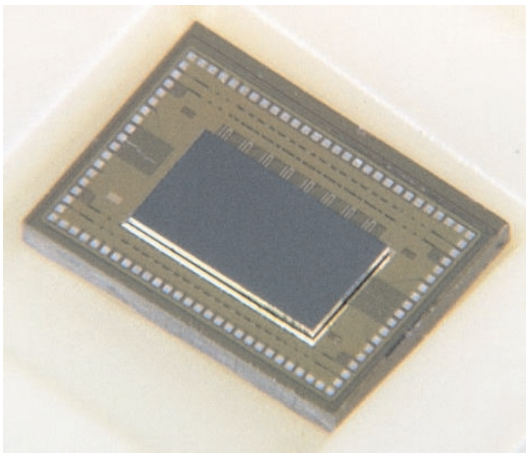

Fig. 4. 0.25 μm-CMOS VCSEL transmitter.

References

[1] L. Vanwassenhove, R. Baets, M. Brunfaut, J. Van Campenhout, J. Hall, K. J. Ebeling, H. Melchior, A. Neyer, H. Thienpont, R. Vounckx, J. Van Koetsem, P. Heremans, F.-T. Lentes, and D. Litaize, "Two-dimensional optical interconnect between CMOS IC's", in Proc. *50th Electron. Comp. & Technol. Conf., ECTC*, pp. 231–237, (Las Vegas, NV, USA), May 2000.

[2] R. Michalzik, K. J. Ebeling, M. Kicherer, F. Mederer, R. King, H. Unold, and R. Jäger, "High-performance VCSELs for optical data links", *IEICE Trans. Electron.*, vol. E84-C, No. 5, May 2001.

Data Transmission at 3 Gb/s over PCB Integrated Polymer Waveguides with GaAs VCSELs

Felix Mederer

GaAs quantum-well based vertical-cavity surface-emitting lasers (VCSEL) at 855 nm emission wavelength are investigated for intraboard polymer waveguide links. We report a 3 Gb/s pseudo random bit sequence (PRBS) non-return-to-zero (NRZ) data transmission over about 5 cm long printed circuit board (PCB) integrated multi-mode polymer waveguide arrays of two different geometries at bit-error rates (BER) of better than 10^{-11}.

1. Introduction

The bottleneck for the next generation of microprocessors with clock rates of more than 1 GHz are the power dissipation and delay time of microchips and multichip modules interconnects [1]. Even with an improved layout the maximum bandwidths and distances of conventional metal based electronic lines are limited and will not satisfy future demands for mid distance (≤ 60 cm) high-throughput (> 1 Gb/s) point-to-point interconnects [2]. Optoelectronic interconnect solutions on the other hand offer the potential for multi-Gb/s transmission over standard distances for high-speed clock and data distribution without increasing power dissipation, delay times [3] and sensitivity for electromagnetic interference (EMI) [4]. Obviously for current supply and low-bandwidth data communication electric metalized circuits are still needed on processor boards. These two demands lead to a hybrid electrical-optical board layout concept with the combined advantages of electrical strip lines and optical waveguides for high-throughput data transmission [5]. VCSELs are highly attractive light sources for low-cost, high-speed data transmission over polymer based optical intraboard waveguides. GaAs or InGaAs based VCSELs with emission at 850 nm or 980 nm wavelengths, threshold currents in the sub-100 μA range [6] and threshold voltages close to the bandgap voltage in combination with extremely high wallplug efficiencies over a large operation range [7] helping to reduce power consumption and dissipated heat in system applications. Nearly temperature independent output characteristics over a -20°C to 100°C temperature range [8], modulation bandwidths of 21.5 GHz [9] and reported single-mode emission of 5.0 mW [10] show the capability for ultra fast, low-cost optical links up to 12.5 Gb/s data rates [11].

In this paper we demonstrate 3 Gb/s data transmission over multi-mode printed circuit board integrated polymer waveguide arrays using a multi-mode GaAs VCSEL source emitting at 855 nm wavelength. Waveguide cores consist of polymer material and are 4.6 cm and 4.3 cm long, with rectangular or trapezoidal cross sectional shapes of about 0.015 mm^2 area.

2. Waveguide Characteristics

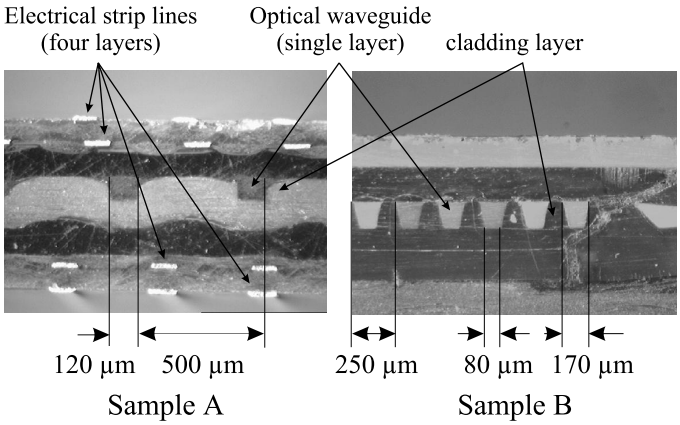

Fig. 1. Cross-sectional view of printed circuit board sample A containing an optical waveguide layer sandwiched between electrical strip layers and sample B with trapezoidal cross sectional waveguide layer.

Fig.1 shows a cross-sectional view of intraboard waveguide array sample A with a single layer of optical waveguides integrated into a four-layer electrical board and sample B with trapezoidal cross sectional shapes. To remain fully compatible with standard electrical PCB manufacturing, the waveguide materials have to withstand long term (>1h) exposure of high temperature (160°C). The waveguides are formed by a two step hot embossing process. In a first step, the waveguide cores are fabricated by using a metal master form, which contains the inverse waveguide structure in form of grooves.

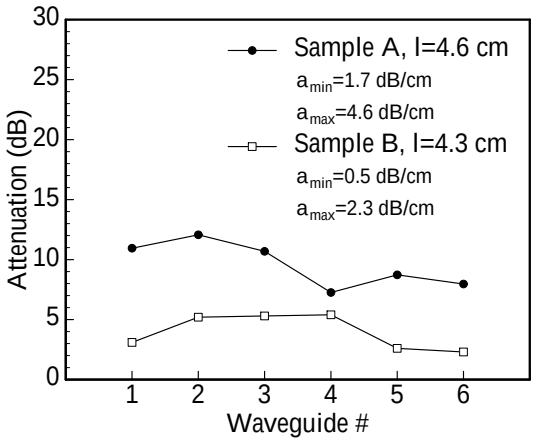

Fig. 2. Attenuation characteristics of several PCB integrated optical waveguides of sample A and B at $\lambda = 835\,\mathrm{nm}$ wavelength.

The waveguide fabrication itself is performed by pressing a high refractive index, temperature stable and highly transparent polycarbonate foil under heat and force into these

grooves. In the following second step, a low refractive index substrate foil is laminated on the waveguides. After this step the waveguide-substrate combination is removed from the metal master form and coated with an optical cladding. Waveguides in sample A are arranged at 500 μm pitch and have rectangular shapes of about $120\times130\,\mu m^2$ area. Sample B contains waveguides of trapezoidal shape arranged at 250 μm pitch.

Fig.2 shows the attenuation loss of six individual waveguides of sample A and B measured with a multi-mode VCSEL source. At a wavelength of 855 nm minimum waveguide attenuations of sample A and B are 1.7 dB/cm and 0.5 dB/cm, respectively. As a future alternative, using waveguides made of new COC polymer material with an attenuation minimum of 0.15 dB/cm at 850 nm wavelength [12], short distance (<100 cm) optical data transmission will be no longer attenuation limited.

3. VCSEL Characteristics

Top-emitting selectively oxidized GaAs based 855 nm emission wavelength VCSELs are fabricated using solid source molecular beam epitaxy. The bottom $Al_{0.9}Ga_{0.1}As$/ $Al_{0.1}Ga_{0.9}As$ distributed Bragg reflector (DBR) consists of 37 n-type Silicon doped layer pairs. The active region contains three 8 nm thick GaAs quantum-wells embedded in $Al_{0.2}Ga_{0.8}As$ spacer layers to provide efficient carrier confinement. The top DBR consists of 19 Carbon doped $Al_{0.9}Ga_{0.1}As$-$Al_{0.1}Ga_{0.9}As$ layer pairs. For current confinement a selectively oxidized 30 nm thick AlAs layer is inserted in the top mirror. Planarizing polyimide passivation is used to reduce bondpad capacitance. The laser is wire-bonded from a Ti/Au bondpad to an SMA socket to keep feeding lines as short as possible.

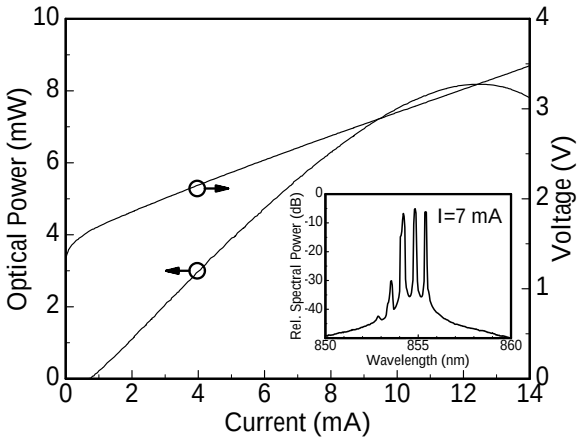

Fig. 3. Output characteristics for a laterally oxidized GaAs VCSEL of 8 μm active diameter.

Output characteristics of the VCSEL with an active diameter of 8 μm are given in Fig.3. Threshold current is as low as 0.8 mA and the maximum output power is 8.2 mW at a current of 12 mA. The CW emission spectrum for 7 mA driving current is given in the inset of Fig.3. The multi-mode emission is centered at 855 nm wavelength.

4. Data Transmission Results

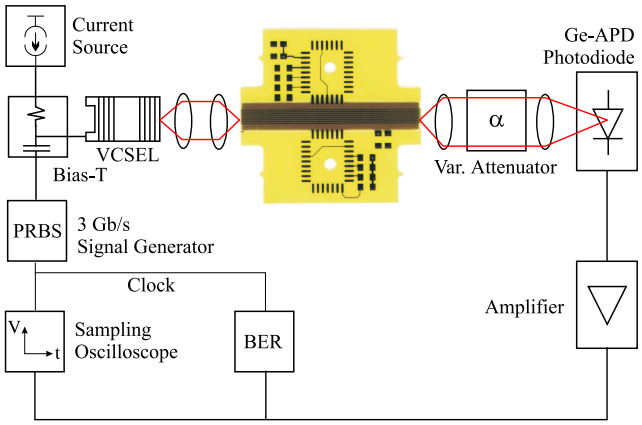

Fig. 4. Setup for data transmission experiments.

The setup for data transmission experiments is indicated in Fig.4. The VCSEL is biased at 7 mA current and modulated with a 1.5 V_{pp} PRBS signal. After transmission through the waveguides the optical signal is passed through a variable attenuator and detected with a 50 μm diameter Germanium avalanche photodiode of 2 GHz bandwidth using demagnifying imaging. The amplified digital signal is monitored with an electrical sampling oscilloscope and analyzed with a BER detector.

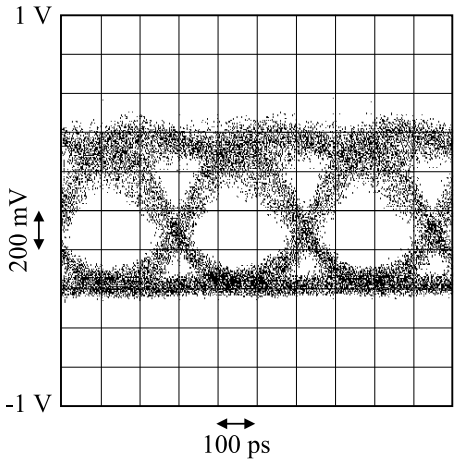

Fig. 5. Eye diagram recorded for 3 Gb/s PRBS of $2^{31} - 1$ word length over sample A.

Fig.5 illustrates the eye diagram for 3 Gb/s PRBS modulation recorded after transmission over a waveguide of sample A. The eye is symmetric and without any significant relaxation oscillations. Similarly, the eye diagrams for the other waveguides on sample A or sample B show no significant differences to Fig.5.

Fig.6 shows the results of the transmission experiments where the BER is plotted versus the received optical power. For 3 Gb/s PRBS NRZ signals of $2^{31} - 1$ word length the

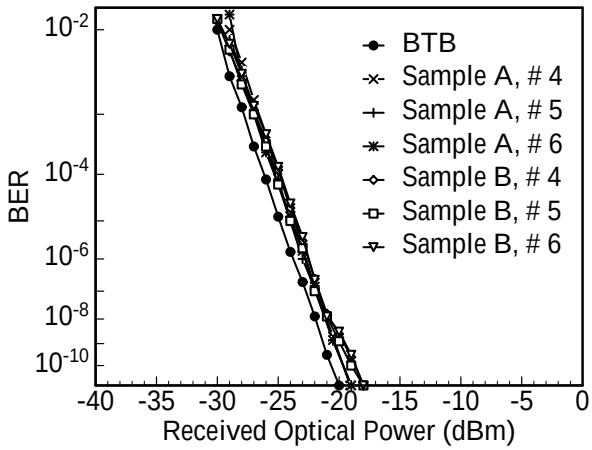

Fig. 6. BER recorded for 3 Gb/s PRBS of $2^{31} - 1$ word length.

received optical power for a BER of 10^{-11} is -20 dBm under back-to-back operation (BTB, filled circles). For sample A a power penalty of 1 dB is found for transmission over waveguides 4,5 and 6 (crosses, pluses and stars). Using sample B, the power penalty for a BER of 10^{-11} is 2 dB for waveguides 4, 5 and 6 (diamonds, rectangles and down-triangles).

5. Conclusion

We have successfully demonstrated VCSEL based error-free 3 Gb/s data transmission over highly multi-mode intraboard polymer optical waveguides. Using optimized fabrication technology still compatible with standard PCB manufacturing we have achieved waveguide losses as low as 0.5 dB/cm at 855 nm wavelength. Even lower losses obtaining quite recently indicate that mode dispersion rather than waveguide attenuation is of primary concern for extremely high bandwidth, e.g. 10 Gb/s, intraboard optical interconnects when transmission distances of several ten cm length are to be considered .

Acknowledgments

The authors would like to acknowledge the support by the German Ministry of Research (BMBF) and the German Research Foundation (DFG). The lamination of the waveguide foils into the printed circuit boards has been accomplished by ILFA, Hannover.

References

[1] B. Wittmann, M. Jöhnck, A. Neyer, F. Mederer, R. King, and R. Michalzik , "POF-Based Interconnects for Intracomputer Applications", *IEEE J. Sel. Topics in Quantum Electron.,* vol. 5, pp. 1243–1248, 1999.

[2] F.E. Kiamilev, P. Marchand, A.V. Krishnamoorthy, S.C. Esener, and S.H. Lee , "Performance Comparison Between Optoelectronics and VLSI Multistage Interconnection Networks ", *IEEE J. Lightwave Technol.,* vol. 9, pp. 1674–1692, 1991.

[3] H. Karstensen, C. Hanke, M. Honsberg, J.-R. Kropp, J. Wieland, M. Blaser, P. Weger, and J. Popp , "Parallel Optical Interconnection for Uncoded Data Transmission with 1 Gb/s-per-Channel Capacity, High Dynamic Range, and Low Power Consumption", *IEEE J. Lightwave Technol.,* vol. 13, pp. 1017–1030, 1995.

[4] B. Bihari, J. Gan, L. Wu, Y. Jiu, S. Tang, and R.T. Chen, "Optical Clock Distribution in Supercomputers using Polyimide-based Waveguides", in Proc. SPIE'99, San Jose, California, USA, 1999, pp. 123–133.

[5] E. Griese, "Reducing EMC Problems Through an Electrical/Optical Interconnect Technology", *IEEE Transactions on Electromagnetic Compatibility,* vol. 41, pp. 502–508, 1999.

[6] D.G. Deppe, D.L. Huffaker, T. Oh, H. Deng, and Q. Deng, "Low-threshold vertical-cavity surface-emitting lasers based on oxide-confined and high contrast distributed Bragg reflectors", *IEEE J. Sel. Topics Quantum Electron.*, vol. 3, pp. 893-904, 1997.

[7] R. Jäger, M. Grabherr, C. Jung, R. Michalzik, G. Reiner, B. Weigl, and K.J. Ebeling, "57 % wallplug efficiency oxide-confined 850 nm wavelength VCSELs", *Electron. Lett.,* vol. 33, pp. 330–331, 1997.

[8] F. Mederer, M. Kicherer, R. Jäger, H. Unold, and K.J. Ebeling, "2.5 Gb/s data transmission with single-mode GaAs VCSELs over -20 to 100°C temperature range", *Electron. Lett.,* vol. 36, pp. 236–238, 2000.

[9] K.L. Lear, V.M. Hietala, H.Q. Hou, M. Ochiai, J.J. Banas, B.E. Hammons, J.C. Zolper, and S.P. Kilcoyne, "Small and large signal modulation of 850 nm oxide-confined vertical cavity surface emitting lasers", *OSA Trends in Optics and Photonics,* vol. 15, pp. 69–74, 1997.

[10] H.J. Unold, S. Mahmoud, F. Eberhard, R. Jäger, and K.J. Ebeling, "Large-Area Single-Mode Selectively Oxidized VCSELs: Approaches and Experiments", *in Proc. SPIE Photonics West*, vol. 3946, pp.207-208, San Jose, USA, 2000.

[11] F. Mederer, C. Jung, R. Jäger, M. Kicherer, R. Michalzik, P. Schnitzer, D. Wiedenmann, and K.J. Ebeling, "12.5 Gb/s data rate fiber transmission using single-mode selectively oxidized GaAs VCSEL at $\lambda = 850$ nm", *in Proc. LEOS Annual Meeting 1999*, vol.2, pp.697-698, San Francisco, USA, 1999.

[12] S. Lehmacher and A. Neyer, "Integration of polymer optical waveguides into printed circuit boards (PCB)", *in Proc. VDE World Microtechnologies Congress 2000*, B 1.1, Hannover, Germany, 2000.

Towards Single-Mode VCSEL Arrays for 10 Gb/s Data Links

Max Kicherer

Vertical-cavity lasers at 850 nm emission wavelength, designed and fabricated for high-speed operation, are used for 10 Gb/s and 12.5 Gb/s data transmission using pseudo-random-bit-sequence (PRBS) signals of different word length. Solitary single- and multi-mode devices as well as linear 1×10 arrays of single-mode devices are tested on wafer for their high-speed performance.

1. Introduction

Since IEEE's P802.3ae 10 Gb/s Ethernet Task Force adopted an 850 nm wavelength option in the physical media dependent layer standard for short range optical data links, the interest in this field has greatly increased. Owing to the surface-normal operation and many other favorable properties, like low power dissipation, high-speed modulation, and Si IC compatible low-cost manufacturing, vertical-cavity surface-emitting lasers (VCSELs) are going to be the preferred choice for the transmitter part. Single channel as well as one-dimensional fiber ribbonized parallel interconnect modules for data rates up to a few Gb/s per channel using VCSELs are already on the market [1, 2, 3]. Here we study single- and multi-mode selectively oxidized VCSELs emitting at 850 nm wavelength for very high speed operation. Solitary devices as well as linear arrays are characterized.

2. Properties of Solitary Devices

Fig. 1 shows the continuous wave (CW) output characteristics of a VCSEL emitting at 846 nm wavelength. Threshold current and threshold voltage are 0.4 mA and 1.7 V, respectively. The differential resistance approaches 207 Ω for higher operating currents. Thermal rollover starts at about 3 mA due to the small active diameter of 2 μm. The maximum optical output power of 3.2 mW is reached at an operating current of 7 mA. The inset shows optical spectra for various operating currents. Up to 2.5 mA the emission remains single-mode with a side mode suppression ratio of more than 30 dB. The modulation efficiency of 7.4 GHz/$\sqrt{\text{mA}}$ is obtained by fitting theoretical curves to measured small-signal modulation response data. For 1.5 mA bias current a 3 dB modulation bandwidth of 9 GHz is determined.

A multi-mode laser with an active diameter of 5 μm was investigated as well. Emission occurs around 843 nm in 4 to 5 transverse modes. Threshold current and threshold voltage are 0.87 mA and 1.6 V, respectively. The differential resistance is as low as 86 Ω. At 15 mA a maximum output power of 8 mW is reached. Small signal modulation response measurements yield a maximum modulation bandwidth of 8.5 GHz at a corresponding modulation efficiency of 5.2 GHz/$\sqrt{\text{mA}}$.

In Fig. 2 the bit error rate (BER) for 12.5 Gb/s pseudo random bit sequence (PRBS) modulation of word length $2^7 - 1$ is plotted against the received optical power for both lasers described above. Measurements are performed using an InGaAs PIN photodetector (supplied by Optospeed SA) of 0.4 A/W sensitivity in a back-to-back transmission setup. For the single-mode device bit error rates below 10^{-11} are reached for a received optical power of -11.7 dBm when the laser is biased at a current of 1.3 mA. The multi-mode device shows a minor power penalty of 1.5 dB at a bias of 10 mA for the same BER level.

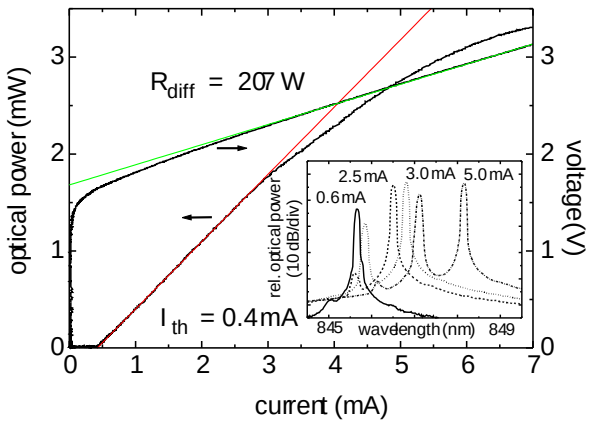

Fig. 1. CW operation characteristics and optical spectra of a single-mode VCSEL of 2 μm active diameter.

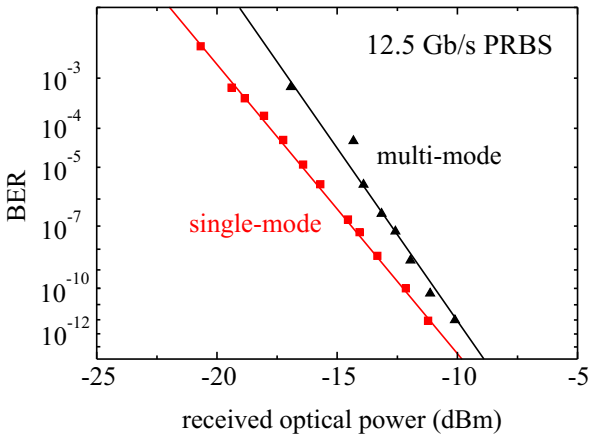

Fig. 2. BER vs. received optical power for a single-mode (squares) and a multi-mode (triangles) VCSEL.

Fig. 3 shows the bit error rate for a solitary laser diode operated at similar bias conditions for two pseudo random bit sequences of different word length at 10 Gb/s data rate. The general decrease in required optical power for a BER of 10^{-9} by about 2 dB in comparison to Fig. 2 is due to the use of an improved photodetector system comprising a PIN photodiode and a transimpedance amplifier (Picometrix AD50xr). The laser under study shows a threshold current of 0.42 mA and emits at 865 nm wavelength. The active diameter of the device is about 3 μm. It reaches a maximum output power of 800 μW at ten times threshold. Compared to the laser presented in Fig. 1 this structure shows reduced optical output power due to the increased number of top mirror pairs.

During modulation the device was biased at about four times threshold. The modulation voltage was adjusted for minimum BER performance. The minimum on/off-ratio was found to be around 5 dB using an optical sampling oscilloscope. In the case of $2^{31} - 1$ PRBS word length the on/off-ratio was strongly dependent on the previously transmitted

information. This causes the power penalty of about 2 dB compared to the shorter word length case. Closer analysis shows this to be due to reflections on the electrical line feeding the laser because of the high differential resistance of about 470 Ω in comparison to the 50 Ω output impedance of the signal generator.

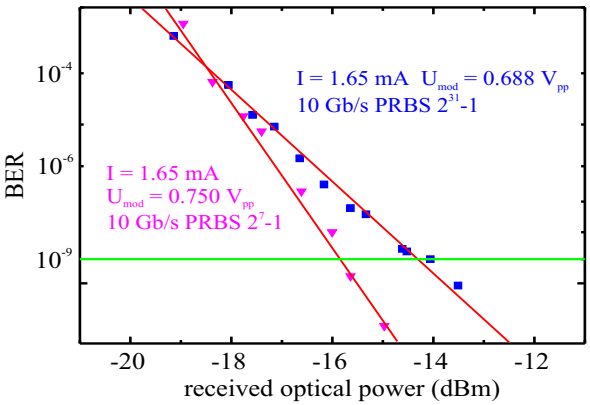

Fig. 3. BER vs. received optical power for a single-mode VCSEL modulated with a $2^7 - 1$ (triangles) and a $2^{31} - 1$ (squares) PRBS signal. Bias current and modulation voltage are only slightly different.

3. Characterization of Arrays

Fig. 4 shows a plot of the threshold current for 10 adjoining lasers. The emission wavelengths vary from 859 nm for laser #1 to about 854 nm for laser #10. All devices have about 2.5 μm active diameter and show a side mode suppression ratio of about 30 dB for the complete operating range.

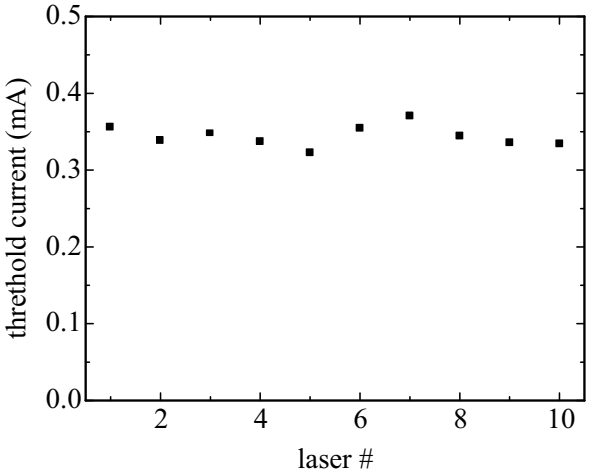

Fig. 4. Threshold current of 10 neighboring single-mode VCSELs of 2.5 μm active diameter.

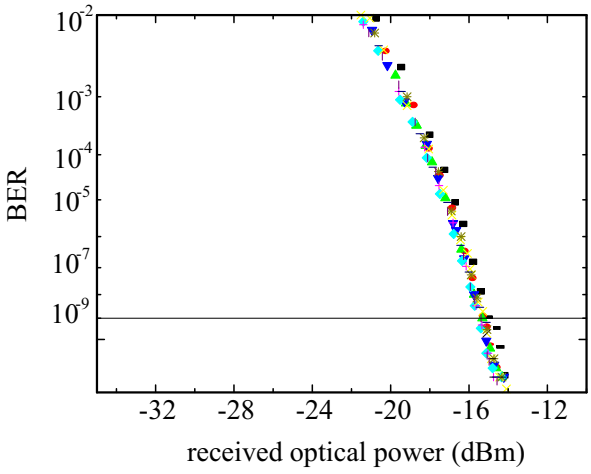

Fig. 5. BER vs. received optical power for a linear array of 10 single-mode VCSELs.

In Fig. 5 the bit error rates for 10 Gb/s pseudo random bit sequence modulation of word length $2^7 - 1$ are plotted against the received optical power for the same 10 lasers presented

above. Each laser was biased at around four times threshold for the data transmission experiments. The modulation voltage was adjusted for minimum BER performance between 0.6 and 0.8 V_{pp} from a 50 Ω output impedance signal generator. For detection of the optical signal a photodetector system comprising a PIN photodiode and a transimpedance amplifier was used. An additional electrical 27 dB gain amplifier was used to measure BER and eye diagrams.

The lasers show no variation in modulation behavior with this setup. Small-signal modulation response measurements show 3 dB bandwidths of around 7 GHz for these lasers, preventing an increase in data rate.

4. Conclusion

In conclusion we have fabricated linear 1×10 VCSEL arrays capable of carrying a total data stream of 100 Gb/s. All measurements were taken at room temperature. Different environmental conditions as well as aging effects remain to be investigated.

References

[1] K. Drögemüller, D. Kuhl, J. Blank, M. Ehlert, T. Kraeker, J. Höhn, D. Klix, V. Plickert, L. Melchior, I. Schmale, P. Hildebrandt, M. Heinemann, F.P. Schiefelbein, L. Leininger, H.-D. Wolf, T. Wipiejewski, A. Ebberg "Current Progress of Advanced High Speed Parallel Optical Links for Computer Clusters and Switching Systems", in *50th Electron. Comp. and Technol. Conf., ECTC 2000*, pp. 1277–1235, Las Vegas, Nevada, USA, May 2000.

[2] http://www.mitelsemi.com/products/download_details.cgi?partno=MFT62340-J

[3] V. Jayaraman, M. Soler, T. Goodwin, M.J. Culik , T.C. Goodnough, M.H. MacDougal, F.H. Peters, D. VanDeusen, and D. Welch "Optically Pumped 1.3 μm VCSELs", in *2000 Conference on Lasers and Electro-Optics Europe, CLEO/Europe 2000*, paper CThK3, Nice, France, September 2000.

Four-Channel Coarse WDM 40 Gb/s Transmission of Short-Wavelength VCSEL Signals Over High-Bandwidth Silica Multi-Mode Fiber

Rainer Michalzik

The first experiment is reported to demonstrate the ability of upgrading future enterprise networks to building backbone speeds of 40 Gb/s carried by a single graded-index silica multi-mode fiber (MMF). We have used 20 nm total span coarse wavelength division multiplexing of four VCSEL channels centered at 825 nm and modulated at 10 Gb/s each for error-free data transmission over a recently developed high-performance MMF with 310 m link length.

1. Introduction

The continuous increase of required data rates in local area networks (LANs) beyond the capacity of current protocol platforms like Gigabit Ethernet (GbE) has urged the establishment of a so-called Higher Speed Study Group within the IEEE in March 1999. These early efforts have resulted in focused work toward the successor of GbE, meanwhile known under [1] 10-Gigabit Ethernet (10-GbE) to be standardized as IEEE 802.3ae. Several options exist to reach the target data rate on the order of 10 Gb/s. Coarse wavelength division multiplexing (CWDM) is an attractive option for increasing the data throughput while utilizing the often low-bandwidth installed MMF base. CWDM modules based on 840 nm wavelength vertical-cavity surface-emitting lasers (VCSELs) [2] or 1310 nm distributed feedback lasers [3] have already been developed, enabling 4×2.5 Gb/s transmission over 100 m MMF or 300 m MMF, respectively, both with 62.5 μm core diameter. However, recent demonstrations of 10 Gb/s VCSEL transmitters and MMF receivers together with the progress of SiGe electronics clearly show the feasibility of a straight forward serial high-speed solution without the added complexity of optical multi- and demultiplexing. Indeed, recently 10 Gb/s data transmission over record distances of 1.6 km [4] or 2.8 km [5] of a new high-bandwidth 50 μm core diameter MMF have been reported. Subcarrier multiplexing and multilevel coding [6] as alternative upgrading methods have not yet been demonstrated in sufficient quality and are not considered competitive at present. Likewise, today's parallel optical modules with already up to 30 Gb/s aggregate data rate through 12 channels [7] seem unsuitable due to high cost of a few hundred meter long fiber ribbon cable. With a further increase of bandwidth demand beyond the direct current modulation capabilities of laser transmitters, CWDM approaches will certainly gain importance for building backbone links. In this paper we present a first realization of a four-channel, 40 Gb/s CWDM link over 310 m of high-performance MMF cable [8].

2. Experimental Setup

The present CWDM transmission system is implemented in a hybrid fashion. In the transmitter section, each two of the four VCSEL outputs are combined through a polarizing beam splitter (PBS) to reduce the regular 3 dB loss contribution. Maximum power transmission is achieved by proper rotation of the fixed polarization of the single transverse mode beams by means of half-wave plates. Both beams are then combined by a 3 dB MMF coupler that is connected to the 310 m length cabled and connectorized LazrSPEED^{TM} MMF with 50 μm core diameter from Lucent Technologies. Fiber loss including one ST-type fiber connection is slightly below 1 dB. The fiber output is collimated, dispersed through a 850 nm, 400 lines/mm blazed grating, attenuated with a circular variable neutral density filter, and fed into a fiber pigtailed pin-receiver. For demultiplexing, the coupling unit is translated perpendicularly to the beam. Total fiber-to-fiber loss is below 3 dB for the demultiplexer. The electrical signal is amplified by 28 dB and analyzed by a bit error rate tester (BERT). The VCSELs are driven by the DATA and inverse DATA outputs of the BERT, where differing cable lengths ensure signal decorrelation.

3. Laser Source Characteristics

High-speed GaAs quantum well based oxide-confined transverse singlemode VCSELs [9] with emission wavelengths of 815, 822, 828, and 835 nm were selected from a molecular beam epitaxially grown wafer with intentional grading of layer thicknesses. 10 Gb/s signals drive the VCSELs through SMA-connectorized packages containing a coplanar stripline which is wire-bonded to the ground-signal-ground contacts of the laser. As shown in Fig. 1, threshold currents vary between 0.6 and 0.85 mA. At 3 mA bias, free-space optical powers between 1.15 and 1.45 mW are delivered.

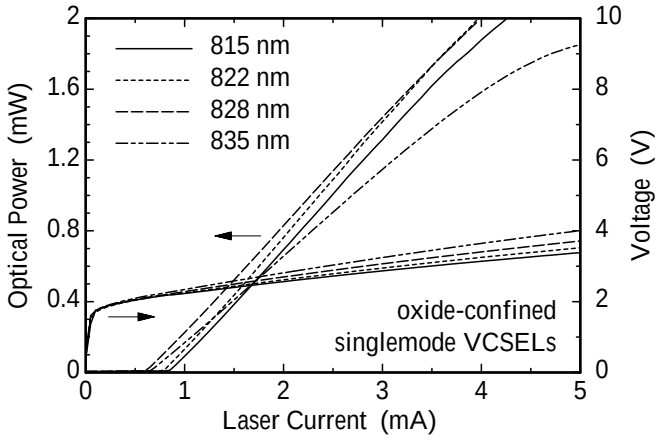

Fig. 1. VCSEL operation characteristics for all four WDM channels.

For the 815 nm device, the optical spectra in Fig. 2 reveal that the sidemode suppression ratio (SMSR) exceeds 40 dB at 3 mA and is reduced to still 30 dB at 4 mA current, corresponding to 1.85 mW output power. The active laser size is defined through the diameter of the oxide aperture which is in the range of 3 to 4 μm.

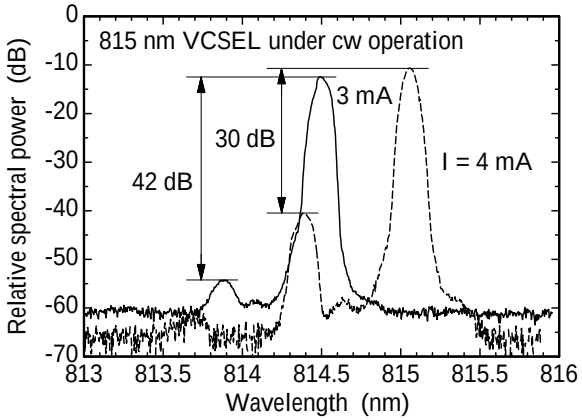

Fig. 2. Optical spectra of the 815 nm device for 3 and 4 mA driving currents.

Since the chosen method of homogeneous layer thickness variation on the wafer also affects the AlAs current aperture, the increase of oxidation rate has resulted in smaller activce diameters for longer wavelength devices. In the multiplexed spectrum depicted in Fig. 3, this effect translates into smaller transverse mode spacings and reduced SMSRs of shorter wavelength VCSELs.

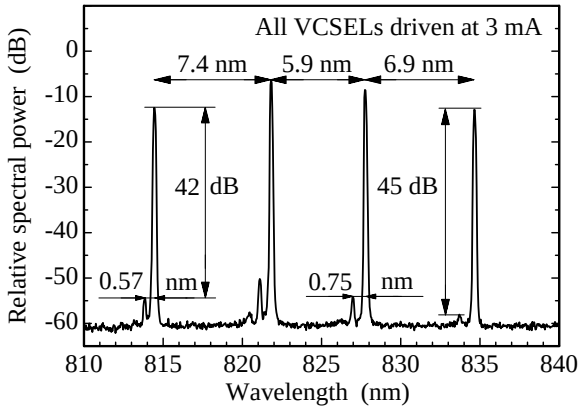

Fig. 3. Combined spectrum of the CWDM VCSEL source with all elements driven at 3 mA current.

4. Data Transmission Results

For the transmission experiment, all VCSELs were biased at 3 mA using bias tees. Owing to slightly varying differential resistances and quantum efficiencies, as seen in Fig. 1, optimum conditions were achieved with different modulation voltages. Signals with the following peak-to-peak voltages were incident onto the VCSEL packages: 1.12 V for the 815 nm wavelength channel, 1.35 V for 828 nm, and 1.56 V for 822 and 835 nm. With all four channels operating, an optical power of -0.25 dBm was launched into the fiber.

Fig. 4 illustrates measured bit error rates (BERs) for all channels at 10 Gb/s modulation as a function of average received optical power both with and without inserting the 310 m long MMF cable. In all cases, error rates down to 10^{-12} are achieved without indications

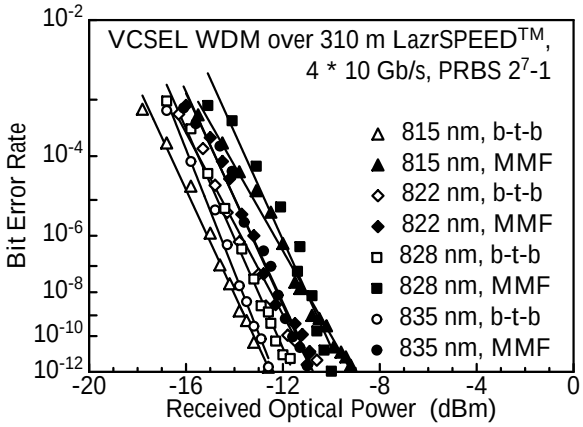

Fig. 4. Bit error rates for all four channels versus optical power at the receiver for 10 Gb/s back-to-back (b-t-b) operation and transmission over 310 m of 50 μm core diameter MMF cable.

of a BER floor. Power penalties for fiber transmission vary between 1 and 3 dB. Compared to previous publications [4, 5], where receiver sensitivities between -17.5 to -17 dBm at BER $= 10^{-9}$ have been observed, values in the range of -13.5 to -12 dBm can be extracted from Fig. 4 for back-to-back operation, although measurements were performed with the same pin-receiver. Some of this penalty can certainly be attributed to electrical parasitics introduced by the laser package (previous experiments employed direct microwave probing of the VCSEL chip), whereas we assign the largest contribution to polarization noise. Although the VCSEL's fundamental modes were linearly polarized, at least within the about 30 dB extinction ratio limit of the employed polarizer, the higher transverse order modes from Fig. 3 in any case are polarized perpendicularly to the zero order modes. These modes are dropped in the PBS which induces excess laser noise. The contribution of this effect could be quantified by repeating the experiment with regular 3 dB beam splitters. Variations of the fiber response with wavelength might also give rise to part of the observed channel-to-channel fluctuations.

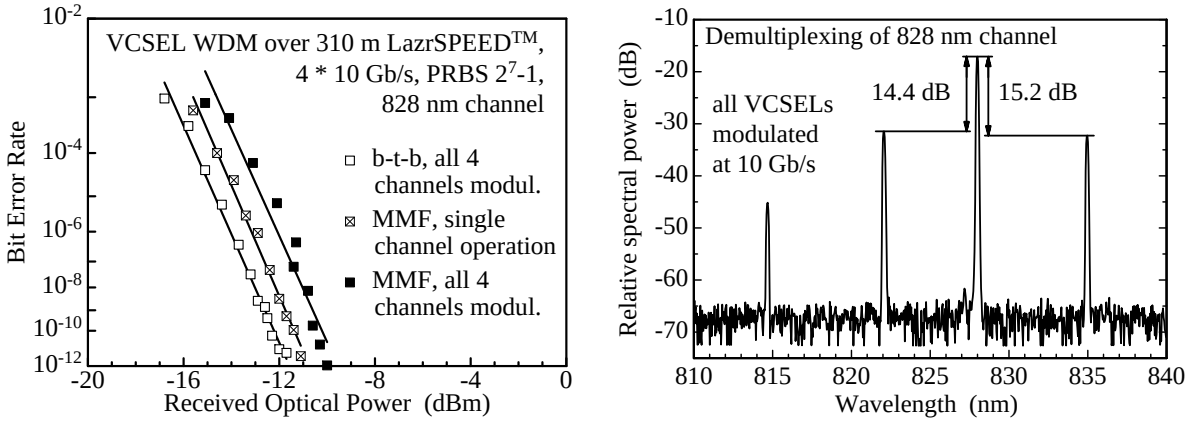

Fig. 5. Bit error rates **(left)** and received optical spectrum **(right)** during measurement of the 828 nm channel, illustrating the influence of optical crosstalk.

Fig. 5 repeats the error rate behavior of the 828 nm channel and shows an additional curve

for the case of the other three channels being switched off. The power penalty of 1 dB for full system operation can be attributed to optical crosstalk induced by the relatively low neighboring channel suppression of about 15 dB, as seen in the right-hand part of Fig. 5. In the present set-up, crosstalk can be easily reduced by increasing the path length between grating and pick-up fiber.

5. Conclusions

Relying on single transverse mode, single polarization VCSELs emitting in the 815 to 835 nm wavelength range we have successfully demonstrated the first 40 Gb/s MMF system by multiplexing 4 CWDM optical channels operating at 10 Gb/s each. Instrumental for this experiment was the availability of a high-bandwidth MMF with an improved representation of a parabolic graded-index profile, thus minimizing the group delay differences between the multiple guided modes for a certain target wavelength. The mismatch between the optimization wavelength of 850 nm and the actually used wavelength interval clearly indicates a wide spectral range of fiber bandwidth sufficient for 10 Gb/s data rates, so that either a higher channel count could be realized or the channel spacing could be increased to, e.g. 15 nm, as would be required to ensure a stable operation of uncooled components over an extended temperature range. The present demonstration thus opens up new perspectives for the realization of higher throughput building backbone links even beyond the aims of the upcoming 10-GbE standard. A more compact system configuration can be achieved with integrated multiplexing units like in [2] and [10] as well as a dielectric filter based demultiplexer [11, 3].

Acknowledgments

The experiments were carried out at Bell Labs, Lucent Technologies, Holmdel, NJ and would not have been possible without the help of G. Giaretta, A.J. Ritger, K.W. Goossen, J.A. Walker, A.L. Lentine, and M.C. Nuss.

References

[1] See URL http://grouper.ieee.org/groups/802/3/ae

[2] L.B. Aronson, B.E. Lemoff, L.A. Buckman, and D.W. Dolfi, "Low-cost multimode WDM for local area networks up to 10 Gb/s", *IEEE Photon. Technol. Lett.* **10**, pp. 1489–1491, 1998.

[3] B.E. Lemoff, L.A. Buckman, A.J. Schmit, and D.W. Dolfi, "A compact, low-cost WDM transceiver for the LAN", in Proc. *50th Electron. Comp. & Technol. Conf., ECTC*, pp. 711–716. Las Vegas, NV, USA, May 2000.

[4] R. Michalzik, G. Giaretta, A.J. Ritger, and Q.L. Williams, "10 Gb/s VCSEL based data transmission over 1.6 km of new generation 850 nm multimode fiber", *IEEE Lasers and Electro-Opt. Soc. Ann. Meet., LEOS '99*, postdeadline paper PD1.6. San Francisco, CA, USA, Nov. 1999.

[5] G. Giaretta, R. Michalzik, and A.J. Ritger, "Long distance (2.8 km), short wavelength (0.85 μm) data transmission at 10 Gb/sec over new generation high bandwidth multimode fiber", *Conf. on Lasers and Electro-Opt., CLEO 2000*, postdeadline paper CPD13. San Francisco, CA, USA, May 2000.

[6] R.V. Penty, M. Webster, A.B. Massara, and I.H. White, "Physical layer strategies for 10 Gigabit Ethernet", in Proc. *50th Electron. Comp. & Technol. Conf., ECTC*, pp. 487–490. Las Vegas, NV, USA, May 2000.

[7] K. Drögemüller, D. Kuhl, J. Blank, M. Ehlert, T. Kraeker, J. Höhn, D. Klix, V. Plickert, L. Melchior, I. Schmale, P. Hildebrandt, M. Heinemann, F.P. Schiefelbein, L. Leininger, H.-D. Wolf, T. Wipiejewski, and A. Ebberg, "Current progress of advanced high speed parallel optical links for computer clusters and switching systems", in Proc. *50th Electron. Comp. & Technol. Conf., ECTC*, pp. 1227–1235. Las Vegas, NV, USA, May 2000.

[8] R. Michalzik, G. Giaretta, K.W. Goossen, J.A. Walker, and M.C. Nuss, "40 Gb/s coarse WDM data transmission with 825 nm wavelength VCSELs over 310 m of high-performance multimode fiber", in Proc. *26th Europ. Conf. on Opt. Commun., ECOC '2000* **4**, pp. 33–34. Munich, Germany, Sept. 2000.

[9] D. Wiedenmann, R. King, C. Jung, R. Jäger, R. Michalzik, P. Schnitzer, M. Kicherer, and K.J. Ebeling, "Design and analysis of single-mode oxidized VCSEL's for high-speed optical interconnects", *IEEE J. Sel. Top. Quantum Electron.* **5**, pp. 503–511, 1999.

[10] S.-Y. Hu, S.Z. Zhang, J. Ko, J.E. Bowers, and L.A. Coldren, "1.5 Gb/s/channel operation of multiple-wavelength vertical-cavity photonic integrated emitter arrays for low-cost multimode WDM local-area networks", *Electron. Lett.* **34**, pp. 768–770, 1998.

[11] B.E. Lemoff, L.B. Aronson, and L.A. Buckman, "Zigzag waveguide demultiplexer for multimode WDM LAN", *Electron. Lett.* **34**, pp. 1014–1016, 1998.

Optically-Pumped Surface-Emitting Lasers

Eckart Schiehlen

Conventional edge-emitting single-mode semiconductor lasers have limitations in beam quality for high output power and a very high optical intensity at the facets. Single-mode VCSELs (Vertical-Cavity Surface-Emitting Lasers) show an almost perfect beam profile but the maximum single-mode output power is limited to approximately 6 mW at present time. OPS-VECSELs (Optically-Pumped Semiconductor VECSEL) also referred to as DP-VECSELs (Diode-Pumped VECSEL) show excellent beam characteristics in combination with possibly high output power. In this paper, we present first results on the epitaxial growth and the characterization of an OPS-VECSEL.

1. Introduction

Edge-emitting lasers do not emit in the fundamental mode at high optical output power [1] because of inhomogeneous electrical pumping, short axial mode distance and thermal effects inside the active region. Unavoidable intensity variations inside the laser diode (filamentations) are jointly responsible for Catastrophic Optical Mirror Damage (COMD). COMD occurs suddenly and destroys the laser diode facet. The beam profile of edge-emitting lasers is highly asymmetric. Conventional surface-emitting lasers (VCSELs) have a circular symmetric gaussian beam profile but single mode operation can achieved only for small active diameters and is limited to approximately 6 mW at present time [2, 3]. For increased active diameters, multiple transverse modes occur. Furthermore, the wallplug efficiency is decreasing significantly because of thermal heating. Additionally, homogeneous carrier injection is not possible for larger active diameters.

The new concept of VECSELs combines properties of conventional edge-emitting and surface-emitting lasers. VECSELs are pumped optically, mostly by a high-power edge-emitting laser. So, they can be pumped homogeneously or with an optimized pump profile. For the TEM_{00} mode, this will be circular symmetric gaussian intensity distribution which corresponds to the laser-mode intensity distribution. Optical pumping up to now is used to pump solid state laser systems. But solid state laser materials like Nd:YAG are emitting only at material specific wavelengths. With semiconductor laser material, the emitting wavelength can be "designed" in the range which is covered by the semiconductor material system. A big advantage is the power scalability of the VECSEL technology. The resulting output power corresponds directly to the pumped active area [4, 5]. An advantage to solid state lasers is the broad absorption spectrum and the very strong absorption coefficient

of semiconductor material. A VECSEL does not need electrical contacts or doping of the semiconductor material. This makes manufacturing technology rather easy.

The main advantage here is the external cavity with an optical power which is by orders of magnitude higher than the output power. Such an external cavity can be used for frequency doubling or absorption spectroscopy for example. Very short pulses with high average power levels could be generated by establishing saturable absorbers inside the cavity.

2. System Setup and VECSEL Structure

As shown in Fig. 1 the VECSEL chip is mounted on a heat sink and is forming a resonator together with an external concave mirror. The laser pump beam is focused onto the chip at an angle of about 45 °, it should ideally result in a round spot.

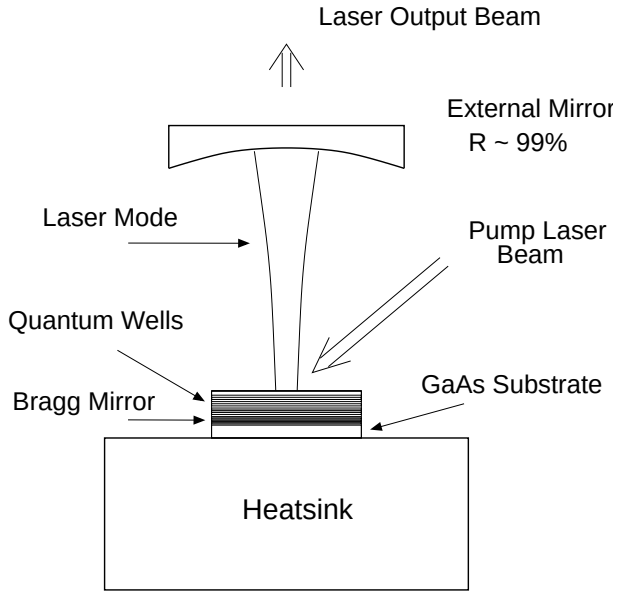

Fig. 1. VECSEL principle setup. The laser cavity is formed by a Bragg mirror and an external dielectric mirror. Pumping of the gain medium (InGaAs quantum wells) is done optically by a laser beam.

The laser cavity is formed by an AlAs/GaAs Bragg mirror which is grown directly on the GaAs substrate and an external concave dielectric mirror. Because of the short gain medium length, the external mirror reflectivity has to be $\geq 99\,\%$. The bragg mirror should exceed 99.9 % to avoid additional losses. A stable resonator configuration is used here. The length of the laser cavity is variable but depends on the mirror radius of course. The epitaxial structure is a classical Resonant Periodic Gain (RPG) structure [6, 7].

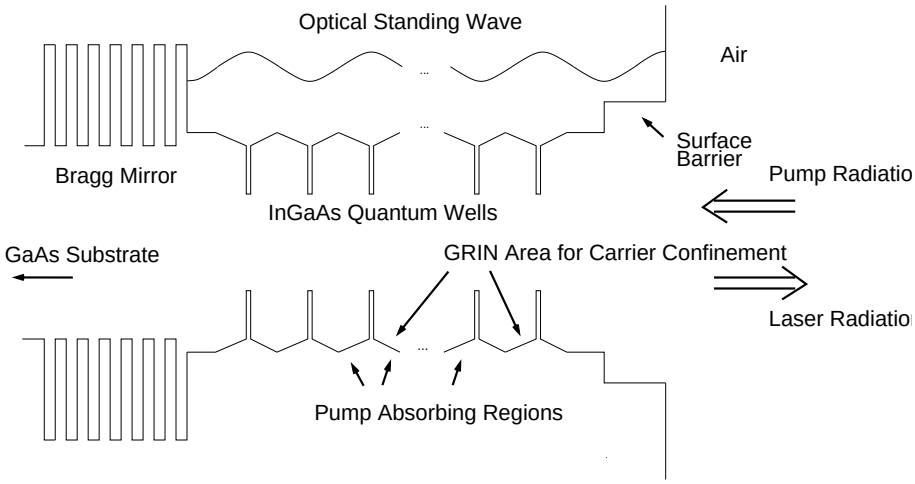

Fig. 2. VECSEL energy diagram. On a GaAs substrate, the Bragg mirror is grown followed by the quantum wells and the surface barrier.

Fig. 2 shows the energy diagram and the resulting standing wave for a VECSEL structure. The carriers are generated by absorption of the pump light in the GaAs and AlGaAs absorbing layers. These carriers relax into the InGaAs quantum wells and are recombining stimulated. The very strong absorption coefficient of the semiconductor materials yields for the pump light to short absorption lengths of only a few micrometers. The absorbing layers are realized as GRaded-INdex (GRIN) areas to support the carrier movement into the quantum-wells. A standing wave is built up within the resonator with the intensity maxima located in the quantum-well regions. A surface barrier made of AlGaAs with an Al content of 30 % prevents excited carriers from recombining at the wafer surface. This surface barrier layer is transparent for the pump wavelength. Optical absorption (of photons of the emission wavelength) is reduced because the epitaxial layers don't have to be doped. No electrical contacts are necessary so no additional heat of the ohmic contacts is added which rises the device temperature and reducees the conversion efficiency.

3. First Results

An epitaxial wafer with an InGaAs/AlGaAs VECSEL structure as specified above has been grown and characterized by photoluminescence measurement, mirror reflectivity measurement, and x-ray diffractometry. For mounting a device, the VECSEL epitaxial structure was thinned, metallized with Ti/Pt/Au layers, and cleaved into $800\,\mu\text{m} \times 800\,\mu\text{m}$ sized chips. These chips are mounted on a heatsink by soldering with $Au_{0.8}Sn_{0.2}$. As expected, these devices showed continuous wave (CW) laser activity and emitted laser radiation with very promising beam properties. The radial symmetric gaussian beam profile is shown in a 2-dimensional and 3-dimensional view in Fig. 3 for an output power of 9.2 mW.

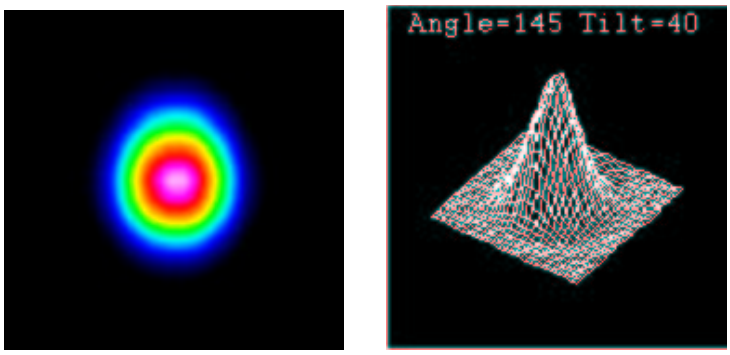

Fig. 3. VECSEL beam profile at an output power of $P_{\text{out}} = 9.2\,\text{mW}$

As a pump source, a standard 808 nm high-power laser diode is used with a suitable beam shaping optic. The diameter of the focussed spot is about 100 μm. By adjusting the external mirror modes of various orders can be forced including the fundamental TEM_{00} mode. In that case, the laser spectrum showed only one single peak at $\lambda = 984.7\,\text{nm}$ (see Fig. 4).

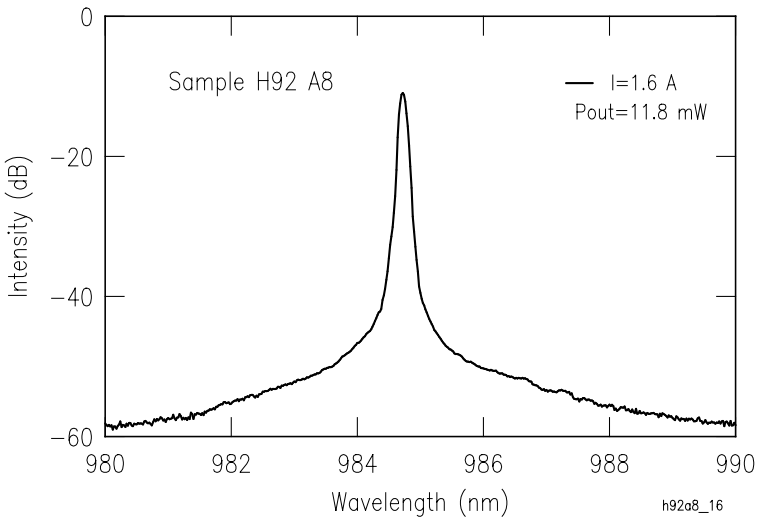

Fig. 4. VECSEL emission spectrum with a single peak at $\lambda = 984.7\,\text{nm}$ at an output power of $P_{\text{out}} = 11.8\,\text{mW}$

No side modes can be recognized here. For the measurement, a spectrometer resolution of 0.1 nm was used. With the very large cavity length in this setup the longitudinal mode distance is very small. Potentially existing multiple longitudinal modes can not be separated in the depicted spectrum with the spectrometer resolution. The width of the lasing spectrum (FWHM) has been determined to be about 0.15 nm limited by the spectrometer resolution. For this TEM_{00} mode, an output power of 11.8 mW CW has

been measured at a temperature of 16 °C. For some higher modes the resulting output power is significantly higher. The reason for this behavior is the non-ideal overlap between VECSEL laser-mode intensity profile and pump spot intensity profile. The output beam is slightly divergent. With a nominal external mirror reflectivity of 99.5 % the intra-cavity power can be estimated to 2.3 W.

Fig. 5 shows the VECSEL setup in operation. Only radiation of the emitting wavelength range is visible in this photograph, because the pump wavelength is filtered by an edge filter. A part of the pump optic, the VECSEL chip, the external resonator mirror and the laser mode can be recognized.

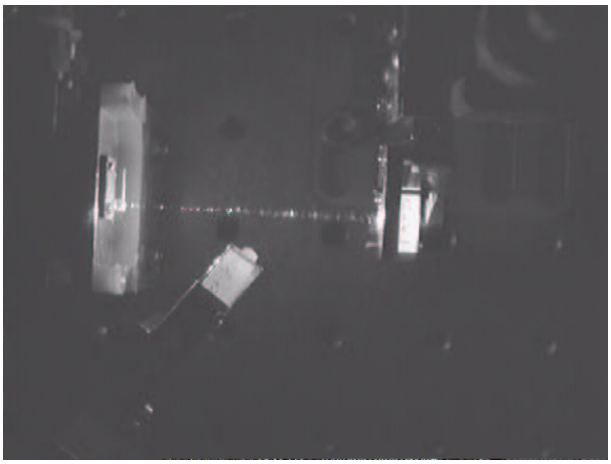

Fig. 5. Photograph of a VECSEL in operation. A part of the pump optic, the VECSEL chip, the external resonator mirror and the laser mode can be recognized.

4. Conclusion

An epitaxial VECSEL structure has been grown, mounted and characterized by photoluminescence measurement, mirror reflectivity measurement and x-ray diffractometry. Continuous wave laser activity has been achieved for the TEM_{00} mode. Depending on the external mirror adjustment, higher order modes have been observed. For the TEM_{00} mode, an output power of 11.8 mW has been measured. As a pump light source, a standard high power laser diode has been used.

References

[1] M. Sagawa, T. Toyonaka, K. Hiramoto, K. Shinoda, and K. Uomi, "High-Power Highly-Reliable Operation of 0.98-μm InGaAs-InGaP Strain-Compensated Single-

Quantum-Well Lasers with Tensile-Strained InGaAsP Barriers", *IEEE J. Selected Topics Quantum Electron., vol. 1, no. 2* , pp. 189–195, 1995.

[2] H. J. Unold, S. W. Z. Mahmoud, R. Jäger, M. Kicherer, M. C. Riedl, and K. J. Ebeling, "Improving Single-Mode VCSEL Performance by Introducing a Long Monolithic Cavity", *IEEE Photon. Technol. Lett., vol. 12, no. 8* , pp. 939–941, 2000.

[3] A. J. Fischer, K. D. Choquette, W. W. Chow, A. A. Allermann, and K. M. Geib, "5.2 mW Single-Mode Power from a Coupled-Resonator Vertical-Cavity Laser", *IEEE LEOS 2000 Lasers and Electro-Optics Society, 13th Annual Meeting, Rio Grande, Puerto Rico, ThN2* , pp. 802–803, 2000.

[4] M. Kuznetsov, F. Hakimi, R. Sprague, and A. Mooradian, "Design and Characteristics of High-Power (>0.5-W CW) Diode-Pumped Vertical-External-Cavity Surface-Emitting Semiconductor Lasers with Circular TEM_{00} Beams", *IEEE J. Selected Topics Quantum Electron., vol. 5, no. 3* , pp. 561–573, 1999.

[5] H. Q. Le, S. Di Cecca, and A. Mooradian, "Scalable high-power optically pumped GaAs laser", *Appl. Phys. Lett., vol. 58, no. 18* , pp. 1967–1969, 1991.

[6] M. Y. A. Raya, S. R. J. Brueck, M. Osinsky, C. F. Schaus, J. G. McInery, T. M. Brennan, and B. E. Hammons, "Resonant Periodic Gain Surface-Emitting Semiconductor Lasers", *IEEE J. Quantum Electron., vol. 25, no. 6* , pp. 1500–1512, 1989.

[7] S. W. Corzine, R. S. Geels, J. W. Scott, R.-H. Yan, and L. A. Coldren, "Design of Fabry-Perot Surface-Emitting Lasers with a Periodic Gain Structure", *IEEE J. Quantum Electron., vol. 25, no. 6* , pp. 1513–1524, 1989.

Destruction-Free Lifetime Characterization for Single-Mode Edge-Emitting Lasers

Ulrich Martin

Information about the lifetime of semiconductor lasers is an important issue in laser applications. The reliability of an optical data communication system requires a constant output power over a long time of operation at various conditions. Lifetime testing and aging of lasers during the manufacturing process ensure devices of high stability. But there is no warranty of stable operation under all conditions. On the other side, the integration of the lasers in optical, mechanical, and electrical systems makes it difficult to replace the device. So any information about the lifetime behavior of the emitters in a system would be helpful for optical data transmission. Using the data base of several lifetime tests and time-to-COMD measurements, it is possible to evaluate the destruction mechanisms in edge-emitting lasers and obtain information about the further device degradation.

1. Introduction

The major failure mechanisms of single mode edge emitting lasers are the slow optical output power degradation and the Catastrophic Optical Mirror Damage (COMD). Especially the effect of COMD which takes place at laser facet, can be reduced by a suitable protection of the facet [4] to reduce thermal and chemical effects [1]. Coatings on edge-emitting laser facets are necessary to establish a laser emission from only one facet of the device. Improper coatings can also initiate a failure during device lifetime. To characterize the protection performance, many lifetime tests at different conditions have to be done and differences in device characteristics during such a test should be found. To get basic information about the electrical and optical changes in a device, the fundamental effects of radiative and non-radiative emission have to be characterized. By doing small signal measurements of output power and voltage to current characteristics we obtain various information about internal and external destruction mechanisms. Comparing these results with the lifetime behavior of the devices allows the characterization of typical destruction mechanisms.

2. Measurement Principle

In order to get information about destruction mechanisms it is necessary to find changes in the electrical and optical behavior of the device. So, above laser threshold, the output

power of a single-mode edge-emitting laser is about a few mW. A slight reduction of output power can not be recognized. Because of the logarithmic voltage to current behavior of these devices, small reductions of input voltage because of serial contact resistors can have an effect on the current and so a reduction of the output power is observed. Especially the non-radiative current part inside a laser device can change the efficiency of the devices. These effects can be measured below laser threshold at low current densities. The basic principle of this measurement technique is a constant dependence of the output power versus voltage characteristic of each optoelectronic device in this operation area. This logarithmic plot is simply constant without an effect of non-radiative current variation and reduction of device efficiency. Changes in the voltage to current behavior provide information about the value of this non-radiative current. It gives also information about the surface recombination which is a part of the non-radiative current of a such a device [5]. Because of the bandgap reduction at the surface, this current is linked to the emission area at the surface of the semiconductor. Different measurements show that this surface current can still be measured at a voltage energy level below bandgap. This surface leakage current can also be measured in backward direction of the device. The voltage to current behavior of the surface current can be modeled by a resistor parallel to the laser device. A reduction of this resistor has main influence on degradation and the COMD-characteristic of the device. In this report, just the changes of current-versus-voltage characteristics during different device destruction mechanisms will be shown.

3. Characterization of Coating Problems

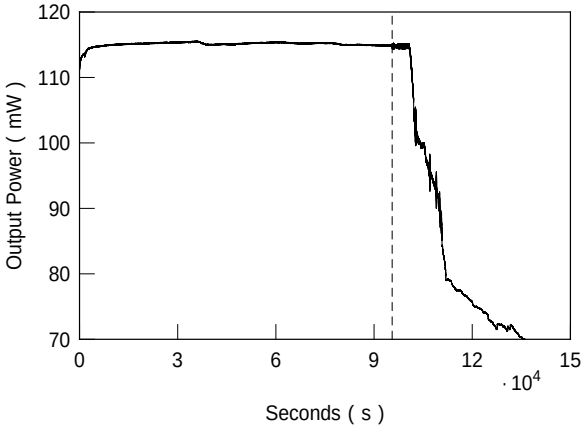

Fig. 1. Lifetime behavior of a laser destruct by a coating catastrophic mirror damage. The two areas mark the changes in current to voltage characteristics which can be seen in Fig. 2.

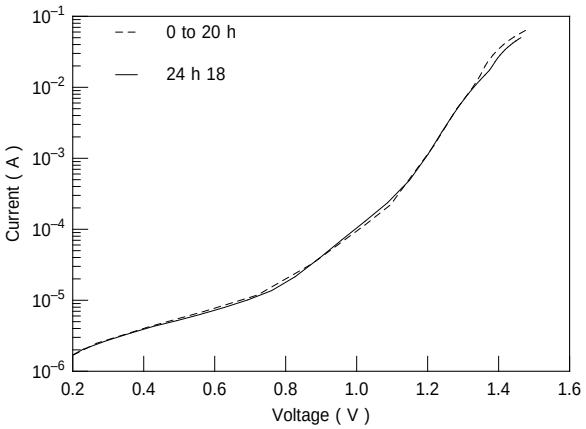

Fig. 2. Current versus voltage behavior during different lifetimes. The solid line show the measurement result at the dashed line in Fig. 1.

The first destruction effect which is presented is a thermal destruction of the high reflection coating itself. Because of impurities inside the coating the layers are heated up by

absorbing light. These heated layers provide chemical reactions between different coating materials and so more light absorbing areas are built up [3]. As illustrated in Fig. 2 before the coating damage takes place, the threshold of the laser, shown as a kink on the right hand side of the plot, is shifted to higher current and voltage values without any other change in the electrical characteristic. A similar reduction of reflectivity in the coating takes place and starts the destruction mechanism of the laser.

4. Characterization of COMD Effects

The device to show the changes in voltage to current characteristics of a catastrophic optical mirror damage is a simply cleaved single mode edge emitting laser without coated laser facet. The main destruction mechanism is built up by the COMD without influence of the chemical behavior of the coating materials. Light absorption at semiconductor surface is the main reason for the catastrophic optical mirror damage [2]. Oxidation effects and bandgap shrinkage at the facet increase the light absorption and speed up the destruction mechanism [6]. This increasing surface current can be noticed at low voltage operation were no radiative recombination effect consists. In Fig. 3 a typical change in the voltage to current plot during a COMD test can be recognized at voltages below about 1 V. This surface current can be modeled by a resistor parallel to the laser device. The value of this resistor changed from an very high value, which can't be measured with our measurement setup, to a value of about 120 kΩ before the catastrophic optical mirror damage occurs. After the destruction the value of this resistor is constant. The last measurement before COMD was taken just a few minutes before the device was destroyed. The value of this virtual resistor can also be measured in backward direction

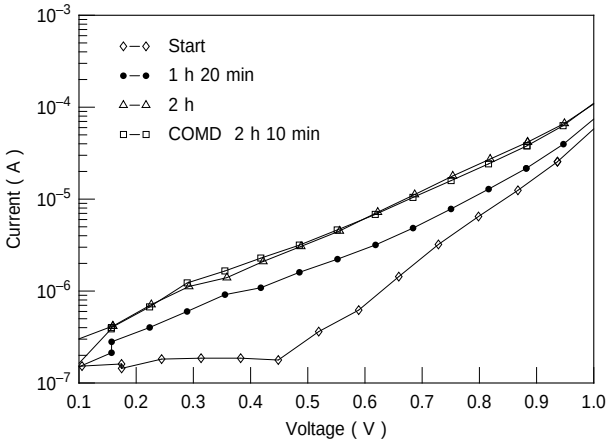

Fig. 3. Changes in voltage versus current behavior of a cleaved single mode laser below radiative emission during different lifetimes.

of the laser device. The high value of the resistor configures a very tricky measurement, only small current or voltage changes can destroy device totally. The voltage versus current dependence above 1 V is nearly constant and does not change during the lifetime

measurement. After the COMD destruction the threshold current is increased. The plot in Fig. 4 illustrates the shifting of the threshold kink from 1.31 V to 1.35 V after the COMD destruction. The threshold current is increased from 10 mA to 20 mA. The behavior of

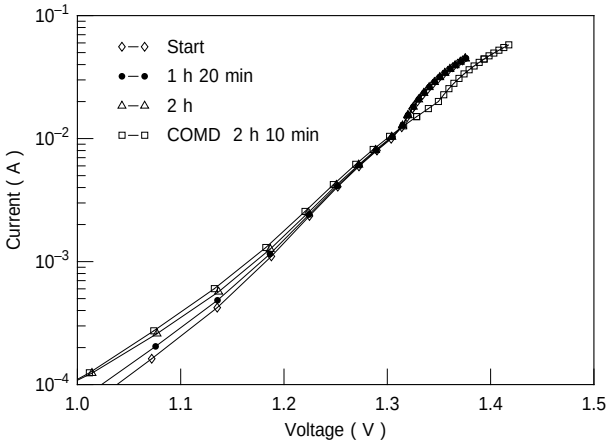

Fig. 4. Current to voltage plot above 1 V of the same laser as shown in Fig. 3. Changes only can be seen after COMD occurs. In this plot the threshold increased to 1.35 V and 20 mA.

COMD effects at coated devices is similar the same to this results, but the values and the shapes of the plots change in dependence of the coating structure.

A) Characterization of Degradation Effects

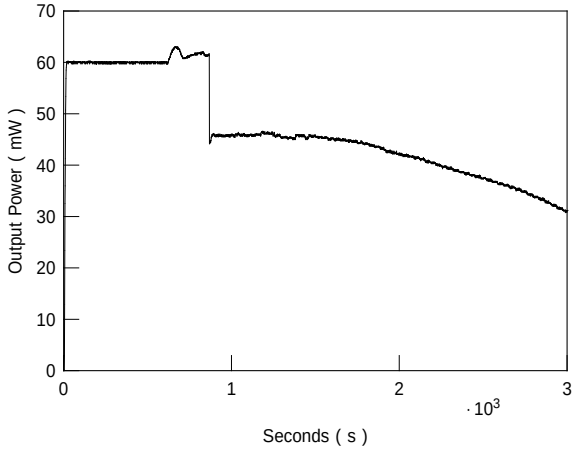

Fig. 5. Lifetime behaviour of an edge emitting laser diode.

The final destruction effect is the steady reduction of output power during operation. This effect is similar the general destruction procedure in laser devices. As Fig. 5 illustrates, the output power is reduced by degradation after COMD occurs. Comparing the voltage to current characteristics of a COMD destruction in Figs. 3 and 4 and the degradation

process (Fig. 6), the changing characteristics looks similar. In both mechanisms the surface resistor is reduced. But the behavior in the radiative operation (above 1 V) is different. At a COMD destruction there is nearly no change in this part of the plot during lifetime. At the degradation mechanism the slope of voltage versus current plot is reduced during

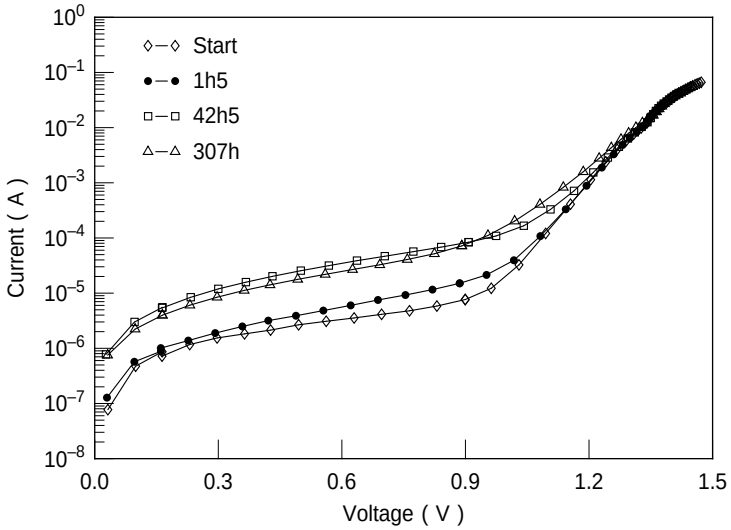

Fig. 6. Current to voltage behaviour of an edge emitting single mode laser with slowly degradation of output power.

lifetime in the operation area of radiative emission. As can be seen in Fig. 6 during degradation of a laser device the surface current increase and also an additional part of nonradiative current must be added to reach the same optical output power. The rate equations show that the nonradiative current determine laser threshold. So a slowly increasing of threshold current during a degradation process can also be determined by this figure. This effect decreases the efficiency of the device and the structure is heated up and the output power is reduced twice. The increasing nonradiative current in the radiative operation area can be described by an electrical and a thermal leakage current in the device which can be modeled by a reduced transverse conductivity inside the device. The resulting electrical model is shown in Fig. 7. The ideal laser diode in the middle of Fig. 7 is surrounded by nonradiative mechanisms whose values change during the aging procedure. So the changing current to voltage characteristic of a device can be calculated by changing the resistor values of this model.

5. Conclusion

By performing lifetime tests of single mode edge emitting lasers different changes in the voltage to current characteristic can be realized. The main destruction mechanisms of laser devices show a typical characteristic of the changes in the voltage to current plot below laser threshold. Especially the degradation process at long time operation can be

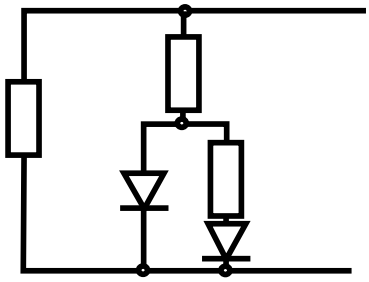

Fig. 7. Electrical model of a laser diode to simulate the results of the small signal measurement technique.

recognized by comparing this measurement results at different times and so information about the lifetime behaviour in future can be acquired.

References

[1] Tamanuki et al., "Ammonium Sulfide Passivation for AlGaAs/GaAs Buried Heterostructure Laser Fabrication Process", *Jap. J. Appl. Phys.,* vol. 30, no.3, Mar. 1991, pp. 499-500.

[2] M. Fukada, "Reliability of high power pump lasers for erbium-doped fiber amplifiers", *J. of High Speed Electronics and Systems,* vol. 7, no. 1, pp. 55-84.

[3] Fukushima et al., "Studies of facet passivation on visible laser diodes", *Jap. Society of Appl. Phys. and Rel. Societies,* vol. 3, pp. 1044.

[4] H.J. Rosen et al., "Chemical changes accompanying facet degradation of AlGaAs quantum well lasers", *J.Appl. Phys.,* vol. 72, no. 9, pp. 3884-3896.

[5] G. Erbert et al., "Non-Radiative current in InGaAs/AlGaAs Laser diodes as a measure of facet stability", *Solid-State Electronics,* vol. 42,no. 11, pp. 1939-1945, 1998.

[6] G. Chen, "Facet heating of quantum well lasers", *J. Appl. Phys.,* vol. 74, no. 4, 1993.

Fabrication and Characterization of High-Power High-Brightness Laser Diodes

Eckard Deichsel

High-power broad-area InGaAs/AlGaAs/GaAs single-quantum-well separate-confinement heterostructure (SQW-GRINSCH) lasers have been investigated. Optical output powers of 7.1 W have been measured with a maximum wall-plug efficiency of 59 %. For laser bars, values of up to 121 W have been achieved with an efficiency of 56 %. The properties of broad-area lasers having dry-etched mirror facets are almost identical to devices with cleaved facets. Record values for the CW output powers of 2.59 W per uncoated facet and wall-plug efficiencies of more than 55% have been obtained for devices with dry-etched laser facets. L-I curves and corrected far fields of lasers with improved unstable resonators are presented.

1. Introduction

Dry etching in laser fabrication offers a variety of advantages compared to the conventional fabrication process and enables many new applications. Accurate control of etching depths, lateral positions, and sidewall slopes of the etched structures are required for the ridge-waveguide laser fabrication which can be realized in a dry-etching process. Another advantage is the ability of full-wafer processing and testing that allows fabrication and characterization of lasers without separating the chips, leading to VLSI-type automation [1]. Therefore, the manipulation of the cleaved laser bars and chips, e.g. for the mirror coating, can be reduced to a minimum. New applications become possible like the monolithic integration of a monitor photodiode allowing to control the optical output power of the laser during operation. Finally, the orientation and shapes of the mirrors are no longer dependent on the crystal orientation. This enables new laser designs including unstable resonators [2, 3], curved mirrors [4], lasers with distributed Bragg reflectors [5], or semiconductor ring lasers [6]. In [7], many other advantages and applications are described like Fresnel lenses, 45° reflectors, microlenses, and waveguides.

On the other hand, there are strict requirements for the dry-etched facets. Vertical, flat, smooth, and damage-free laser mirrors are necessary for good device performance. Tilted facets or corrugation of mirror surfaces lead to increased threshold currents, reduced efficiencies, and far-field distortions. Additionally, the lifetime and maximum output power of the devices may be reduced due to chemical contamination of the facets caused by the dry-etching process. All these requirements must be considered in the development of an optimized etching process.

2. Epitaxy

The epitaxial layer sequence of the lasers is a MBE-grown graded-index separate-confinement heterostructure (GRINSCH). The active region consists of an 8 nm-thick compressively strained $In_{0.2}Ga_{0.8}As$ single quantum well which is surrounded by 10 nm-thick GaAs spacing layers followed by doped AlGaAs grading and cladding layers. The p- and n-dopants are C and Si, respectively. The emission wavelength of the laser devices is 980 nm. Details of the epitaxial growth process and the optimization of the epitaxy for high-brightness applications are described in [8] and [9].

3. High-Power Broad-Area Lasers and Laser Bars

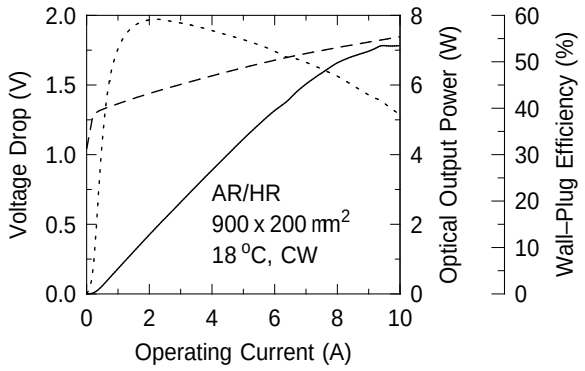

Fig. 1. Output characteristics of an AR/HR-coated 900 μm × 200 μm laser diode. Plotted are the *L-I* (solid line) and the *V-I* (dashed line) characteristics together with the wall-plug efficiency (dotted line).

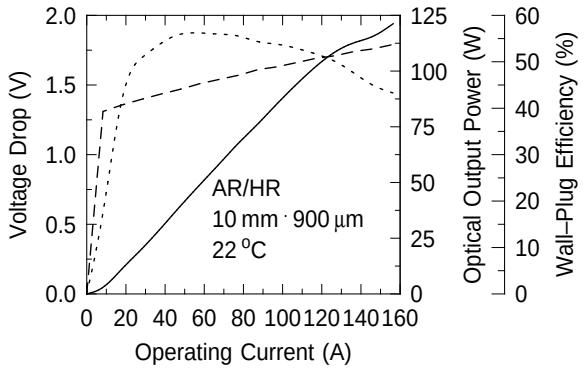

Fig. 2. Output characteristics of an AR/HR-coated 10 mm × 900 μm laser bar. Plotted are the *L-I* (solid line) and the *V-I* (dashed line) characteristics together with the wall-plug efficiency (dotted line).

Broad-area lasers have been fabricated in a standard process from this optimized epitaxial material. The AR/HR-coated 900 μm × 200 μm devices have been mounted junction-side down on diamond heat spreaders and measured using a calibrated integrating sphere photodetector. The device characteristics is shown in Fig. 1. A differential slope efficiency of 77 % has been obtained in the *L-I* curve with a threshold current density as low as 140 Acm^{-2}. The maximum optical power of 7.1 W is limited by thermal roll over. From these data a maximum wall-plug efficiency of 59 % has been derived. No facet damage has been observed even after extensive measurements. Other devices from the same epitaxial material exhibit nearly identical characteristics proving the reproducibility of epitaxy and fabrication process. A 10 mm laser bar with 25 single emitters (900 μm × 200 μm) has been mounted and measured at the Fraunhofer Institute (ILT), Aachen, Germany. The results are shown in Fig. 2. A maximum cw optical output power of 121 W has been achieved at 22 °C with a maximum wall-plug efficiency of 56 %.

These outstanding results exhibit the good quality of the epitaxial material, which seems to be very promising for high-power and high-brightness applications.

4. Lasers with Dry-Etched Laser Mirror Facets

A) Fabrication

The gain-guided area is defined by wet-chemical etching. A SiO_2 passivation layer is deposited by plasma-enhanced chemical vapor deposition (PECVD). The p-contact window openings are defined using a CF_4 reactive ion etching (RIE) process followed by the p-contact Ti/Pt/Au metallization. These first steps are similar to the conventional fabrication of lasers.

The dry-etched mirrors require vertical, flat, and smooth facets, which can be achieved by using an optimized chemical-assisted ion-beam-etching process (CAIBE) and a 3-level resist as can be seen in Fig. 3. AFM measurements show remaining roughnesses of 3–5 nm (RMS). Details of the fabrication process and characterization are described in [10]. At this state of the process, first pulsed on-wafer tests can be performed and mirror coatings can be applied. Then, a thick gold layer is electroplated onto the p-contact metal to reduce thermal and electrical resistance of the devices.

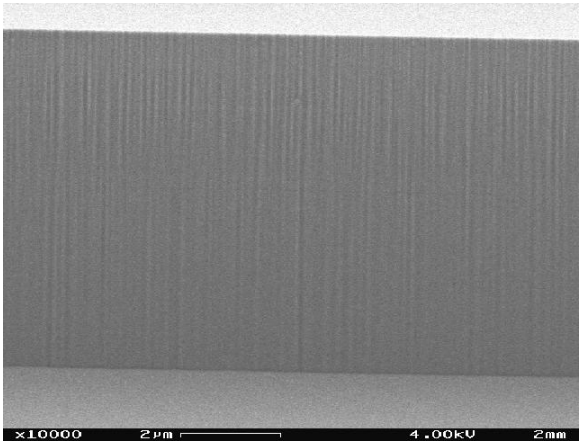

Fig. 3. SEM micrograph of a vertical 8-μm-deep dry-etched mirror facet. The process has been performed at a substrate temperature of 75 °C, an ion energy of 400 eV, and a chlorine gas flow of 4 sccm.

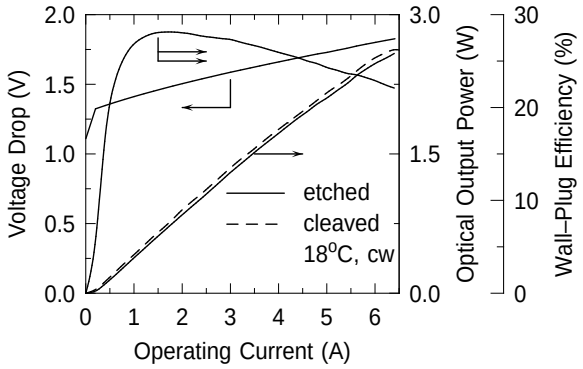

Fig. 4. Optical front-facet output power, voltage drop, and wall-plug efficiency of a 1000 μm × 100 μm broad-area laser with dry-etched facets (solid lines). For comparison, the output power characteristic of a laser with cleaved facets is plotted (dashed line).

B) High Output Power of Dry-Etched Laser Facets

For high-power operation, 1000 μm × 100 μm lasers fabricated with the above described process have been mounted junction-side down on diamond submounts and characterized in CW operation at room temperature. As presented in Fig. 4, an optical output power of 2.59 W from the front facet of the laser has been measured with a calibrated integrating-sphere detector. To our knowledge, this value represents the highest cw optical-output

power from a dry-etched laser facet. Additionally, it should be emphasized that no protective facet coating has been deposited onto the laser mirrors. The threshold current density and the differential quantum efficiency are $j_{th} = 100\,\mathrm{Acm}^{-2}$ and $\eta_\mathrm{d} = 34.1\,\%$ per facet, respectively. The same optical output power is emitted at the back facet of the laser. The corresponding wall-plug efficiency for both facets is over 55 % in the range between 1 and 3 A. Lasers with cleaved facets and identical geometry have been fabricated from the same epitaxial wafer material. For comparison, the output power characteristic of a laser of this type is plotted in Fig. 4 as a dashed line. No significant differences can be noticed when comparing lasers with cleaved and dry-etched facets under these conditions.

C) Unstable Resonators

Different types of unstable resonators with curved mirrors have been fabricated. Fig. 5 shows the *L-I* curves of $500\,\mu\mathrm{m} \times 100\,\mu\mathrm{m}$ symmetric unstable resonators with different mirror curvatures. The curvature radii are 250, 500, 1000 and $2000\,\mu\mathrm{m}$ and the corresponding magnifications are 17, 7, 3.5 and 2.125, respectively. For comparison a broad area laser with same dimensions and two cleaved mirrors is also shown.

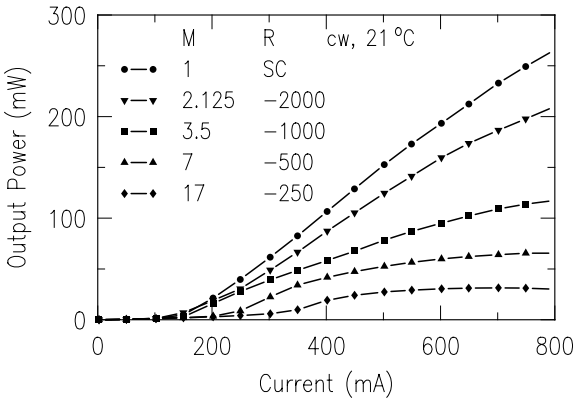

Fig. 5. *L-I* curves of $500\,\mu\mathrm{m} \times 100\,\mu\mathrm{m}$ unstable resonators with curved mirrors on both sides. The mirror curvatures are 250, 500, 1000 and $2000\,\mu\mathrm{m}$. For comparison a laser with two cleaved ends is also shown.

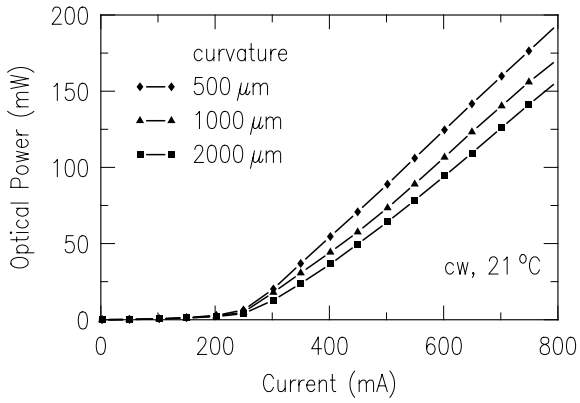

Fig. 6. *L-I* curves of devices with tapered waveguides, the narrow end facing to the dry-etched curved mirror and the $200\,\mu\mathrm{m}$-wide cleaved end on the other side. The curvatures of the mirrors are 500, 1000, and $2000\,\mu\mathrm{m}$.

With increasing magnification the loss of the unstable resonators also increases, leading to a very poor behavior of the $250\,\mu\mathrm{m}$ curvature devices. However these losses can be compensated by an optimized laser design, which matches the electically-pumped regions to the light-guiding regions.

D) Tapered Unstable Resonators

Devices with tapered waveguides have been fabricated and investigated. The dry-etched curved mirror is located on the narrow end of the tapered region, on the opposite side of

the 200 μm-wide cleaved output mirror. Compared to the broad-area unstable resonators in Fig. 5 the optical-output power of the tapered unstable resonators in Fig. 6 increases for higher mirror curvatures. This is a very good possibility to compensate the higher losses with increasing magnification.

The corrected far fields were also measured, which is shown in Fig. 7 for the 500 μm-curvature device with tapered waveguide. The far fields for the other lasers with different mirror curvatures are comparable. Currents below threshold lead to wide corrected far field, due to spontaneous emission. With increasing current the corrected far field narrows and raises for higher currents again.

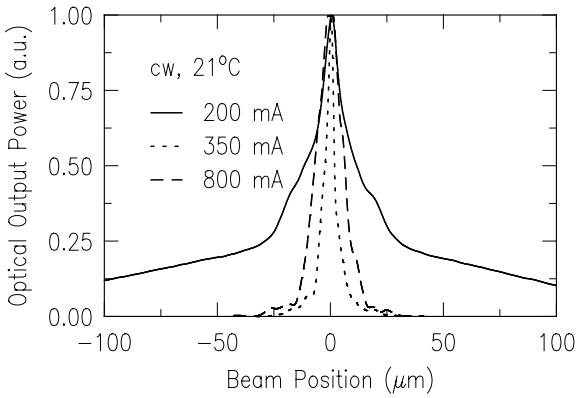

Fig. 7. Corrected far-field of the 500 μm-curvature device with tapered waveguide.

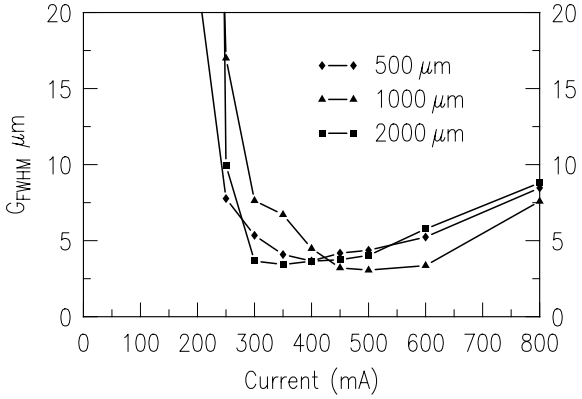

Fig. 8. Virtual source width of devices with tapered waveguides. The curvature radii of the mirrors are 500, 1000, and 2000 μm.

The virtual source width has been calculated from the data of the corrected far fields. Fig. 8 shows the virtual source width of the devices with tapered waveguides and 500, 1000, and 2000 μm mirror curvatures. The minimum virtual source widths are between 3 and 5 μm. The smallest virtual source size with 2.0 μm was found for a shorter device with 250 μm mirror curvature at 550 mA.

5. Conclusion

Epitaxial material for high power applications has been shown. Single lasers and laser bars were presented with optical output powers of 7.1 W and 121 W, respectively. The wall-plug efficiency was up to 59 %. This epitaxial material seems to be very promising for the fabrication of semiconductor unstable-resonator lasers. First lasers with straight dry-etched output facets showed 2.59 W per single uncoated facet in cw operation. Improved unstable resonators with tapered geometry were presented with good *L-I* behavior and virtual source sizes smaller than 5 μm.

References

[1] P. Vettiger, M. K. Benedict, G.-L. Bona, P. Buchmann, E. C. Cahoon, K. Dätwyler, H.-P. Dietrich, A. Moser, H. K. Seitz, O. Voegeli, D. J. Webb, and P. Wolf, "Full-wafer technology — A new approach to large-scale laser fabrication and integration", *IEEE J. Quantum Electron.*, vol. 27, no. 6, pp. 1319–1331, 1991.

[2] S. A. Biellak, C. G. Fanning, Y. Sun, S. S. Wong, and A. E. Siegman, "Reactive-ion-etched diffraction-limited unstable resonator semiconductor lasers", *IEEE J. Quantum Electron.*, vol. 33, no. 2, pp. 219–230, 1997.

[3] M. L. Tilton, G. C. Dente, A. H. Paxton, J. Cser, R. K. DeFreez, C. E. Moeller, and D. Depatie, "High power, nearly diffraction-limited output from a semiconductor laser with unstable resonator", *IEEE J. Quantum Electron.*, vol. 27, no. 9, pp. 2098–2108, 1991.

[4] P. Unger, V. Boegli, P. Buchmann, and R. Germann, "Fabrication of curved mirrors for visible semiconductor lasers using electron beam lithography and chemically assisted ion-beam etching", *J. Vac. Sci. Technol. B*, vol. 11, no. 6, pp. 2514–2518, 1993.

[5] E. Höfling, F. Schafer, J. P. Reithmaier, and A. Forchel, "Edge-emitting GaInAs-AlGaAs microlasers", *IEEE Photon. Technol. Lett.*, vol. 11, no. 8, pp. 943–945, 1999.

[6] Z. J. Fang, G. M. Smith, D. V. Forbes, and J. J. Colemann, "An InGaAs-GaAs strained layer single quantum-well ring laser with a reactive ion-etched tetragonal cavity", *IEEE J. Quantum Electron.*, vol. 31, no. 1, pp. 44–48, 1995.

[7] P. P. Deimel, "Micromachining processes and structures in micro-optics and optoelectronics", *J. Micromech. Microeng.*, vol. 1, pp. 199–222, 1991.

[8] R. Jäger, J. Heerlein, E. Deichsel, and P. Unger, "63% wallplug efficiency MBE grown InGaAs/AlGaAs broad-area laser diodes and arrays with carbon p-type doping using CBr_4", *J. Crystal Growth*, vol. 201/202, pp. 882–885, 1999.

[9] E. Deichsel, F. Demaria, and R. Jäger, "Optimized epitaxial structure of laser diodes for high-power and high-brightness applications", *Annual Report, Department of Optoelectronics, Universisty of Ulm*, pp. 27–30, 1999.

[10] E. Deichsel, F. Eberhard, R. Jäger, and P. Unger, "High-power laser diodes with dry-etched mirror facets and integrated monitor photodiodes", accepted for *J. Selected Topics Quantum Electron.*, vol. 7, no. 3, May/June 2001.

Optical Characterization of High-Power 940 nm InGaAs/AlGaAs Semiconductor Laser Amplifiers with Tapered Gain Region

Frank Demaria and Manfred Mundbrod

The optical intensity distribution at the output facet as well as the lateral beam quality factor M^2 of optical amplifiers are presented. The devices are part of a hybrid master-oscillator power-amplifier setup. At 1.1 to 1.7 W output powers we measured M^2 values between 1.6 and 2.9. The diffraction angle of the optical beam within the device depends on the beam quality of the master oscillator and is also affected within a certain range by the optical setup of the optical path at the input side of the amplifier chip.

1. Introduction

Semiconductor amplifiers with tapered gain region in a master-oscillator power-amplifier (MOPA) setup are well suited for applications requiring high optical output powers with good spatial beam quality and narrow line width. One possible application is the generation of high-power blue laser light by second harmonic generation [1]. For achieving a good performance, the lateral design of the devices as well as the epitaxial structure play an important role. One major problem concerning optical amplifiers with flared gain regions is the overlap optimization of the optical beam propagation inside the device with the pumped region. If the light divergence angle is small compared to the taper angle, the injected carriers in the outer gain region do not contribute to stimulated emission, but rather emit spontaneously or recombine non-radiative. As a consequence, the beam quality and conversion efficiency decrease, whereas noise and heating increase. If, on the other hand, the propagating beam expands faster than the gain region, the outer part of the gauss-shaped radiation is absorbed, whereas the inner part is amplified. This leads to a reshaping of the beam that results in a top-hat intensity distribution which in turn has a loss in beam quality as a consequence.

The amplifiers that have been fabricated consist of a simple gain guided taper region, where the radiation can expand laterally according to free space approximation over the whole length. One advantage of such a design without index guided preamplifier structure is that the diffraction angle of the beam within the device can be widely adjusted by the selection and positioning of the collimating and focusing lenses in the input optical path. In the next section, measurements that have been performed at amplifiers with a suchlike optimized coupling are presented.

2. Output Characteristics, Beam Quality and Lateral Near-Field

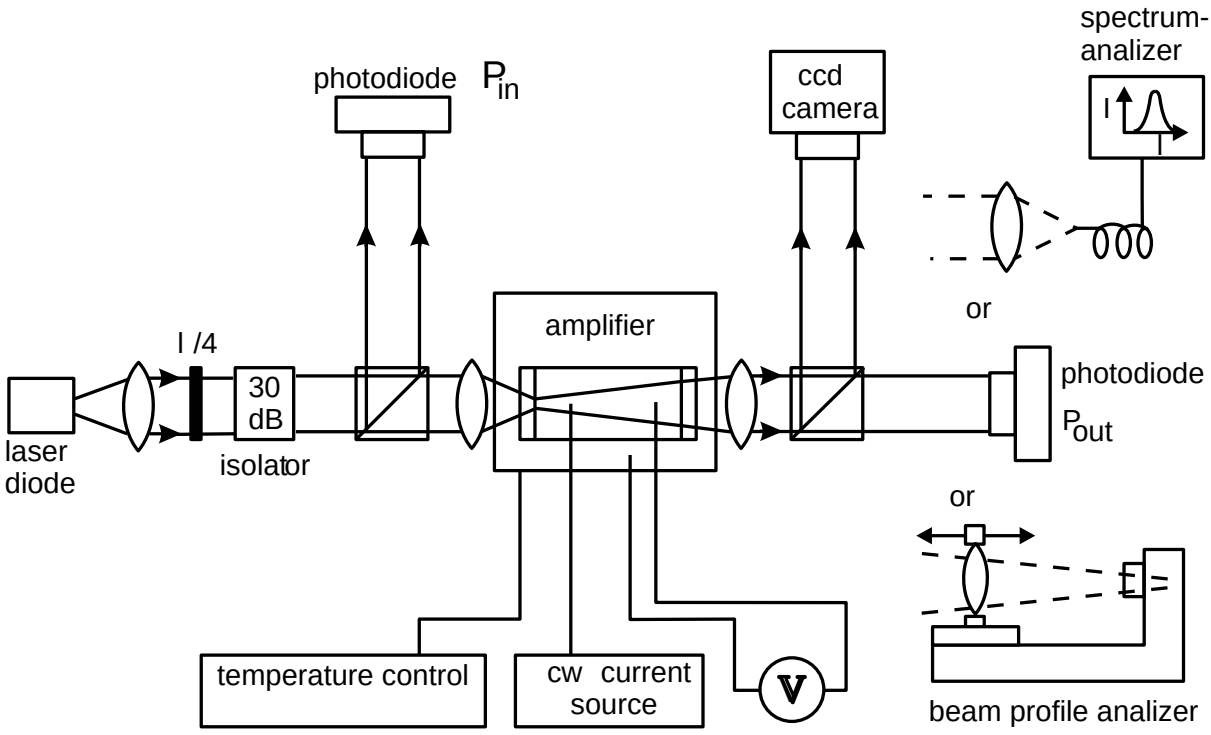

Fig. 1. Measurement setup.

Fig. 1 shows the schematic diagram of the measurement setup for the characterization of the amplifiers. The results have been achieved with a 2-mm-long 8°-full-taper-angle amplifier. The optical output characteristics of that device is depicted in Fig. 2. In order to reduce thermal stress, the maximum current has been restricted to smaller values at small and medium optical input powers. The non-radiative recombination processes cause thermal energy dissipation particularly if the carrier injection is high and the photon injection is low. As a result the output power is stagnating at smaller currents for lower optical input powers, caused by thermal rollover.

As a master oscillator we used a ridge-waveguide laser diode emitting at 940 nm. Because of optical power losses, mainly caused by the optical isolator, a near diffraction limited input beam with an M^2 value of 1.1 has only been obtained up to 6.5 mW. With higher powers, the input sided M^2 significantly increases up to 1.7 at 11 mW. Figs. 3 and 4 show the results of a lateral beam quality measurement series. The M^2 values have been determined by measuring the propagation of a focused beam in the waist region. Besides different optical input powers, the current of the amplifier has been varied within a range from 2.5–3.5 A. Hence the variation of the M^2-values in Fig. 4 at fixed input powers is mainly caused by the different currents. Together with the beam quality, the optical intensity distribution at the output facet in the lateral direction, called the optical near-field, has been determined. Two examples are presented in Fig. 5 and 6. The determination

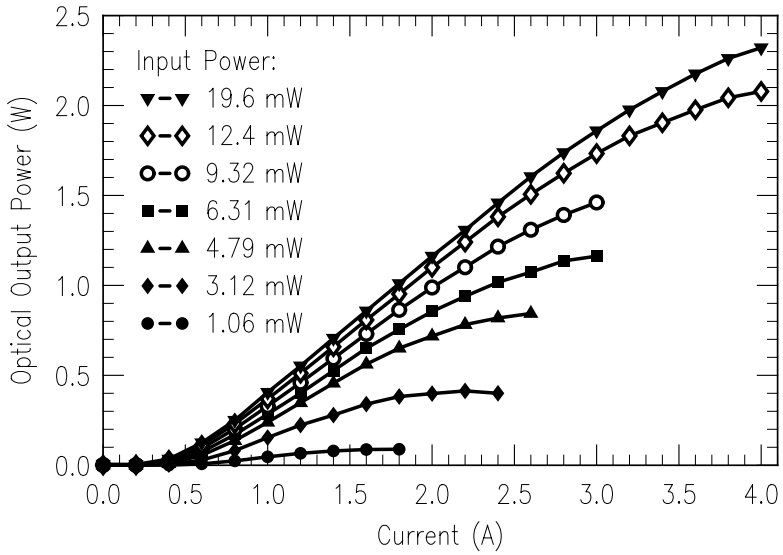

Fig. 2. Optical output characteristics of a tapered amplifier with 8° full taper angle and a length of 2 mm.

has been done by measuring the lateral power distribution by scanning the image of the facet with a slit and taking the shape of the vertical mode into account [3].

It is well known from Gaussian beam propagation theory [4] that the far-field divergence angle is increasing simultaneously with the beam quality factor M^2. Fig. 7 shows the calculated quasi free space beam propagation for two different M^2 values and the pumped region of an amplifier with 8° full taper angle.

At an optical input power of 6.6 mW, the near diffraction limited beam is mainly guided within the taper region and quite homogeneously amplified over its hole width. Fig. 5 shows that the shape of the output optical near field is Gaussian like with filamentations in the region near the optical axis. At a higher optical input power, the beam spreading within the amplifier and also the width at the input facet is enhanced because of the reduced input beam quality. As a result, the shape of the near field at the output facet is kind of a top hat, superimposed by considerable filamentation as shown in Fig. 6.

The other extreme, where the beam spreading inside the device is small compared to the broadening of the current injection region is diagramed in Fig. 9. Both, Fig. 8 and 9, have been measured with a 10° taper angled device. In order to achieve a smaller divergence angle, the depth of focus has been increased. For this purpose, the focusing lens with 6.5 mm focal length that has been used for the measurements, diagrammed in Fig. 3 to 6 and Fig. 8, has been substituted by one with 8 mm focal length. The enhanced depth of focus goes ahead with a broader focal beam width as well in the vertical as in the horizontal direction. The vertical broadening results in a lower coupling efficiency which explains that not only the output power, but also the maximum intensity, is smaller in Fig. 9. In the outer region of the facet, only Amplified Spontaneous Emission (ASE) at

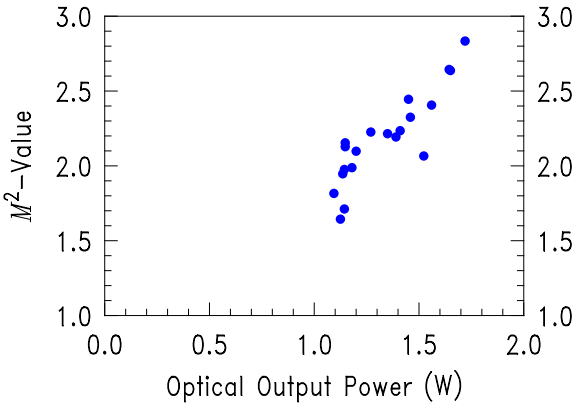

Fig. 3. Series of measurements with different output powers, and the corresponding beam quality factor.

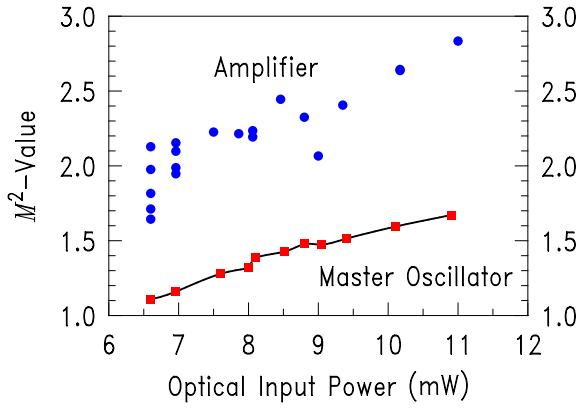

Fig. 4. Input sided and output sided beam quality factor at various input powers. The graph refers to the same series of measurements as Fig. 3

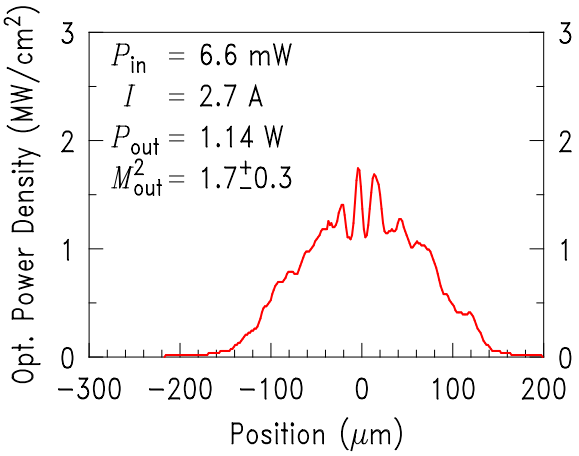

Fig. 5. Lateral intensity distribution at the output facet of an amplifier with 8° full taper angle at moderate input and output power.

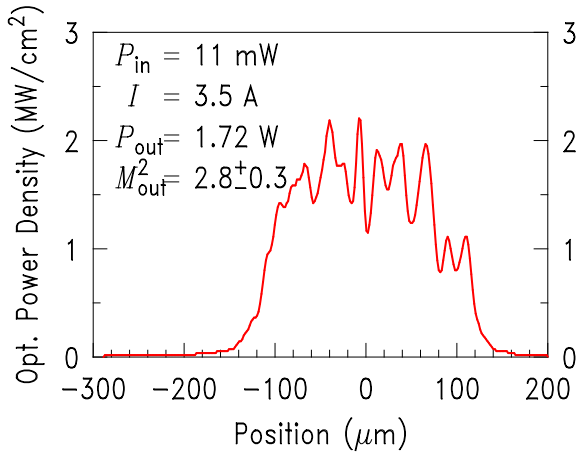

Fig. 6. Intensity distribution of the same device, with higher input and output power.

a quite constant intensity can be observed. Caused by the strong ASE radiation, the beam quality decreases in a way that it can not be measured anymore with our setup, which is evidence that the M^2 value is higher than 10. In Fig. 8, the broader taper angle has been widely compensated by slightly varying the axial position of the master oscillators collimating lens and the focusing lens. Though the shape of the output near-field is Gaussian like, comparable to that in Fig. 5, the beam quality factor of 2.6 is worse compared to a value of 1.7. This also can be explained by the enhanced ASE radiation.

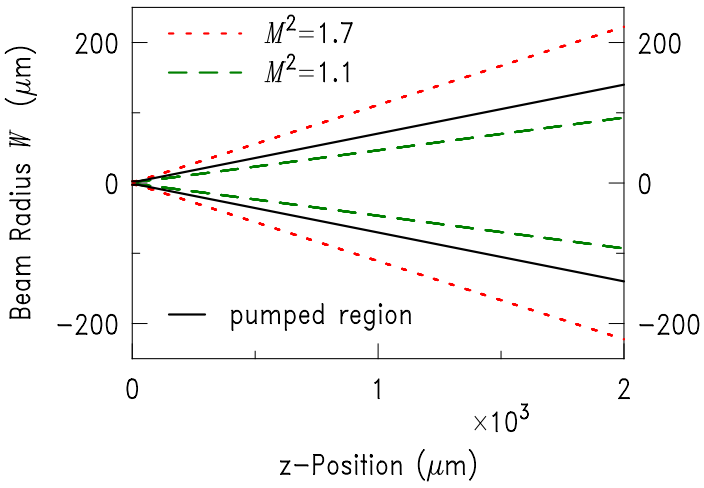

Fig. 7. Calculated beam expansion for different M^2-values in a tapered amplifier with 8° full taper angle and a length of 2 mm.

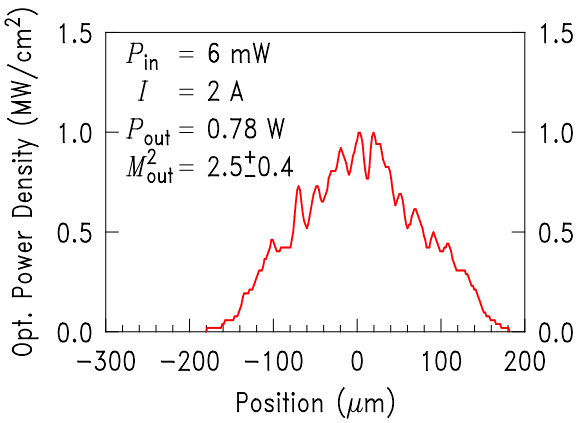

Fig. 8. Intensity distribution at the output facet of an amplifier with 10° full taper angle and input sided focusing lens with 6.5 mm focal length.

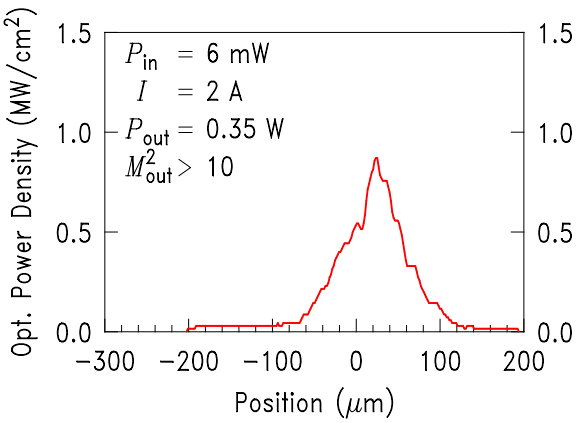

Fig. 9. Intensity distribution of the same device, but with 8 mm focal length of input sided lens.

3. Conclusion

Considerable beam qualities of tapered semiconductor amplifiers at high optical output powers have been measured. The measurements are also a indication for future design approaches, which should provide better beam qualities and higher powers. In order to achieve higher powers, the thermal rollover should be reduced. This can be done either by improved heat transmission or by increasing the efficiency of the device. Latter can be achieved by further improving the epitaxial design, which is demanding because structures with higher efficiencies showed tendency towards stronger filamentations [3]. On the other hand, the efficiency can also be improved by feeding the amplifier with higher input powers. This should also be an advantage with regard to the suppression of ASE and the resulting improvement of the beam quality, presumed that the input beam quality is not suffering at the same time. One strategy for that consists of a design that

implies an index guided preamplifier structure. The presented near field measurements reveal how those of such a structure should look like, where the beam propagation inside the gain guided region is optimized with respect to the output beam quality.

References

[1] D. Woll, B. Beier, K.-J. Boller, and R. Wallenstein, "1 W blue 465-nm radiation generated by frequency doubling of a high-power diode laser in critically phase-matched LiB_3O_5", *Optics Lett.*, vol. 24, no.10, pp. 691–693, 1999.

[2] G. Jost, "Hochleistungs-Laserverstärker auf der Basis von InGaAs-AlGaAs-GaAs", *Shaker Verlag Aachen*, 2000

[3] F. Demaria, E. Deichsel, and R. Jäger, "High-power semiconductor laser amplifiers with optimized active material", *Annual Report 1999, Dept. of Optoelectronics, University of Ulm*, pp. 44–47.

[4] A. Siegman, "Lasers", *University Science Books, Mill Valley, California*, 1986.

Influence of Growth Parameters on Crack Density in Thick Epitaxially Lateral Overgrown GaN Layers by Hydride Vapor Phase Epitaxy

Matthias Seyboth and Michael Wang

Using hydride vapor phase epitaxy (HVPE) the influence of growth parameters on crack density is studied for thick epitaxially lateral overgrown (ELOG) GaN layers. Reactor pressure, growth rate, and substrate temperature are key factors to obtain crack-free thick GaN layers. The cracking mechanism is discussed and void formation on top of the SiO_2 stripes is proposed to play a key role in stress relaxation and crack suppression.

1. Introduction

Due to the lack of a native nitride substrate, GaN-based compounds are commonly grown on sapphire [1] or 6H-SiC [2]. However, high dislocation- and defect-densities are generated in the epitaxial layers due to differences in lattice parameters and thermal expansion coefficients between layer and substrate. Despite continuous progress, many high-end applications of group III-nitrides are still limited by mismatched heteroepitaxial growth. Thus, the most favorable approach would employ GaN homoepitaxial growth [3] which proved already that it can provide unchallenged benchmarks in GaN material quality. GaN substrates, as compared to the mostly used sapphire substrates, have further advantages such as higher thermal conductivity, electrical conductivity for vertical carrier transport, simplified epitaxy without the need for nucleation layers, high index of refraction yielding an improved far field, and feasibility of easy cleavage for laser facets. However, bulk GaN substrates so far show limitations in size, availability, and costs due to the sophisticated high temperature and high pressure processes [5]. On the other hand, hydride vapor phase epitaxy is a promising approach to achieve freestanding GaN substrates [6]. By applying reduced pressure HVPE, high quality GaN layers with thicknesses of 10–20 μm have been obtained [7]. However, cracks became the main residual problem to achieve thicker layers and eventually freestanding GaN substrates. ELOG could be an effective way to relax the strain, reduce the threading dislocations and obtain crack-free thick GaN layers [8]. In this work, we report on the influence of growth parameters on crack density in thick layers using ELOG in HVPE.

2. Experimental

Growth is performed using a horizontal AIXTRON HVPE reactor. The Ga source is GaCl formed by the reaction between liquid Ga and HCl gas at 850 °C. The resulting GaCl is injected to the growth zone through a showerhead, where GaCl and NH_3 are mixed and react on the substrate surface. 1.5 μm thick GaN templates grown on c-plane sapphire by MOVPE serve as substrates for the present study. SiO_2 layers are deposited using plasma enhanced chemical vapor deposition. Along the GaN $\langle 1100 \rangle$ direction 10 μm wide stripes were structured at a period of 20 μm using standard photolithography and dry etching. Subsequently, GaN layers with thickness d of 40–70 μm were grown by HVPE under reactor pressures p of 250 and 550 mbar. At a constant V/III-ratio the growth rate r is varied from 15 μm/h to 70 μm/h by changing the GaCl supply rate. The substrate temperature T_G is varied from 1000 °C to 1100 °C. Beside standard characterization, the samples have been investigated regarding their crack density and void formation by optical and scanning electron microscopy (SEM).

3. Results and Discussion

Fig 1. shows optical micrographs of ELOG GaN layers grown at temperatures of 1000 °C, 1050 °C and 1100 °C ($p = 550$ mbar, $r = 70$ μm/h). The visible narrow dark lines are cracks within the layer, whereas the horizontal extended gray stripes correspond to the SiO_2 stripes beneath the surface.

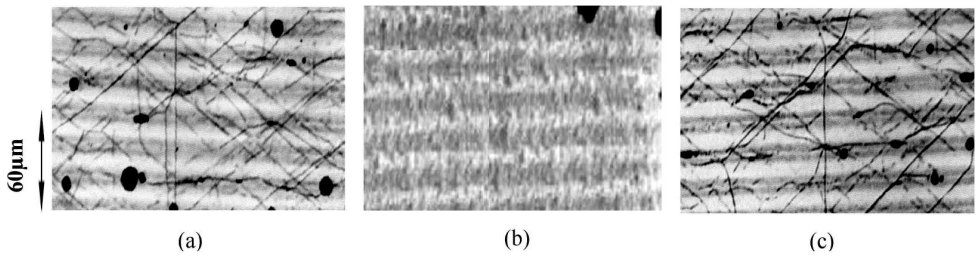

Fig. 1. Surface morphologies of samples grown at 1000 °C, 1050 °C, and 1100 °C.

The layers grown at 1000 °C and 1100 °C reveal crack densities of $4\times10^5\,\mathrm{cm}^{-2}$ and $3\times10^5\,\mathrm{cm}^{-2}$, while the layers grown at 1050°C have crack densities below $1\times10^2\,\mathrm{cm}^{-2}$. The influence of the reactor pressure on crack density is depicted in Fig. 2.

Increasing the growth pressure from 250 mbar to 550 mbar ($p = 1050$ °C, $r = 70$ μm/h) significantly reduces the crack densities from $5\times10^5\,\mathrm{cm}^{-2}$ to less than $1\times10^2\,\mathrm{cm}^{-2}$. The crack density is also strongly affected by the growth rate (see Fig. 3).

Whereas at growth rates of 15 and 30 μm/h, crack densities of $1\times10^6\,\mathrm{cm}^{-2}$ and $4\times10^4\,\mathrm{cm}^{-2}$ are present, crack densities less than $1\times10^2\,\mathrm{cm}^{-2}$ are achieved at higher growth rates of 70 μm/h ($T = 1050$ °C, $p = 550$ mbar). To investigate the mechanisms behind the influence of growth parameters on crack formation, SEM is used to investigate cross sections of the

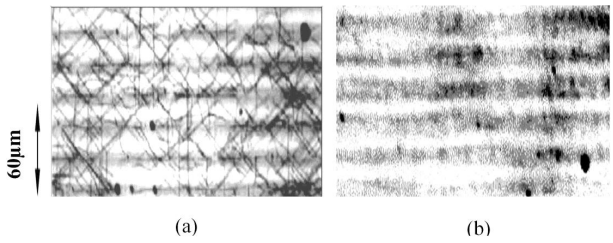

Fig. 2. Surface morphologies of samples grown at 250 mbar and 550 mbar.

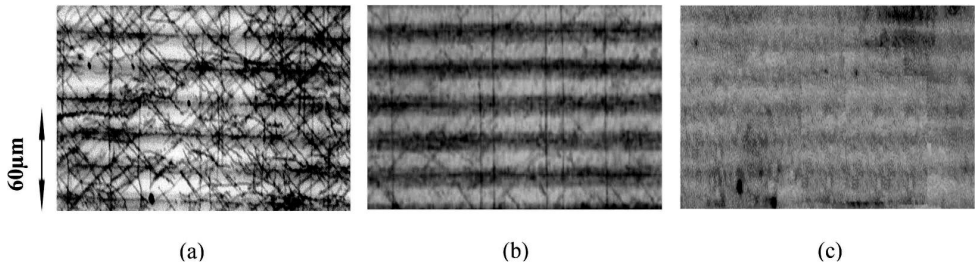

Fig. 3. Surface morphologies of samples grown at 15 μm/h, 30 μm/h, and 70 μm/h.

GaN layers depicted in Fig. 1(a), Fig. 3(b) and Fig. 1(b). The growth conditions of the samples yielded crack densities of $4\times10^5\,\mathrm{cm}^{-2}$, $4\times10^4\,\mathrm{cm}^{-2}$ and less than $1\times10^2\,\mathrm{cm}^{-2}$. We find a clear correlation between crack density and the size of the void on top of the SiO_2 mask. The ELOG layer without any visible void, grown at $T_G = 1000\,^\circ\mathrm{C}$, $p = 550$ mbar and $r = 70\,\mu$m/h, see Fig. 4(a), reveals the highest crack density at $4\times10^5\,\mathrm{cm}^{-2}$.

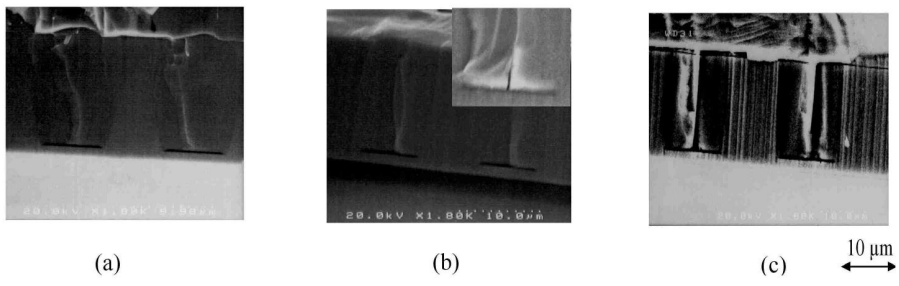

Fig. 4. SEM cross section micrographs of the GaN layers depicted in Fig. 1(a), 3(b), and 1(b). The crack density $4\times10^5\,\mathrm{cm}^{-2}$, $4\times10^4\,\mathrm{cm}^{-2}$ and less than $1\times10^2\,\mathrm{cm}^{-2}$ corresponds to the observed size of the void above the SiO_2 mask which is increasing from left to right. The insert in the upper left corner of Fig. 4(b) is a two times magnification of the SiO_2 mask region.

The GaN layer grown under conditions ($T = 1050\,^\circ\mathrm{C}$, $p = 550$ mbar, and $r = 30\,\mu$m/h) producing small voids reveals an one order of magnitude reduced crack density (see Fig. 4(b)). Under growth conditions ($T = 1050\,^\circ\mathrm{C}$, $p = 550$ mbar, and $r = 70\,\mu$m/h) where the lowest crack densities ($<1\times10^2\,\mathrm{cm}^{-2}$) are obtained the biggest void is found in cross-section SEM (see Fig. 4(c)).

We propose that these voids act as stress relaxation centers yielding 3–4 orders of mag-

nitude reduction in crack density. This is in agreement with finite element analyses [9] performed by Zheleva et al. who calculated the stress distribution in ELOG-GaN depending on the thermal expansion coefficient mismatch, and found that ELOG without SiO_2 can significantly reduce the stress as compared with conventional ELOG assuming no voids.

4. Summary and Conclusion

The influence of growth parameters, i.e. temperature, pressure and growth rate, on the crack density of ELOG GaN layer has been investigated. Crack free GaN layers with thickness of about 70 μm have been obtained. We have found a correlation between crack density and void formation, and we propose that the formation of voids is a key for stress relaxation and suppression of crack formation.

References

[1] S. Nakamura and G. Fasol, "The Blue Laser Diode", Springer Berlin, 1997.

[2] J.A. Smart, A.T. Schremer, N.G. Weimann, O. Ambacher, L.F. Eastman, J.R. Shealy, *Appl. Phys. Lett.* **75**, p. 388, 1999.

[3] M. Kamp, A. Pelzmann, C. Kirchner, M. Mayer, K.J. Ebeling, M. Leszczynski, I. Grzegory, and T. Suski, and S. Porowski, *MRS Internet J. Nitride Semicond. Res.* **4s1**, G10.2, 1999.

[4] C. Kirchner, V. Schwegler, F. Eberhard, M. Kamp, K.J. Ebeling, K. Kornitzer, T. Ebner, K. Thonke, R. Sauer, M. Leszczynski, I. Grzegory, S. Porowski, *Appl. Phys. Lett.* **75**, p. 1098, 1999.

[5] S. Porowski, M. Bockowski, B. Lucznik, M. Wroblewski, S. Krukowski, I. Grzegory, M. Leszczynski, G. Niwak, K. Pakula, J. Baranowski, *Mater. Res. Soc. Symp. Proc.* **449**, p. 35, 1999.

[6] M.K. Kelly, R.P. Vaudo, V.M. Phanse, L. Gorgens, O. Ambacher, M. Stutzmann, *Jpn. J. Appl. Phys.* **38**, p. L212, 1999.

[7] H.Y.A. Chung, C. Wang, Ch. Kirchner, M. Seyboth, V. Schwegler, M. Scherer, M. Kamp, K.J. Ebeling, R. Beccard, M. Heuken, *Accepted by Phys. Stat. Sol(a).*

[8] A. Usui, *Mater. Res. Soc. Symp. Proc.* **482**, p. 233, 1998.

[9] T.S. Zheleva, W.M. Ashmavi, K.A. Jones, *Phys. Stat. Sol. (a)* **176**, p. 545, 1999.

Low Resistive p-Type GaN Using a 2-step Rapid Thermal Annealing Processes

Marcus Scherer

2-step rapid thermal annealing processes were investigated for electrical activation of magnesium doped galliumnitride layers. The samples were studied by room temperature Hall measurements and photoluminescence spectroscopy at 16 K. After an annealing process consisting of a short-term step at 960 °C followed by a 600 °C dwell step for 5 min a resistivity as low as 0.84 Ωcm is achieved for the activated sample, which improves the results achieved by standard annealing (800 °C for 10 min) by 25% in resistivity and 100% in free hole concentration. Photoluminescence shows a peak centered at 3.0 eV, which is typical for Mg-doped samples with high free hole concentrations.

1. Introduction

In recent years, remarkable progress was achieved in GaN-based optical devices, such as high brightness LEDs for the green, blue and near ultraviolet regions of the visible spectrum and laser diodes with lifetimes beyond 10000 hours. However, all devices grown under hydrogen-rich ambient, such as metal organic vapor phase epitaxy (MOVPE), struggle with an initially generated, electrically inactive Mg-H complex, since the Mg-acceptor is passivated by hydrogen. Thus an additional processing step is necessary to activate the Mg and eventually to remove the hydrogen from the GaN films. This can be done either by low energy electron beam irradiation (LEEBI) [1] or thermal annealing under nitrogen atmosphere [2]. The second method achieved the recognition, although several additional features like photo-enhanced activation [3], annealing under minority-carrier injection [4] or in oxygen atmosphere [5] have been investigated. In this letter we report on the activation of Mg-doped GaN by 2-step rapid thermal annealing (RTA) in a N_2 environment focusing on minimization of the thermal budget required for activation. Eventually, the reduction of thermal budget, defined as process duration times temperature, for all device production steps is beneficial for the performance of the devices. For the activation step this can be achieved by an optimized process management (time and temperature) in combination with steep temperature ramps and an improved temperature control.

2. Experimental Procedure

Mg-doped GaN films are grown in a horizontal MOVPE reactor on (0001)-oriented (c-plane) sapphire. Trimethylgallium (TMGa) and ammonia (NH_3) are used as Ga and N precursors, respectively, and bis-(cyclopentadienyl)magnesium (Cp_2Mg) as p-type doping

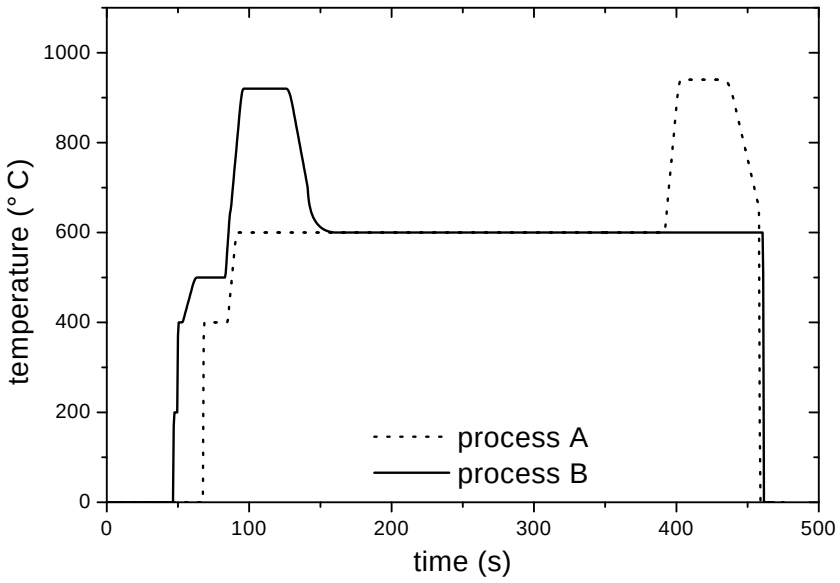

Fig. 1. Temperature profile of the examined 2-step RTA processes.

source. First a 30 nm low-temperature nucleation layer is grown on sapphire followed by 2 μm semi-insulating GaN ($n < 5\times10^{16}\,\mathrm{cm}^{-3}$) and 300 nm GaN:Mg. The wafer is cleaved into $5\times5\,\mathrm{mm}^2$ pieces and post-growth annealing under N_2-atmosphere is performed in a STEAG AST2800CS RTP system, capable of high temperature ramp rates up to 50 °C/s. In this study we investigate two different 2-step annealing processes as shown in Fig. 1 and compare the achieved data to a standard 800 °C 10 min annealing step performed in the same RTP system. The first RTP process utilizes the high temperature step at the end (process A) and the other has the high temperature step at the beginning (process B) of the process. The RTA processes consist of a 5 min low temperature step at 600 °C and a 30 s high temperature step at 850 °C, 920 °C, 940 °C, 960 °C, 980 °C and 1030 °C, respectively. After activating the magnesium dopant, Ni/Au contacts (20/200 nm) are evaporated onto the samples using a shadow-mask. Room-temperature (RT) Hall measurements are carried out using the van-der-Pauw method. Secondary ion mass spectroscopy (SIMS) and photoluminescence (PL) measurements are performed to complete the study.

3. Results and Discussion

Theory predicts an energy of 0.7 eV to overcome the binding energy of the Mg-H complex, but even higher energies are necessary to remove the hydrogen from the crystal and prevent the Mg from being passivated again [6]. The basic idea of process A is to separate this two steps, e.g. to crack the Mg-H complex during the dwell step (5 min) at low temperature (600 °C) and remove the dissociated H during the short high temperature step from the semiconductor material [7]. Process B exchanges the sequence of the two temperature steps to prove the basic idea of 2-step RTA. For process A a resistivity as low as

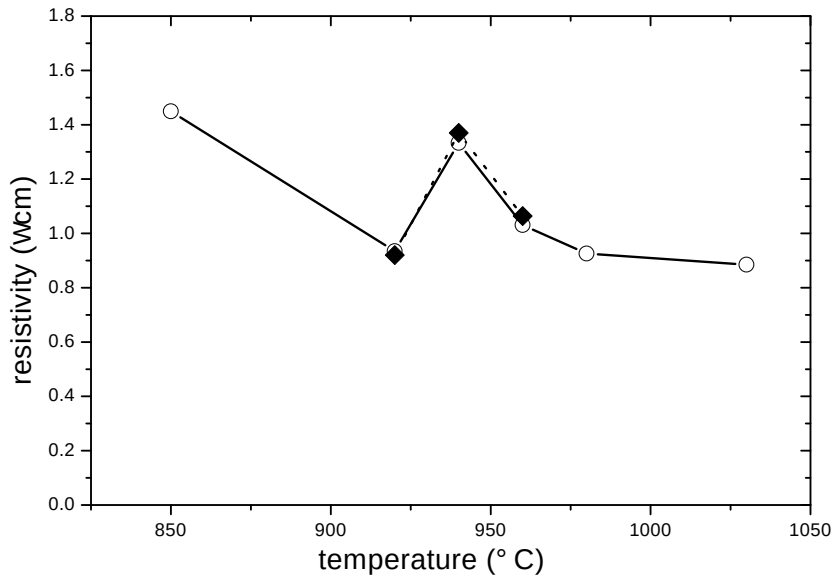

Fig. 2. Resistivities of the Mg-doped samples annealed by process A (circles) and the corresponding reproduced experiments (diamonds) (dwell conditions: 600 °C, 5 min).

$\rho = 0.88\,\Omega$cm is achieved for an annealing temperature of 1030 °C of the second step (Fig. 2, circles), which corresponds to a free carrier density of $p = 2.5\times10^{18}\,\mathrm{cm}^{-3}$ ($\mu_\mathrm{p} = 3\,\mathrm{cm}^2/\mathrm{Vs}$). For comparison, a resistivity of $\rho = 1.23\,\Omega$cm ($p = 9.8\times10^{17}\,\mathrm{cm}^{-3}$, $\mu_\mathrm{p} = 5\,\mathrm{cm}^2/\mathrm{Vs}$) was determined after activating the sample by a standard annealing process at 800 °C for 10 min. This improvement in free hole concentration shows, that during the standard process either not all of the Mg is activated or donors , e.g. nitrogen vacancies, are generated. Variation of the temperature of the initial step showed, that for a dwell temperature of 600 °C the highest conductivities could be achieved. The unexpected behavior for annealing temperatures around 940 °C cannot be explained so far, however reproduction of the experiments verified the temperature dependence (Fig. 2, diamonds).

The resistivity of the epitaxial layer can be further improved to $\rho = 0.84\,\Omega$cm using process B with a 960 °C high temperature step (Fig. 3, squares). For this sample, a free hole concentration of $9.9\times10^{17}\,\mathrm{cm}^{-3}$ was determined at a mobility of $7.5\,\mathrm{cm}^2/\mathrm{Vs}$. A conclusive explanation for this further improvement is not available so far. The idea of using only a single step at the respective temperatures of the high temperature step could be defeated, because experiments show that the achieved conductivities for this experiments are even lower than for the 800 °C annealing process. For annealing temperatures higher than 1030 °C and 980 °C for process A and B, respectively, the samples showed n-type conductivity probably induced by outdiffusion of nitrogen during the annealing process [8]. After Hall measurements all samples have been stored under vacuum conditions for a week and then annealed again at 400 °C for 5 minutes in a nitrogen atmosphere to allow residual hydrogen to repassivate the layer. The following Hall measurements showed no repassivation of the samples, so it could be concluded, that no hydrogen remains in the samples

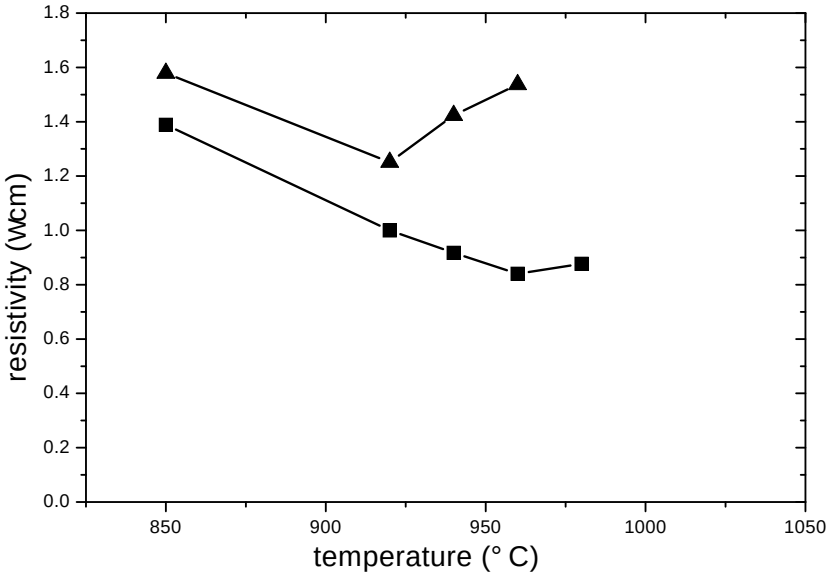

Fig. 3. Resistivities of the samples annealed by process B (high doping level: squares, low doping level: triangles) as a function of temperature of the high temperature step (dwell conditions: 600 °C, 5 min).

after the 2-step annealing process. Repeating the experiments with a sample grown with a reduced Mg-flux resulted in the same behavior according to the annealing process, although the optimum annealing temperature is slightly shifted (Fig. 3, triangles). This minor shift can be explained by varying dislocation densities [8].

PL measurements at 16 K are performed for samples activated by process B with a peak temperature of 960 °C and 1030 °C, resulting in the highest p-type, respectively n-type conductivity after annealing. The PL spectrum for the p-type sample (Fig. 4, striped line) shows a peak centered at 3.1 eV which is well known for highly Mg doped gallium-nitride [9]. For annealing temperatures higher than 1000 °C the spectrum gets broader and is shifted to a peak energy of 3.0 eV (Fig. 4, solid line). This corresponds to the increasing number of nitrogen vacancies (V_N) induced by nitrogen outdiffusion during the activation process. The activated Mg_{Ga} associate with the nearest neighbor V_N and form a deep-donor-complex. The photoluminescence peak at lower energy is an indication for donor-acceptor pair (DAP) transition from this deep donor centers for GaN:Mg with Mg concentration of more than 10^{19} cm^{-3} [10]. SIMS measurements of the investigated samples show Mg concentrations of $2-3\times10^{19}$ cm^{-3}. The DAP recombination between the deep donor states and the Mg acceptor levels is responsible for the shift of the PL-peak energy with increasing annealing temperature and the low energy tail of the PL spectra [9]. The peak at 3.27 eV (Fig. 4, arrow) is equal to the DAP found by Fischer et.al. [11] and its increase corresponds to the increasing number of activated acceptors for higher annealing temperatures [9].

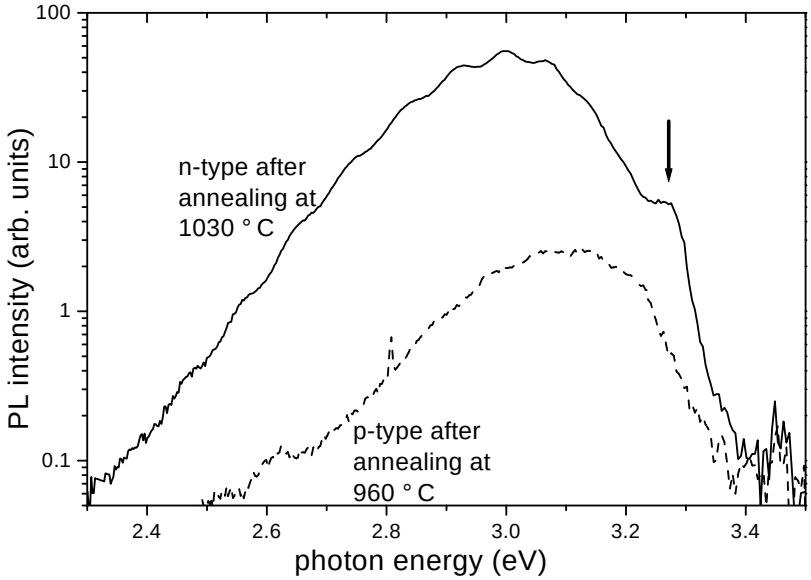

Fig. 4. PL measurements at 16 K for a sample showing p- (dashed line) and n-type (solid line) conductivity after annealing process.

4. Summary

In summary we were able to establish a 2-step annealing process that improves the electrical properties of Mg-doped GaN. Using a short-term step with temperatures higher than 940 °C followed by a 600 °C step for 5 minutes in a nitrogen atmosphere provides improved resistivity below 1 Ωcm for highly doped GaN:Mg films. This corresponds to an improvement of 25% in resistivity and 100% in free hole concentration compared to the results achieved for a standard annealing process at 800 °C for 10 min. PL studies show increasing luminescence at 2.8 eV for annealing temperature higher than 980 °C which is attributed to the formation of N vacancies during the annealing process.

References

[1] H. Amano, M. Kito, K. Hiramatsu, and I. Akasaki, "P-Type Conduction in Mg-Doped GaN Treated with Low-Energy Electron Beam Irradiation (LEEBI)", *Jpn. J. Appl. Phys.* **28**, pp. L2112–L2114, 1999.

[2] S. Nakamura, T. Mukai, M. Senoh, and N. Iwasa, "Thermal Annealing Effects on P-Type Mg-Doped GaN Films", *Jpn. J. Appl. Phys.* **31**, pp. L139–L142, 1992.

[3] Y. Kamiura, Y. Yamashita, and S. Nakamura, "Photo-Enhanced Activation of Hydrogen-Passivated Magnesium in P-Type GaN Films", *Jpn. J. Appl. Phys.* **37**, pp. L970–L971, 1998.

[4] M. Miyachi, T. Tanaka, Y. Kimura, and H. Ota, "The activation of Mg in GaN by annealing with minority-carrier injection", *Appl. Phys. Lett.* **72**(9), pp. 1101–1103, 1998.

[5] B.A. Hull, S.E. Mohney, H.S. Venugopalan, and J.C. Ramer, "Influence of oxygen on the activation of p-type GaN", *Appl. Phys. Lett.* **76**(16), pp. 2271–2273, 2000.

[6] J. Neugebauer, and C.G. Van De Walle, "Theory of Hydrogen in GaN", *Hydrogen in Semiconductors II*, edit. by N.H. Nickel, Semiconductor and Semimetals Vol. 61, Academic Press, pp. 479–502, 1999.

[7] K.-S. Ahn, D.-J. Kim, Y.-T. Moon, H.-G. Kim, and S.-J. Park, "Effect of Two-Step Rapid Thermal Annealing Process on Mg-doped p-type GaN Film Grown by Metalorganic Chemical Vapor Deposition", *2nd Intern. Symp. On Blue Lasers and Light Emitting Diodes*, Chiba, Th-P28, pp. 556–559, 1998.

[8] D.-H. Youn, M. Lachab, M. Hao, T. Sugahara, H. Takenaka, Y. Naoi, and S. Sakai, "Investigation on the P-Type Activation Mechanism in Mg-doped GaN Films Grown by Metalorganic Chemical Vapor Deposition", *Jpn. J. Appl. Phys.* **38**, pp. 631–634, 1999.

[9] P.H. Lim, B. Schineller, O. Schön, K. Heime, and M. Heuken, "Photoluminescence of GaN:Mg grown by metalorganic vapor-phase epitaxy (MOVPE)", *J. Crystal Growth* **205**, pp. 1–10, 1999.

[10] U. Kaufmann, M. Kunzer, M. Maier, H. Obloh, A. Ramakrishnan, B. Satic, and P. Schlotter, "Nature of the 2.8 eV photoluminescence band in Mg doped GaN", *Appl. Phys. Lett.* **72**(11), pp. 1326–1328, 1998.

[11] S. Fischer, C. Wetzel, E.E. Haller, and B.K. Meyer, "On p-type doping in GaN - acceptor binding energies", *Appl. Phys. Lett.* **67**(9), pp. 1298–1300, 1995.

Efficient Light-Emitting Diodes with Radial Outcoupling Taper at 970 and 630 nm Emission Wavelength

Wolfgang Schmid and Marcus Scherer

We have investigated efficient light outcoupling from light-emitting diodes (LEDs) by introducing lateral tapers. The concept is based on light generation in the very central area of a circularly symmetric structure. After propagating between two highly reflecting mirrors light is outcoupled in a tapered mesa region. By proper processing we achieve quantum efficiencies of almost 40 % for outcoupling via a planar surface or quantum and wallplug efficiencies of 52 % and 48 %, respectively, for encapsulated devices.

1. Introduction

One of the cardinal problems limiting the performance of light emitting diodes (LEDs) is their low external efficiency caused by total internal reflection of light in semiconductor material. Various approaches already exist to overcome this problem. Among those are resonant cavity LEDs with their modified internal direction of spontaneous emission [1, 2], surface textured devices with a back side mirror where photons repeatedly try to escape [3, 4], or the use of transparent substrates [5, 6]. We have suggested a new method of efficient light outcoupling from thin-film LEDs by introducing lateral tapers [7, 8]. The concept is based on light generation in the very central area of a circularly symmetric structure. After propagating between two highly reflecting mirrors light is outcoupled in a flat tapered mesa region. We present InGaAs based devices emitting at 970 nm with 52 % and 48 % quantum and wallplug efficiency, respectively. A simplified theoretical approach is used to discuss the outcoupling mechanism [9].

2. Results at 970 nm Wavelength

Fig. 1 shows the output characteristics of a 140 μm diameter device with an active diameter of 20 μm. Before encapsulation, the quantum efficiency is close to 30 %. Encapsulation raises the optical output power by an enhancement factor of 1.5 and the quantum efficiency reaches a value of 45 %. Due to the low resistance the wallplug efficiency has almost the same value of 44 %. The encapsulation enhancement factor for a conventional cubically shaped chip is typically around 2 [10]. In these chips light extraction benefits from broader escape cones and simultaneously lower interface reflectivities. The different behavior of

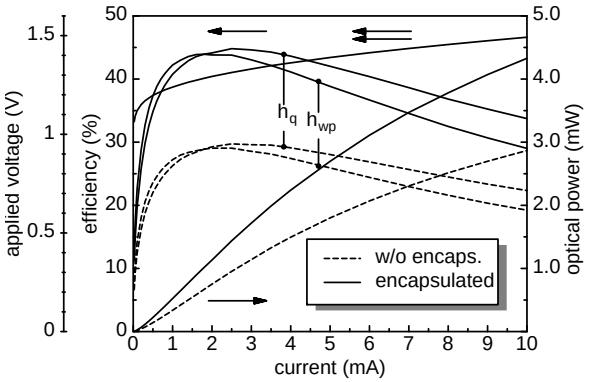

Fig. 1. Optical output power and quantum efficiency of a 140 μm device with and without encapsulation.

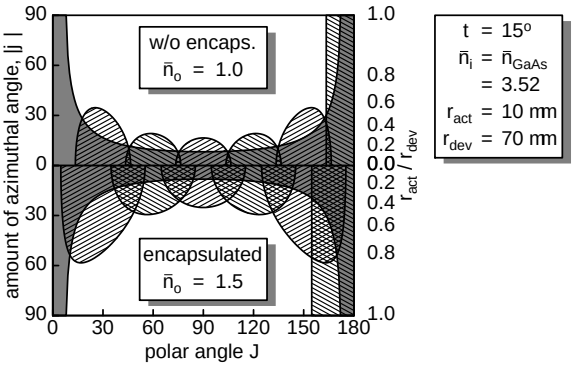

Fig. 2. Escape cones for an encapsulated and non-encapsulated device, respectively.

tapered LEDs can be explained by plotting the escape cones shown in Fig. 2. For the case of encapsulation the overlap of the cones is getting larger and some directions get more than one chance to escape. In conjunction with the smaller reflectivity this leads to an efficiency increase with encapsulation. Since on the other hand, already cones for non-encapsulated devices are covering all excited directions, we cannot expect as much enhancement as for conventional LEDs.

The characteristics of another device with roughly the same diameter are shown in Fig. 3. Before encapsulation, the quantum efficiency is close to 40 %. With encapsulation the quantum efficiency reaches 52 % resulting in a smaller encapsulation enhancement factor of 1.3. Due to the relatively high resistance, the wallplug efficiency is limited to 48 %. We relate the higher quantum efficiency to a smaller taper angle. The escape cones

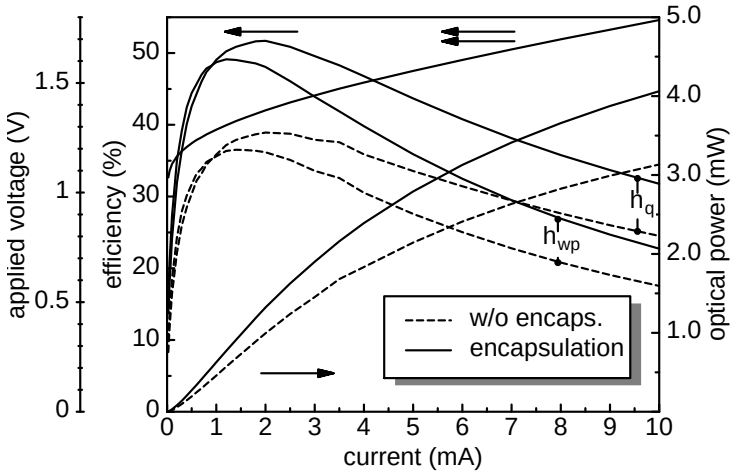

Fig. 3. Optical output power and quantum efficiency of a 140 μm diameter device with and without encapsulation. We assume a smaller taper angle compared to the device in Fig. 1.

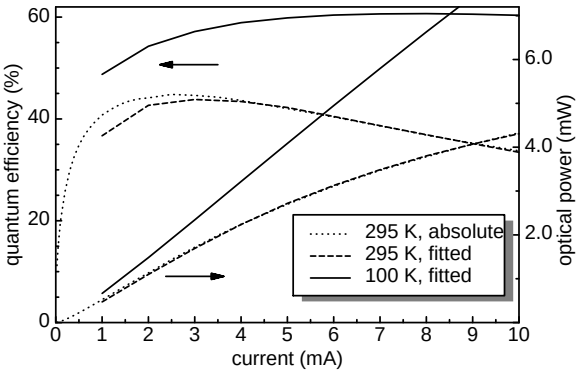

Fig. 4. Optical output power and quantum efficiency for two different ambient temperatures.

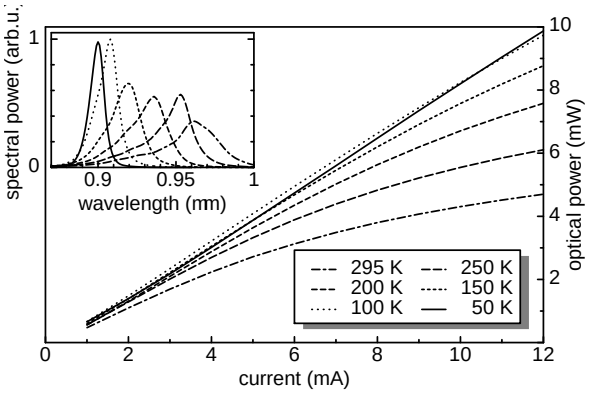

Fig. 5. Optical output power for different temperatures. The inset shows corresponding output spectra.

move closer and even for the non-encapsulated device light has a higher chance to escape. Accordingly, we expect a smaller encapsulation enhancement factor. Unfortunately, there is some uncertainty, since the taper angle of the processed device cannot be measured precisely without destroying the device.

We have used the 45 % efficiency device for low temperature investigations. Since the device should be cooled down in vacuum to avoid condensation of water at the surface, no absolute measurement of optical output power was possible. Therefore relative measurements were made at room temperature and fitted to the absolute data. For the low temperature data we take the same calibration factor. For every temperature the emission spectrum is recorded to take the sensitivity of the detector into account. Fig. 4 shows the optical output power for different heat sink temperatures. While the room temperature characteristic shows a slightly sublinear slope, the optical output power increases with current as at 100 K is an almost straight line. The quantum efficiency reaches 60 %. In a first order approximation this value can be regarded as the minimum outcoupling efficiency. Assuming temperature independent outcoupling the internal efficiency at room temperature is at least 75 %.

To be more precise, the outcoupling efficiency is not fully independent of temperature. Apart from a change of free carrier absorption, outcoupling is influenced by a temperature dependent active diameter. Emission spectra and optical output power are shown in Fig. 5. Especially for low temperatures of 50 K the optical output power shows a slightly superlinear behavior. At this temperature the high resistance of the homotype heterobarriers in the confining layers leads to current spreading. Increasing the current, the internal temperature reduces current spreading. However, as explained, a reduced active diameter improves outcoupling of light.

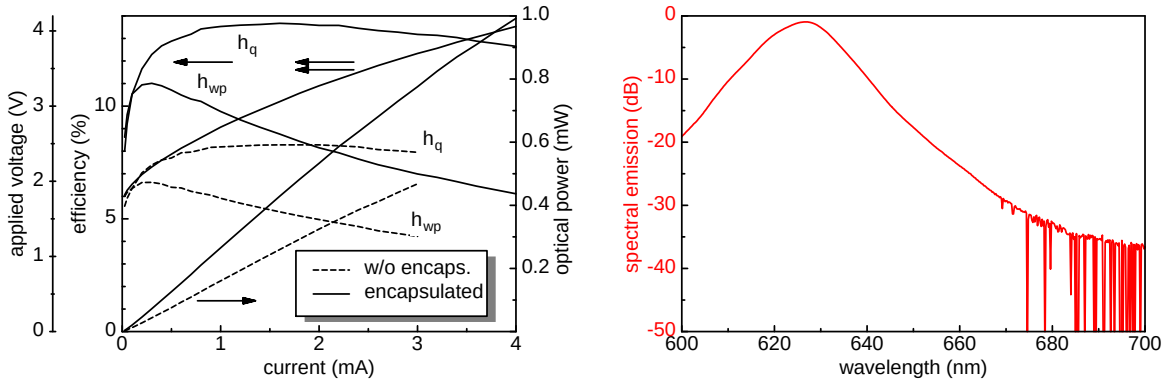

Fig. 6. Characteristics of a InGaAlP based, 630 nm red emitting LED with 120 μm diameter and emission spectra at 3 mA.

3. 630 nm Red Emitting LEDs

The uncomplicated epitaxial layer structure facilitates a process transfer to the InGaAlP material system for emission at about 630 nm.

Fig. 6 shows the characteristics of a prototype device. A high operating voltage is observed which can be related to bad ohmic contacts on Al containing layers, still requiring some optimization. Nevertheless we achieve encouraging 13 % quantum efficiency and 1 mW optical output power at a current of 4 mA.

A comparison of devices with different lateral sizes and variations in the overall active layer thickness is shown in Fig. 7. While infrared devices show a clear tendency of higher efficiency with larger diameter [8], red devices show no systematic dependence. Even devices with different overall active layer thicknesses and therefore different reabsorption in the outer unpumped region show no different slopes. Therefore we do not solely relate

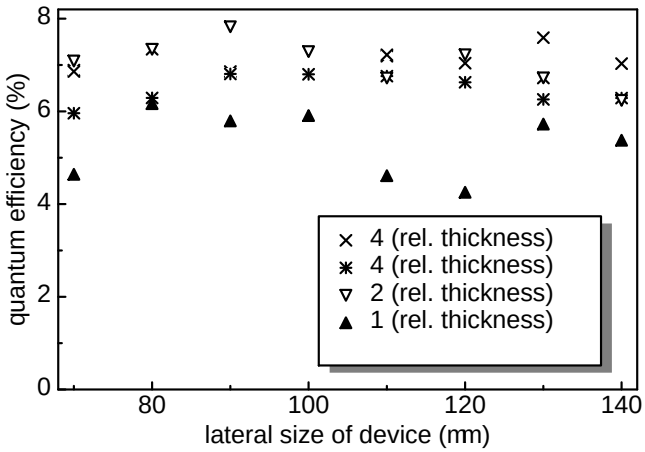

Fig. 7. Quantum efficiency at 2 mA for LEDs with different overall active layer thicknesses.

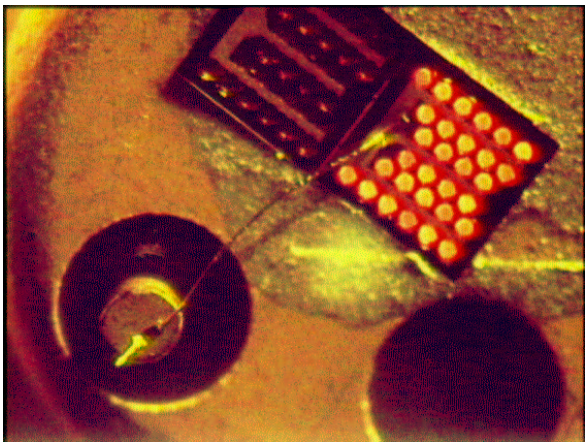

Fig. 8. Array of 30 devices within a total area of 1 mm^2.

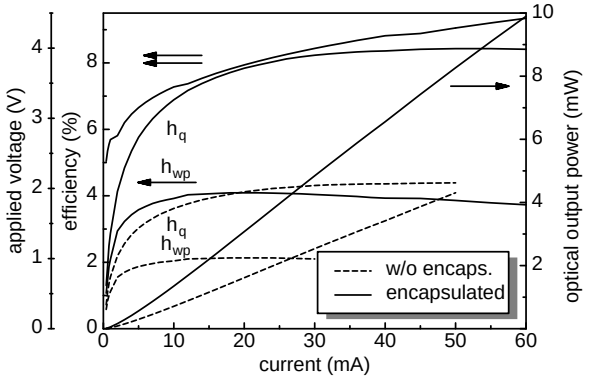

Fig. 9. Characteristics of 60 parallel driven devices with a total area of 2 μm.

the poorer performance to reabsorption nor a minor reflectivity of the metal mirror. A possible reason for the lower efficiency might be scattering at the tapered surface which is still rough compared to infrared emitting AlGaAs devices. Future work will focus on improvements in the chemical-assisted ion beam etching process.

As for technological reasons it is not to possible to significantly enlarge the device diameter to increase the overall optical output power, we have fabricated an array device driven in parallel. The processing sequence easily permits to use the same n-contact for all devices which can be contacted with a single bond. A first densely packed array of 30 devices with a total area of 1 mm^2 is depicted in Fig. 8. Each device has a lateral size of 120 μm. Fig. 9 shows the characteristics of two arrays driven in parallel. The quantum efficiency is lower compared to the non-encapsulated single device of Fig. 6, which is due to the comparatively rough surface of the taper. Nevertheless at a total current of 60 mA an optical output power of 10 mW is achieved. Due to heating of the TO-socket we have limited the current to this value which corresponds to 1 mA per device.

4. Summary

Latest generation LEDs emitting in the 970 nm wavelength regime exhibit maximum quantum and wallplug efficiencies of 52 % and 48 %, respectively. Devices show continuous-wave 4 mW output power at 10 mA driving current and 20 % wallplug efficiency resulting in potential optical output power densities of about 40 W/cm^2 at current densities of 100 A/cm^2 for operation of densely packed 2D tapered LED arrays. Currently, we transfer and optimize the processing route to InGaAlP based 630 nm red emitting devices. Future work will concentrate on improvements of contacts, dry etched tapers, and epitaxial layer structures.

References

[1] E.F. Schubert, N.E.J. Hunt, M. Micovic, R.J. Malik, D.L. Sivco, A.Y. Cho and G.J. Zydzik, "Highly efficient light-emitting diodes with microcavities", *Science* **265**, pp. 943–945, 1994.

[2] H. De Neve, J. Blondelle, P. van Daele, P. Demeester and R. Baets, "Recycling of guided mode light emission in planar microcavity light emitting diodes", *Appl. Phys. Lett.* **70**, pp. 799–801, 1997.

[3] I. Schnitzer, C. Caneau, T.J. Gmitter, A. Scherer and E. Yablonovitch, "30 % external quantum efficiency from surface textured, thin-film light-emitting diodes", *Appl. Phys. Lett.* **63**, pp. 2174–2176, 1993.

[4] R. Windisch, M. Kuijk, B. Dutta, G.H. Döhler, G. Borghs and P. Heremans, "High-Efficiency Surface-Textured LEDs", *Compound Semiconductors* **6**(6), pp. 55–58, 2000.

[5] D.A. Vanderwater, I.-H. Tan, G.E. Höfler, D.C. Defevere and F.A. Kish, "High-brightness AlGaInP light emitting diodes", *Proc. IEEE* **85**, pp. 1752–1763, 1997.

[6] M.R. Krames, M. Ochiai-Holcomb, G.E. Höfler, C. Carter-Coman, E.I. Chen, I.-H. Tan, P. Grillot, N.F. Gardner, H.C. Chui, J.-W. Huang, S.A. Stockman, F.A. Kish and M.G. Craford, "High-power truncated-inverted-pyramid $(Al_xGa_{1-x})_{0.5}In_{0.5}P$/GaP light-emitting diodes exhibiting >50% external quantum efficiency", *Appl. Phys. Lett.*, **75** (16), pp. 2365–2367, 1999.

[7] W. Schmid, F. Eberhard, M. Schauler, M. Grabherr, R. King, M. Miller, E. Deichsel, G. Stareev, U. Martin, R. Jäger, J. Joos, R. Michalzik and K. J. Ebeling, "Infrared Light-Emitting Diodes with Lateral Outcoupling Taper for High Extraction Efficiency", *Light-Emitting Diodes: Research, Manufacturing, and Applications III*, Proc. SPIE, **3621**, pp. 198–205, 1999.

[8] W. Schmid, F. Eberhard, R. Jäger, R. King, M. Miller, J. Joos and K.J. Ebeling, "45 % quantum-efficiency light-emitting diodes with radial outcoupling taper", *Light-Emitting Diodes: Research, Manufacturing, and Applications IV*, Proc. SPIE, **3938**, pp. 90–97, 2000.

[9] W. Schmid, M. Scherer, R. Jäger, P. Stauß, K. Streubel and K.J. Ebeling, "Efficient Light-Emitting Diodes with Radial Outcoupling Taper at 980 and 630 nm Emission Wavelength", to be published in *Light-Emitting Diodes: Research, Manufacturing, and Applications V*, Proc. SPIE, 2001.

[10] D.A. Vanderwater, I.-H. Tan, G.E. Höfler, D.C. Defevere and F.A. Kish, "High-Brightness AlGaInP Light-Emitting Diodes", *Proc. IEEE* **84** (11), pp. 1752–1763, 1997.

Extraction Efficiency of GaN-Based LEDs

Sven-Silvius Schad

Two different LED structures are investigated which provide high extraction efficiency in other material systems than gallium nitride (GaN). For near band edge emitting devices absorption has a major influence on the device performance. Simulation results, based on a ray tracing model, are presented to compare the two structures (For the taper LED the extraction efficiency is 35 % and for the truncated inverted pyramid LED 65 %).

First transmission measurements are introduced which allow an estimation of absorption in thin GaN-based films. This technique has been used to characterize Mg-doped GaN. We found a major influence of the standard activation process on the near band edge absorption ($\alpha = 426\,cm^{-1}$ at 400 nm before and $\alpha = 112\,cm^{-1}$ after activation).

1. Introduction

GaN based light emitters are promising in a variety of applications. The generation of white light is possibly the most important. This can be achieved by using an UV emitting LED in combination with a luminescence converter (LUCOLED). A high excitation density and short wavelengths typically in the range of 390 – 410 nm are necessary to pump these converters.

Several mechanisms prevent that the whole internal generated light is extracted. Simple models assume that only light which angle of incidence is smaller than the angle of total internal reflection, given by

$$\sin\theta = \frac{1}{n_{\mathrm{sem}}} \tag{1}$$

contributes to the extraction efficiency, where n_{sem} is the refractive index of the semiconductor. From (1) it is obvious that with $n_{\mathrm{sem}} \approx 2.5$ for GaN compared to other typical III-V semiconductor materials (e.g. GaAs, $n_{\mathrm{sem}} \approx 3.6$) the escape cone is larger. Looking more into details, absorption has to be considered as well as multi reflections. On the way from the active region to the surface, a fraction of the generated light is lost. There another part is reflected due to Fresnel or total internal reflection. This part has to travel through the device to the opposite surface and once again absorption reduces the intensity. By choosing a suitable geometry of the LED the average path length of a ray traced from the origin will be reduced and a higher extraction efficiency can be achieved. This has already successfully been shown for other material systems such as AlInGaP [1] or AlInGaAs [2] but the processing of such devices is difficult and needs special processing

steps (e.g. substrate removal). In particular for UV emitting LEDs a strong absorption is expected due to the band tail effect. Therefore, these special LED geometries are promising to improve the extraction efficiency. To compare different concepts a ray tracer has been developed which is able to calculate the extraction efficiency using a ray model. Polarization, Fresnel reflection and internal absorption are considered to get a reasonable prediction.

2. Simulation

Since it is necessary to limit the amount of arithmetic operations, we neglect p- and n-type doping as well as the presence of a quantum well. Thus, the LED has homogenous absorption and the refractive index of GaN. Therefore, this simple model can only be used as a rough estimation for the extraction efficiency. The average absorption α has been assumed to be 100 cm^{-1} and 300 cm^{-1}. We investigated two different types of LED structures, the truncated inverted pyramid (TIP) LED and the taper LED.

The taper LED has been successfully fabricated in the AlGaAs material system. Fig. 1 shows an overview of the structure. Light is generated in the center of the device and is laterally guided by a waveguide. In the tapered region the angle of incidence is reduced by the taper angle τ each time a surface is hit. Finally the incidence angle of the ray is smaller than the angle of total internal reflection and the light is coupled out. The LED is mounted upside down on a high reflective surface. Fig. 2 shows the calculated extraction efficiency versus the taper angle τ. A strong influence of the absorption has been expected since the intensity decrease obeys an exponential law in distance. For $\alpha = 100\,\mathrm{cm}^{-1}$ at an angle of 22° the maximum is achieved. Around that angle the extraction efficiency stays almost constant over a wide range. Towards large angles efficiency decreases. Simulations show that in this region standing ray patterns prevent extraction. For $\alpha = 300\,\mathrm{cm}^{-1}$ the extraction efficiency is nearly independent from the taper angle.

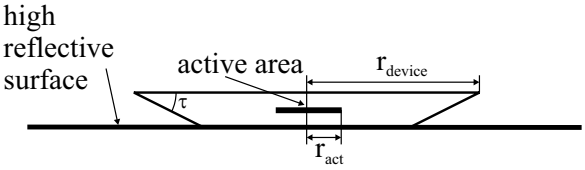

Fig. 1. Structure of a taper LED (schematic), according to [2]

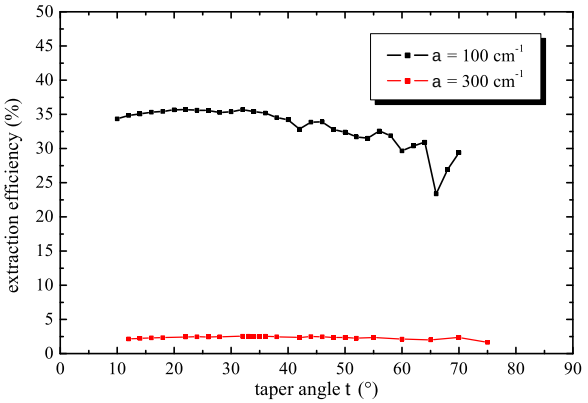

Fig. 2. Calculated efficiency of a taper LED vs. taper angle

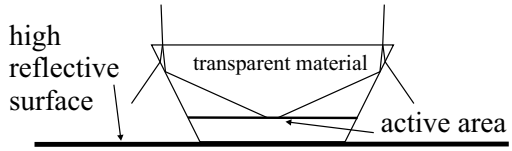

Fig. 3. structure of a TIP LED (schematic)

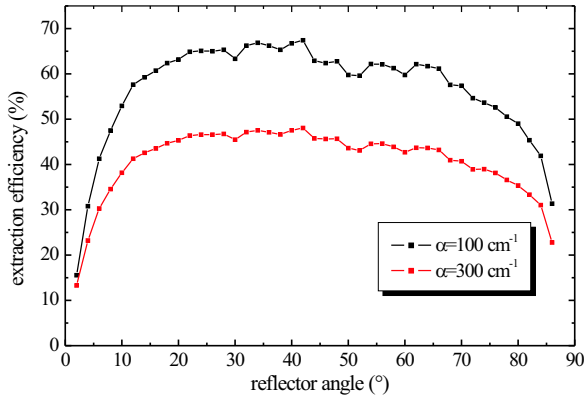

Fig. 4. calculated efficiency of a TIP-LED

Fig. 3 shows the basic configuration of a TIP-LED device. In the lateral center of the device the active region is located. On top a thick window layer [9] exists which is structured like a rectangular reflector. In the AlInGaP material system this layer is wafer fused GaP [1]. The contact to the cathode of the junction is on top of the device so the injection is through the transparent layer. The light extraction is achieved by redirecting totally internal reflected photons from the sidewall interfaces towards the top. There they pass the surface nearly with normal incidence, allowing them to escape. Another mechanism is that photons which are reflected at the surface are redirected to the sidewalls where extraction is possible. In summary the TIP-LED works mostly like a micro reflector.

The realization of such LED structures using nitrides is difficult. The TIP and the taper LED structures require a substrate removal. The material of the micro reflector has to be considered for the TIP-LED. For our simulation model we think that sawn sapphire can be used which is non conductive. Therefore, the LED has to be flip-chipped on a high reflective carrier to contact both sides of the pn-junction. This provides also an efficient heat sink. Fig. 4 shows the calculated extraction efficiency for the TIP-LED vs. the sidewall angle of the reflector with respect to horizontal. For a sidewall angle of 42° the maximum of generated light can be extracted. As can be seen from the diagram the efficiency for strong absorption is much better compared to the taper LED. This can be explained by the fact that the escape cone from the GaN into sapphire is larger than that of the taper LED. In case of the taper LED the refractive index of air limits the size of the cone. Limitation of the taper LED also occurs by the damping in the waveguide.

3. Characterization

It has been shown that absorption has a major influence on the device performance. To get an access to this critical parameter, a transmission measurement setup has been built. For thin films on a transparent substrate a solution for the calculation of the absorption has been given by [3]. For the nitrides the mainly used substrates are silicon carbide and sapphire. The latter one is transparent in the whole visible range and is therefore suitable

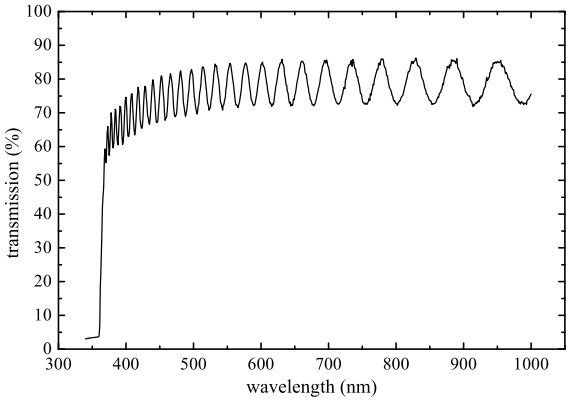

Fig. 5. transmission spectrum of p-type GaN

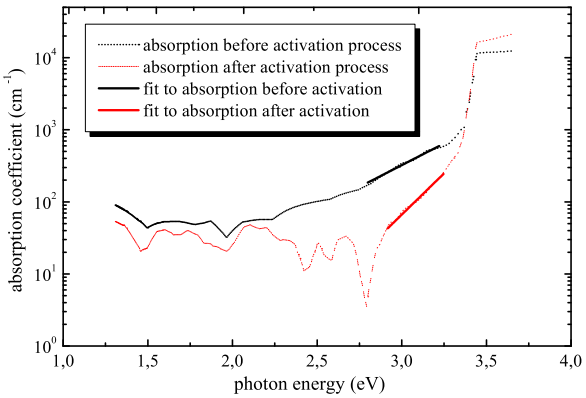

Fig. 6. absorption coefficient of p-type GaN

for the transmission measurements. To avoid scattering at the bottom surface, this side has also to be polished. Due to the lattice mismatch of sapphire and gallium nitride a nucleation and a buffer layer is grown. This is necessary to reduce the defects and to get an appropriate material quality. Considering a LED, the p- and n-type doped layers and InGaN-quantum well structures are of interest. When applying the two layer model, the thick buffer layer ($\approx 2\,\mu$m) leads to a systematic error yielding in a too small absorption coefficient. Nevertheless, researchers use this method for the determination of the optical properties [4, 5, 6, 7, 8].

Fig. 5 shows a typical transmission spectrum of a GaN film on sapphire substrate. Three regions can be distinguished: below 370 nm strong absorption is observed since the photon energies are higher than the bandgap energy of GaN ($E_\mathrm{g} = 3.39\,\mathrm{eV}$). In the middle region (380 to 600 nm) weak absorption is present whereas to longer wavelengths transmission T is limited by the refractive index of sapphire n_s by

$$T = \frac{2n_\mathrm{s}}{n_\mathrm{s}^2 + 1} \tag{2}$$

In the latter two regions the transmission spectrum is dominated by interference fringes from which the thickness of the film can be derived. Taking the envelope functions into account the absorption and the refractive index of the film can be calculated [3]. It is expected that the major part of the average absorption in the device occurs in the p-doped region, since the band tail effect increases with higher doping concentrations. Therefore, we investigated a p-doped sample which absorption coefficient is shown in Fig. 6. After growth the Mg-donor is inactive and has to be activated. Measurements have been made before and after the standard activation process (800 °C, 10 min, N_2) in which the H-Mg bond is broken. Around 3.1 eV a significant reduction of the absorption is observed after activation. For a wavelength of 400 nm the absorption coefficient is $\alpha = 426\,\mathrm{cm}^{-1}$ before and $\alpha = 112\,\mathrm{cm}^{-1}$ after activation.

4. Conclusion

The extraction efficiencies of a GaN based taper LED and a TIP-LED have been simulated. Best results were found for a taper angle of $\tau = 22°$ and for a sidewall angle of 44° for the TIP-LED, respectively. Simulations show clearly that the TIP-LED is superior to the taper LED when strong absorption is present. Transmission measurements show that the absorption in the p-region of the device is larger than $\alpha = 112\,\mathrm{cm}^{-1}$. Therefore, for UV emitting devices we think that the highest extraction efficiency may be achieved by a TIP-LED design.

References

[1] M.R. Krames, M. Ochiai-Holcomb, G.E. Hoefler, C. Carter-Coman, E.I. Chen, I.-H. Tan, P. Grillot, N.F. Gardner, H.C. Chui, J.-W. Huang, S.A. Stockman, F.A. Kish, M.G. Craford, T.S. Tan, C.P. Kocot, M. Hueschen, J. Posselt, B. Loh, G. Sasser and D. Collins, "High-power truncated-inverted-pyramid $(Al_xGa_{1-x})_{0.5}In_{0.5}P$/GaP light-emitting diodes exhibiting $>$ 50% external quantum efficiency", *Appl. Phys. Lett.* **75**, pp. 2365–2367, 1999.

[2] W. Schmid, F. Eberhard, M. Schauler, M. Grabherr, R. King, M. Miller, E. Deichsel, G. Stareev, U. Martin, R. Jaeger, J. Joos, R. Michalzik and K.J. Ebeling "Infrared Light-Emitting Diodes with Lateral Outcoupling Taper for High Extraction Efficiency", *Light-Emitting Diodes: Research, Manufacturing, and Applications III, SPIE Proc.*, pp. 198–205, 1999.

[3] R. Swanepoel "Determination of the thickness and optical constants of amorphous silicon", *J. Phys. E: Sci. Instrum.* **16**, pp. 1214–1222, 1983.

[4] J.F. Muth, J.H. Lee, I.K. Shmagin, R.M. Kolbas, H.C. Casey, B.P. Keller, U.K. Mishra, S.P. DenBaars "Absorption coefficient, energy gap, exciton binding energy, and recombination lifetime of GaN obtained from transmission measurements", *Appl. Phys. Lett.* **71**, pp. 2572–2574, 1997.

[5] J.W. Kim, Y.K. Park, Y.T. Kim, C.-S. Son I.-H. Choi, O. Ambacher and M. Stutzmann "Transmission Spectra of InGaN Single Quantum Wells and InGaN/GaN Heterostructures Grown by Metalorganic Chemical Vapor Deposition", *J. Korean Phys. Soc.* **35**, pp. 42–45, 1999.

[6] G.Y. Zhao, H. Ishikawa, H. Jiang, T. Egawa, T. Jimbo and M. Umeno "Optical Absorption and Photoluminescence Studies of n-type GaN", *Jpn. J. Appl. Phys.* **38**, pp. 993–995, 1999.

[7] D. Brunner, H. Angerer, E. Bustarret, F. Freudenberg, R. Hoepler, R. Dimitrov, O. Ambacher and M. Stutzmann "Optical constants of epitaxial AlGaN films and their temperature dependence", *J. Appl. Phys.* **82**, pp. 5090–5096, 1997.

[8] G. Yu, G. Wang, H. Ishikawa, M. Umeno, T. Soga, T. Egawa, J. Watanabe, T. Jimbo "Optical properties of wurzite structure GaN on sapphire around fundamental absorption edge (0.78-4.77 eV) by spectroscopic ellipsometry and the optical transmission method", *Appl. Phys. Lett.* **70**, pp. 2309-3211, 1997.

[9] K.H Huang, J.G. Yu, C.P. Kuo, M. Fletcher, T.D. Osentowski, L.J. Stinson, M.G. Craford and A.S.H. Liao "Twofold efficiency improvement in high performance AlGaInP light-emitting diodes in the 555-620 nm spectral region using a thick GaP window layer", *Appl. Phys. Lett.* **61**, pp. 1045–1047, 1992.

GaN-Based Lasers on SiC: Influence of Mirror Reflectivity on L-I Characteristics

Veit Schwegler and M. Selim Ünlü

Threshold current density and differential slope efficiency as function of end-mirror reflectance have been measured to estimate the internal losses of GaN-based laser diodes. An Al-coated fiber tip is used as an external micro-mirror to vary the reflectance of the end facets allowing for a continuous adjustment of mirror losses of a particular laser. The effective reflectance of the external resonator is modeled as function of facet reflectivities, emission wavelength, micro-mirror distance and laser mode shape. In contrast to other methods, this eliminates all ambiguities usually arising from the comparison of devices of varying length or mirror coatings. In GaN-lasers with high threshold current transparency loss for the gain medium is not negligible and, therefore, i_{th} dependence on mirror reflectivity alone is not sufficient to determine internal losses. Our measurements of one-facet slope efficiency yields internal losses $\langle \alpha_{int} \rangle$ between $27\,cm^{-1}$ and $46\,cm^{-1}$ whereas for derivation from current threshold a combination of transparency and internal losses in the range of $58\,cm^{-1}$ to $67\,cm^{-1}$ has been obtained.

1. Introduction

Whereas blue and green light emitting diodes (LEDs) have already been successfully commercialized, ultraviolet laser diodes (LDs) are still challenging for epitaxial growth and process technology arising from the specific material properties [1]. The low refractive index of GaN at 400 nm leads to a significantly reduced mirror reflectance of 0.18 according Fresnel equations. The mirror reflectance is further decreased by any interface roughness, as it typically appears for all dry chemical etched laser facets [3]. The weak dependence of refractive index on Al-content together with epitaxial limits on Al-content and AlGaN thickness yield a relatively poor optical confinement. Furthermore, due to the high number of dislocations acting as scattering centers the waveguide is susceptible to absorption losses. Since mirror losses have been overcome either by HR coating with dielectric $\lambda/4$ mirrors or usage of SiC and GaN substrates which allow cleaving, internal losses have moved into focus for further device optimization.

Usually, the internal losses are estimated from laser threshold of different cavity lengths and mirror coatings. Using different devices might cause ambiguities due to epitaxial inhomogeneity and various processing. Laser diodes relying on cleaved or etched GaN/air facets are quite sensitive to external optical feedback. An external micro-mirror can,

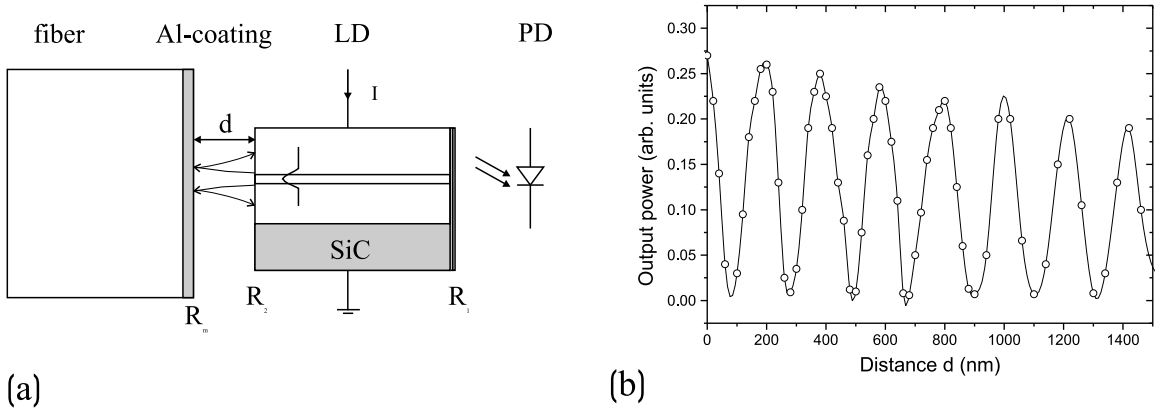

Fig. 1. (a) Experimental setup. (b) Optical output power as a function of micro-mirror distance from the HR-coated laser facet at constant current.

therefore, be used to increase the effective mirror reflectance significantly. Moreover, changes in the distance between the butt coupled micro-mirror and the facet influence the feedback into the laser diode, so an adjustable facet reflectance can be realized [2]. In this paper, we present the estimation of internal losses and transparency losses by continuous variation of mirror reflectivity on a single diode.

2. Experimental Setup

The devices under investigation are separate confinement double heterostructure (SCH) lasers grown by MOVPE on SiC substrates. Oxide stripe lasers have been fabricated from those structures with a 600 μm x 6 μm geometry. The facets are formed by cleaving the thinned substrate. Within this study laser diodes with one highly reflecting (HR) and one uncoated facet are used. The HR-coating consists of a stack of $\lambda/4$ dielectric layers and has a nominal reflectance of 0.95 to 0.98. Further details concerning structure and chip technology are reported elsewhere [4]. Fig. 1a shows the experimental setup. A cleaved fiber facet with 100 μm diameter and a 200 nm thick Al-coating is used as an external micro-mirror. Within the examined wavelength range between 400 nm and 410 nm the reflectance of the mirror is estimated of about 0.91. To align the micro-mirror in front of the uncoated laser facet, a piezo controlled xyz-stage with a resolution of approximately 10 nm is used. The optical output power of the laser diode is collected from the HR-coated facet by a microscope objective and imaged on a photodiode. To allow for correction of additional tilt errors the sample is mounted on a 4-axis waveguide manipulator. For measuring the L-I characteristics the device is biased with a current of 1 mA and driven by 50 ns long pulses at a duty cycle of 0.05%.

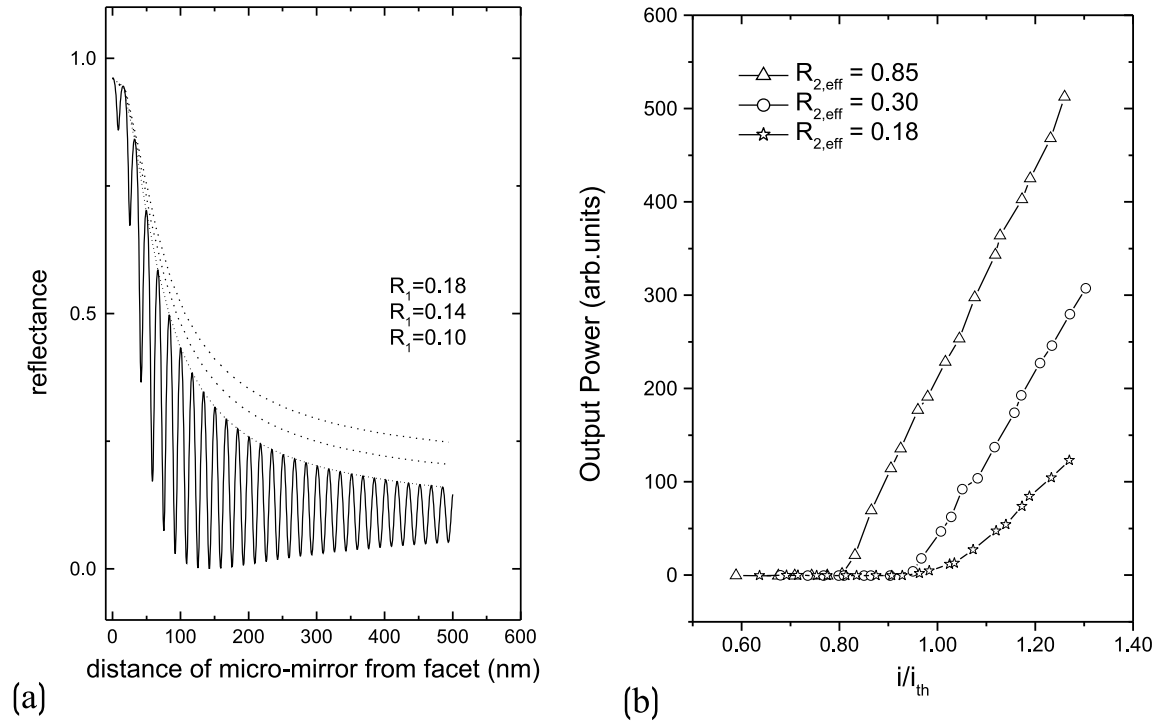

Fig. 2. (a) Calculated effective reflectance $R_{2,\mathrm{eff}}$ as function of micro-mirror distance from uncoated laser facet ($R_1 = 0.91$, $R_2 = 0.18$). The observed exponential decay is due to divergence of the laser beam which leads for increasing distance d to reduced back-reflection into the laser mode. Additional curves represent lowered values of the uncoated facet reflectance R_2, typically induced by surface roughness due to dry-etching. (b) L-I characteristics taken from the HR-coated facet for different positions of the micro-mirror corresponding to various effective reflectances $R_{2,\mathrm{eff}}$. For increasing values of $R_{2,\mathrm{eff}}$ significant threshold current reduction and improved slope efficiency is observed.

3. Results and Discussion

Fig. 1b shows the optical output power measured from the HR-coated facet at constant current as a function of mirror distance d to the uncoated facet. The output power reveals characteristic Fabry-Perot resonances resulting from coupling a second external resonator which is formed by the uncoated GaN facet, the air gap and the micro-mirror. Since the laser beam diverges, towards larger distances d the overlap of back-reflected optical field and the laser diode's mode profile decreases. This weakens the overall feedback into the laser shown by an exponential decay which envelopes the output power oscillations. For estimation of internal losses the system is treated as a solitary laser diode substituting the external resonator by an output facet with variable effective reflectance $R_{2,\mathrm{eff}}(d)$. Modeling of $R_{2,\mathrm{eff}}(d)$ is a crucial point for the following considerations and takes into account the reflectance of the HR-coated facet R_1, the uncoated GaN-facet R_2 and

micro-mirror R_m, emission wavelength λ, micro-mirror distance d and laser mode shape. The mode shape was calculated by a waveguide simulation program and confirmed by far field measurements. Losses because of divergence are taken into account by propagating the beam twice the air resonator length and calculating the overlap of beam profile with the laser mode. In Fig. 2a the calculated effective reflectance $R_{2,\mathrm{eff}}(d)$ is plotted for $R_\mathrm{m} = 0.9$ and $R_2 = 0.18$. The qualitative shape of the of the R_2 versa d dependence is similar to that of the measured output power, featuring same strong oscillation and characteristic exponential decay. Additional envelopes sketch the influence of reduced R_2 as it is typically obtained for increased surface roughness due to dry-etching. Atomic force microscopy (AFM) measurements on the laser facets revealed a root mean square surface roughness of the cleaved facets of about 1 nm indicating that the roughness is not a significant factor [5]. Therefore, in the following considerations a reflectance $R_1 = 0.18$ for the uncoated GaN-facet is used. Fig. 2b depicts I-L-characteristics taken from the HR-coated facet for different positions of the micro-mirror corresponding to various effective reflectances $R_{2,\mathrm{eff}}$. The expected dependence of slope efficiency η_d and i_th on mirror reflectivity is experimentally verified. For increasing values of $R_{2,\mathrm{eff}}$ significant threshold current reduction and improved slope efficiency are observed. When the micro-mirror is in close proximity of the facet corresponding to the highest output power at constant current, the single-facet slope efficiency is improved by factor of 2 and the threshold current is reduced by approximately 20% as compared to the device without micro-mirror. Both, variation of threshold current density and slope efficiency shall now be taken to estimate the internal losses and the transparency losses. According to [6] threshold current follows the equation

$$i_\mathrm{th} = \frac{q v_\mathrm{g}}{\tau_\mathrm{c} G_\mathrm{N}} \left[\frac{N_0 G_\mathrm{N}}{v_\mathrm{g}} (\alpha_\mathrm{mir} + \langle \alpha_\mathrm{int} \rangle + \alpha_\mathrm{transp}) \right] \tag{1}$$

with N_0 being equilibrium number of electrons, τ_c the carrier lifetime, v_g the group velocity, $\langle \alpha_\mathrm{int} \rangle$ and α_mir the internal and distributed mirror losses and α_transp the transparency losses. For a standing wave laser with two facet reflectivities R_1, R_2 and resonator length L, the mirror losses are given by

$$\alpha_\mathrm{mir} = \frac{1}{2L} \ln \frac{1}{R_1 R_2} \tag{2}$$

Since R_1 represents the HR-coated facet ($R_1 = 0.95 \ldots 0.98$) and $\ln(1/x) \gg 1 - x$ for $x \gg 1$, (1) can be rewritten and simplified by introducing the constants A, B

$$i_\mathrm{th} = A \left[B + \langle \alpha_\mathrm{int} \rangle + \frac{1}{2L}(1 - R_1) + \frac{1}{2L} \ln \frac{1}{R_{2,\mathrm{eff}}} \right] \approx A \left[B + \langle \alpha_\mathrm{int} \rangle + \frac{1}{2L} \ln \frac{1}{R_{2,\mathrm{eff}}} \right] \tag{3}$$

Comparison with literature gives typical values of $\langle \alpha_\mathrm{int} \rangle$ between $35\,\mathrm{cm}^{-1}$ and $45\,\mathrm{cm}^{-1}$ [7, 8], therefore the term containing R_1 can be neglected. For simulated values of $R_{2,\mathrm{eff}}$, (3) can be used to fit the internal losses $\langle \alpha_\mathrm{int} \rangle$. The obtained values of $\langle \alpha_\mathrm{int} \rangle$ are between $58\,\mathrm{cm}^{-1}$ and $67\,\mathrm{cm}^{-1}$ depending on the particular device. Similarly, starting from the output power

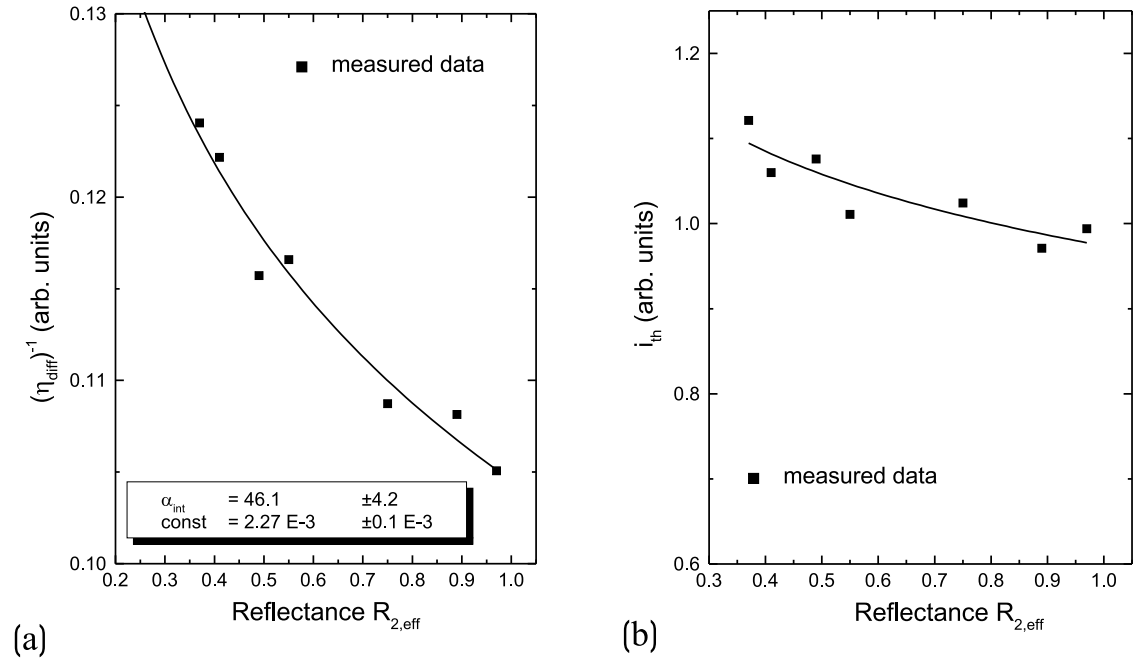

Fig. 3. Estimation of internal losses in dependence of (a) threshold current density variation and (b) changes in the slope efficiency.

P_{opt} for a standing wave laser, the one facet slope efficiency for the HR-coated facet could be derived according to [9]

$$\eta_{\mathrm{d}} \propto \frac{\partial P_{\mathrm{opt}}}{\partial i} \propto \frac{T_1}{\frac{1}{2L}\ln\frac{1}{R_{2,\mathrm{eff}}} + \langle\alpha_{\mathrm{int}}\rangle + T_1}, (i > i_{\mathrm{th}}) \tag{4}$$

P_{opt} being the optical output power, T_1 the transmittance of the HR-coated facet, $\langle\alpha_{\mathrm{int}}\rangle$ the internal losses, and i, i_{th} the forward and threshold currents, respectively. Since slope efficiency is taken above laser threshold and represents a differential figure it only considers internal losses like waveguide and scattering losses. The obtained values for these are in the range of $27\,\mathrm{cm}^{-1}$ and $46\,\mathrm{cm}^{-1}$.

4. Conclusion

We examined the influence of an external micro-mirror to the L-I-characteristics of GaN-based laser diodes. Both, threshold current density and differential slope efficiency can be improved significantly by increasing the effective mirror reflectance. Modeling of the effective mirror reflectance allows the estimation of internal losses from change of threshold current density and differential quantum efficiency in dependence on adjusted mirror reflectivity. Depending on the particular device values of $\langle\alpha_{\mathrm{int}}\rangle$ between $27\,\mathrm{cm}^{-1}$ and $46\,\mathrm{cm}^{-1}$

for derivation from differential quantum efficiency are obtained, which is in good agreement with data extracted from laser threshold of different cavity lengths (30–50 cm^{-1}). For variation of current threshold internal losses in the range of 58 cm^{-1} to 67 cm^{-1} have been calculated. The values of internal losses estimated from threshold behavior contain additionally transparency losses and are therefore slightly increased.

References

[1] S. Nakamura, "Present Status of InGaN-Based Laser Diodes", *phys. stat. sol. (a)* **176**, pp. 15–22, 1999.

[2] Y. Sidorin, D. Howe, "Some characteristics of an extremely-short-external-cavity laser diode realized by butt coupling a Fabry-Perot laser diode to a single-mode optical fiber", *Appl. Optics* **37**, (15), pp. 3256-3263, 1999.

[3] D.A. Stocker, E.F. Schubert, W. Grieshaber, K.S. Boutros, J.M. Redwing, "Facet roughness analysis for InGaN/GaN lasers with cleaved facets", *Appl. Phys. Lett.* **73**, pp. 1925–1927, 1998.

[4] S. Bader, B. Hahn, H.J. Lugauer, A. Lell, A. Weimar, G. Brüderl, J. Baur, D. Eisert, M. Scheubeck, S. Heppel, A. Hangleiter, V. Härle, "First European GaN-Based Violet Laser Diode", *phys. stat. sol. (a)* **180**, pp. 177–182, 2000.

[5] M. Scherer, V. Schwegler, M. Seyboth, F. Eberhard, C. Kirchner, M. Kamp, G. Ulu, M.S. Ünlü, R. Gruhler, O. Hollricher, "Characterization of Etched Facets for GaN-based Lasers", *to be published in J. Chryst. Growth*, 2001.

[6] G.P. Agrawal, "Fiber-Optic Communication Systems", Wiley, 1992.

[7] S. Nakamura, "Characteristics Of Room Temperature-CW Operated InGaN Multi-Quantum-Well-Structure Laser Diodes", *J. Nitride Semicond.Res.* **2**, 5, 1999.

[8] D.P. Bour, M. Kneissl, L.T. Romano, R.M. Donaldson, C.J. Dunnrowicz, N.M. Johnson, G.A. Evans, "Stripe-width dependence of threshold current for gain-guided AlGaInN laser diodes", *Appl. Phy. Lett.* **74**,(3) pp. 404–406, 1999.

[9] J.T. Verdeyen, "Laser Electronics", Prentice Hall, 1997.

[10] V. Härle, A. Lell, S. Bader, B. Hahn, H.J. Lugauer, F. Kühn, A. Weimar, "GaN-Based LEDs and Lasers on SiC", *phys. stat. sol. (a)* **180**, pp. 5–13, 2000.

Ph.D. Theses

[1] Peter Schnitzer, "Hochbitratige optische Datenübertragung mit selektiv oxidierten Vertikallaserdioden", Ph.D. Thesis, Optoelectronics Department, 2000.

[2] Markus Mayer, "Reaktive Molekularstrahlepitaxie für Leuchtdioden im InAlGaN-Materialsystem", Ph.D. Thesis, Optoelectronics Department, 2000.

[3] Günter Jost, "Hochleistungs-Laserverstärker auf der Basis von InGaAs-AlGaAs-GaAs", Ph.D. Thesis, Optoelectronics Department, 2000.

[4] Stefan Morgot, "Halbleiter-Trapezverstärker als Laserstrahlquellen hoher Brillanz", Ph.D. Thesis, Optoelectronics Department, 2000.

[5] Martin Grabherr, "Oberflächenemittierende Leistungsdiodenlaser mit Vertikalresonator", Ph.D. Thesis, Optoelectronics Department, 2000.

Diploma Theses and Semester Projects

[1] Sven-Silvius Schad, "Verbesserung des externen Quantenwirkungsgrades GaN-basierender Leuchtdioden", Diploma Thesis, Optoelectronics Department, 2000.

[2] Alexei Cheleg, "Wide temperature range characterization of high-performance vertical-cavity surface-emitting lasers for optical fiber data transmission", Masters Thesis, Optoelectronics Department, 2000.

[3] Axel Straub, "Vertikal emittierende Laserstrukturen mit integrierter Tunneldiode", Diploma Thesis, Optoelectronics Department, 2000.

[4] Karsten Schmidt, "Transparente Kontakte für GaN-basierende Leuchtdioden", Semester Project, Optoelectronics Department, 2000.

[5] Torsten Sven Schaal, "Modenmischung in und Bandbreite von Standard PMMA Fasern", Semester Project, DaimlerChrysler Forschungszentrum Ulm, 2000.

[6] Barbara Neubert, "Herstellung und Untersuchung von getaperten InAlGaP Leuchtdioden und Leuchtdiodenarrays", Semester Project, Optoelectronics Department, 2000.

Talks

[1] H.Y.A. Chung, C. Wang, and M. Kamp, "GaN-Wachstum mit der HVPE", *Seminar*, Ferdinand-Braun Institut für Höchstfrequenztechnik, Berlin, Germany, Jan., 2000.

[2] H.Y.A. Chung, C. Wang, C. Kirchner, M. Seyboth, V. Schwegler, M. Scherer, M. Kamp, K.J. Ebeling, R. Beccard, and M. Heuken, "Hydride vapour phase epitaxy growth of GaN layers under reduced reactor pressure", *Third International Symposium on Blue Laser and Light Emitting Diodes, ISBLLED 2000*, Zeuthen/Berlin, Germany, Mar., 2000.

[3] K.J. Ebeling, "Electrical-optical circuit board, EOCB", *Öffentliches Statusseminar*, Fraunhofer-Institut für Zuverlässigkeit und Mikrointegration, Berlin, Germany, Jan., 2000.

[4] K.J. Ebeling, "Low-noise high speed VCSELs and arrays for optical interconnects", *Internationales Symposium on Ultra-Parallel Optoelectronics*, Kawasaki, Japan, Feb., 2000.

[5] K.J. Ebeling, "VCSELs: Status und Aussichten", *Seminar Quantenelektronik*, ETH Zürich, Switzerland, Apr., 2000.

[6] K.J. Ebeling, "VCSELs und Anwendungsmöglichkeiten", *Seminar*, Institut für Lasertechnik in der Medizin, Ulm, Germany, Apr., 2000.

[7] K.J. Ebeling, "Vertical cavity semiconductor lasers (VCSELs) for data communications", *Short course, European Conference on Optical Communications, ECOC 2000*, München, Germany, Sept., 2000.

[8] I. Ecker, S. Menzel, J. Joos, and K.J. Ebeling, "Wachstum von GaAsSb/GaAs Laserdioden für den langwelligen Emissionsbereich", *MBE-Workshop 2000*, Bochum, Germany, Sept., 2000.

[9] M. Kamp, V. Schwegler, C. Kirchner, H.Y. Chung, C. Wang, M. Seyboth, M. Scherer, and K.J. Ebeling, "GaN-based light emitters on quasi-substrates", *Third International Symposium on Blue Laser and Light Emitting Diodes, ISBLLED 2000*, Zeuthen/Berlin, Germany, Mar., 2000.

[10] M. Kamp, V. Schwegler, M. Scherer, C. Kirchner, and M. Seyboth, "Advanced characterization for GaN-based LEDs", *E-MRS*, Strasbourgh, France, June, 2000.

[11] M. Kicherer, "Optische Übertragungssysteme mit integrierten Halbleiter-Lasern", *Optische Netze Forum 2000*, ComConsult Akademie, Bonn, Germany, Dec., 2000.

[12] R. Michalzik, F. Mederer, R. King, M. Kicherer, R. Jäger, and K.J. Ebeling, "Very short reach interconnect applications of vertical-cavity surface-emitting laser diodes", *U.R.S.I. Kleinheubacher Tagung 2000*, Schloß Kleinheubach, Germany, Sept., 2000.

[13] R. Michalzik, "An overview over the use of VCSELs for optical interconnection", *Future Technology Forum*, IBM Deutschland Entwicklung GmbH, Böblingen, Germany, June, 2000.

[14] R. Michalzik, "High-speed parallel optical interconnects — A sample of European research activities", *Symposium on Optical Interconnects and Related Technologies for Computers*, IBM T.J. Watson Research Center, Hawthorne, NY, USA, May, 2000.

[15] M. Scherer, A. Pelzmann, V. Schwegler, C. Kirchner, M. Seyboth, and M. Kamp, "Influence of multiple step annealing on p-type conductivity and contact behaviour", *Minerals, Mining, Materials Wide Gap Semiconductors Workshop*, Copper Mountain, CO, USA, Apr., 2000.

[16] M. Scherer, A. Pelzmann, V. Schwegler, C. Kirchner, M. Seyboth, and M. Kamp, "GaN related research at University of Ulm", *Seminar*, US Army Research Laboratory, Adelphi, MD, USA, Apr., 2000.

[17] T. Ackemann, S. Barland, M. Giudice, J.R. Tredicce, R. Jäger, M. Grabherr, M. Miller, and K.J. Ebeling, "Spatial structures in vertical-cavity semiconductor amplifiers", *Nonlinear Optics and Excitation Kinetics in Semiconductors, NOEKS 2000*, Marburg, Germany, Apr., 2000.

Publications and Conference Contributions

[1] K.J. Ebeling, R. King, M. Kicherer, F. Mederer, H. Unold, J. Joos, R. Jäger, I. Ecker, and M. Golling, "Low-noise high-speed VCSELs and arrays for optical interconnects", in Proc. *Int. Symp. on Ultra-Parallel Optoelectronics*, Kawasaki, Japan, Feb., 2000.

[2] K.J. Ebeling, F. Mederer, H. Unold, T. Knödl, M. Kicherer, M. Golling, R. Jäger, and R. Michalzik, "High performance VCSELs for optical data links", in Proc. *Fifth Optoelectronics and Communications Conf., OECC 2000*, pp. 518–519, Makuhari Messe, Chiba, Japan, July, 2000.

[3] K.J. Ebeling, M. Miller, M. Grabherr, R. Jäger, M. Kicherer, and F. Mederer, "High-power vertical-cavity surface emitting laser diodes", in Proc. *10th Conference on Laser Optics,* (invited), St. Petersburg, Russia, June, 2000.

[4] K.J. Ebeling, F. Mederer, H. Unold, T. Knödl, M. Kicherer, M. Golling, R. King, R. Jäger, I. Ecker, J. Joos, D. Wiedenmann, and R. Michalzik, "High speed modulation of VCSELs for optical data transmission", in Proc. *Topical Meeting on Semiconductor Microcavity Photonics 2000*, Monte Verità, Ascona, Switzerland, Oct., 2000.

[5] K.J. Ebeling, "VCSELs: Prospects and challenges for optical interconnects", in Proc. *IEEE Lasers and Electro-Optics Society Annual Meeting, LEOS 2000,* (invited), pp. 7–8, Rio Grande, Puerto Rico, Nov., 2000.

[6] M. Grabherr, M. Miller, R. Jäger, and K.J. Ebeling, "VCSELs show up in the Watt regime", in Proc. *COST, European VCSEL Workshop*, p. A1, Brussels, Belgium, Sept., 2000.

[7] J. Joos, F. Mederer, M. Kicherer, I. Ecker, R. Jäger, W. Schmid, M. Grabherr, and K.J. Ebeling, "2.5-Gbit/s data transmission over 10 km standard single-mode fiber using InGaAs VCSELs at 1.13 μm emission wavelength", *IEEE Photon. Technol. Lett.*, vol. 12, pp. 344–346, 2000.

[8] J. Joos, I. Ecker, and K.J. Ebeling, "Low threshold GaAsSb/GaAs broad area laser diodes emitting at 1220 nm", in Proc. *Conference on Lasers and Electro-Optics Europe, CLEO/Europe 2000*, p. 39, Nice, France, Sept., 2000.

[9] M. Kamp and H. Riechert, "MBE growth of GaN and related compounds", (Book Chapter) in *Properties of GaN and Related Compounds,* J.H. Edgar (ed.), *INSPEC Datas Review Series*, pp. 426–439, 2000.

[10] M. Kamp, "Solutions for heteroepitaxial growth of GaN and their impact on devices", *Optical and Quantum Electronics,* (invited), vol. 32, pp. 227–248, 2000.

[11] M. Kicherer, D. Wiedenmann, and K.J. Ebeling, "High speed phenomena in vertical-cavity surface-emitting laser diodes", *Nonlinear Optics*, vol. 25, pp. 215–222, 2000.

[12] M. Kicherer, R. Jäger, R. King, F. Mederer, H.J. Unold, and K.J. Ebeling, "Single- and multimode VCSELs for 12.5 Gb/s data links", in Proc. *Conference on Lasers and Electro-Optics Europe, CLEO/Europe 2000*, p. 73, Nice, France, Sept., 2000.

[13] M. Kicherer, F. Mederer, R. Jäger, H.J. Unold, K.J. Ebeling, S. Lehmacher, A. Neyer, and E. Griese, "Data transmission at 3 Gbit/s over intraboard polymer waveguides with GaAs VCSELs", in *Proc. European Conference on Optical Communication, ECOC 2000*, vol. 3, pp. 289–290, Munich, Germany, Sept., 2000.

[14] M. Kicherer, F. Mederer, H.J. Unold, K.J. Ebeling, S. Lehmacher, E. Griese, and M. Naritomi, "VCSEL based high-speed data transmission over polymer optical fibers and circuit board integrated waveguides", in Proc. *Int. Optical Symp.,* (invited), vol. 55, pp. 7–8, Kyoto, Japan, June, 2000.

[15] C. Kirchner, V. Schwegler, F. Eberhard, M. Kamp, K.J. Ebeling, P. Prystawko, M. Leszczynski, I. Grzegory, and S. Porowski, "MOVPE homoepitaxy of high-quality GaN: crystal growth and devices", *Progress in Crystal Growth and Characterization of Materials,* (invited), pp. 57–83, 2000.

[16] T. Knödl, R. Jäger, M. Golling, M. Miller, and K.J. Ebeling, "Improvement of diode cascade VCSEL performance", in Proc. *Conference on Lasers and Electro-Optics Europe, CLEO/Europe 2000*, p. 346, Nice, France, Sept., 2000.

[17] S.W.Z. Mahmoud, H.J. Unold, W. Schmid, and K.J. Ebeling, "Analysis of longitudinal lasing modes in long cavity VCSELs", in Proc. *Semiconductor and Integrated Optoelectronics, SIOE 2000*, Cardiff, United Kingdom, Apr., 2000.

[18] F. Mederer, R. Jäger, P. Schnitzer, H. Unold, M. Kicherer, K.J. Ebeling, M. Naritomi, and R. Yoshida, "Multi-Gigabit/s graded-index POF data link with butt-coupled single-mode InGaAs VCSEL", *IEEE Photon. Technol. Lett.*, vol. 12, pp. 199–201, 2000.

[19] F. Mederer, M. Kicherer, H. Unold, and K.J. Ebeling, "2.5 Gbit/s data transmission with single-mode GaAs VCSELs over a −20°C to 100°C temperature range", *Electron. Lett.*, vol. 36, pp. 236–238, 2000.

[20] F. Mederer, M. Grabherr, F. Eberhard, I. Ecker, R. Jäger, J. Joos, C. Jung, M. Kicherer, R. King, P. Schnitzer, H. Unold, D. Wiedenmann, and K.J. Ebeling, "High performance selectively oxidized VCSELs and arrays for parallel high-speed optical interconnects", *Advances in Solid State Physics, Vieweg, Braunschweig*, vol. 40, pp. 611–625, 2000.

[21] F. Mederer, R. Jäger, P. Schnitzer, H. Unold, M. Kicherer, K.J. Ebeling, M. Naritomi, and R. Yoshida, "High performance selectively oxidized VCSEL arrays for parallel, high-speed optical interconnects", in Proc. *Electronic Components and Technology Conference, ECTC 2000*, pp. 1242–1251, Las Vegas, NV, USA, May, 2000.

[22] F. Mederer, M. Kicherer, R. Jäger, H. Unold, and K.J. Ebeling, "5 Gbit/s data transmission with single-mode GaAs VCSELs over a 0°C to 80°C temperature range", in Proc. *European Conference on Optical Communication, ECOC 2000*, vol. 2, pp. 65–66, Munich, Germany, Sept., 2000.

[23] F. Mederer, R. Michalzik, and K.J. Ebeling, "High-speed parallel optical interconnects based on vertical-cavity surface-emitting lasers", *Compound Semiconductor Magazine*, vol. 6, pp. 60–64, 2000.

[24] F. Mederer, R. Jäger, M. Kicherer, H. Unold, and K.J. Ebeling, "GaAs-basierende VCSELs für hochbitratige optische Datenübertragung", in Proc. *Frühjahrstagung der DPG e.V.*, vol. HL 29.1, p. 557, Regensburg, Germany, Mar., 2000.

[25] F. Mederer, M. Grabherr, R. Jäger, J. Joos, M. Kicherer, R. Michalzik, H. Unold, and K.J. Ebeling, "VCSELs for the optical data transmission to PCB-integrated waveguides", in Proc. *Selected Optoelectronic Components and Functional Optical Structures for the Use in Electronics and Sensory Technique*, Dresden, Germany, July, 2000.

[26] R. Michalzik, R. King, G. Giaretta, R. Jäger, and K.J. Ebeling, "VCSEL arrays for 10 Gb/s multimode fiber optical interconnects", in *Optoelectronic Interconnects VII, SPIE Proc.,* (invited), vol. 3952, pp. 124–133, Jan., 2000.

[27] R. Michalzik, G. Giaretta, K.W. Goossen, J.A. Walker, and M.C. Nuss, "40 Gb/s coarse WDM data transmission with 825 nm wavelength VCSELs over 320 m of high-performance multimode fiber", in Proc. *European Conference on Optical Communication, ECOC 2000*, vol. 4, pp. 33–34, Munich, Germany, Sept., 2000.

[28] M. Miller, M. Grabherr, R. Jäger, and K.J. Ebeling, "kW/cm^2 VCSEL array for high power applications", in *Vertical Cavity Surface Emitting Lasers IV, SPIE Proc.*, vol. 3946, pp. 198–206, San Jose, CA, USA, Jan., 2000.

[29] M. Miller, M. Grabherr, R. Jäger, H.J. Unold, and K.J. Ebeling, "Large-area high-power VCSEL", in Proc. *IEEE International Semiconductor Laser Conference*, pp. 63–64, Monterey, CA, USA, Sept., 2000.

[30] M. Scherer, M. Seyboth, V. Schwegler, and M. Kamp, "Dry etching influence on contact formation to gallium nitride", in Proc. *10th European Heterostructure Technology Workshop*, Günzburg, Germany, Sept., 2000.

[31] W. Schmid, F. Eberhard, R. Jäger, R. King, M. Miller, J. Joos, and K.J. Ebeling, "45 % quantum-efficiency light-emitting diodes with radial outcoupling taper", in *Light-Emitting Diodes: Research, Manufacturing, and Applications IV, SPIE Proc.*, vol. 3938, pp. 90–97, San Jose, CA, USA, Jan., 2000.

[32] V. Schwegler, M. Seyboth, C. Kirchner, M. Scherer, M. Kamp, P. Fischer, J. Christen, and M. Zacharias, "Spatially resolved electroluminescence of InGaN-MQW-LEDs", *MRS Internet J. Nitride Semicond. Res.*, vol. 5S1, p. W1.6, 2000.

[33] V. Schwegler, M. Seyboth, S.S. Schadt, M. Scherer, C. Kirchner, M. Kamp, U. Stempfle, W. Limmer, and R. Sauer, "Temperature distribution in InGaN-MQW LEDs under operation", *MRS Internet J. Nitride Semicond. Res.*, vol. 5S1, p. W11.18, 2000.

[34] P. Unger, "Integration of high-power semiconductor lasers using dry-etched mirrors", in Proc. *Ist Joint Symposium on Opto- and Microelectronic Devices and Circuits*, pp. 77–80, Nanjing, China, Apr., 2000.

[35] P. Unger, "Introduction to power diode lasers", (Book Chapter) in *High-Power Diode Lasers–Fundamentals, Technology, Applications,* Berlin, Springer-Verlag, vol. 78, pp. 1–53, 2000.

[36] H.J. Unold, S.W.Z. Mahmoud, F. Eberhard, R. Jäger, and K.J. Ebeling, "Large-area single-mode selectively oxidized VCSELs: approaches and experimental", in *Vertical Cavity Surface Emitting Lasers IV, SPIE Proc.*, vol. 3946, pp. 207–218, San Jose, CA, USA, Jan., 2000.

[37] H.J. Unold, S.W.Z. Mahmoud, R. Jäger, M. Kicherer, M.C. Riedl, and K.J. Ebeling, "Improving single-mode VCSEL performance by introducing a long monolithic cavity", *IEEE Photon. Technol. Lett.*, vol. 12, pp. 939–941, 2000.

[38] H.J. Unold, M. Kicherer, S.W.Z. Mahmoud, R. Jäger, R. Michalzik, and K.J. Ebeling, "Spatially varied anti-resonant DBR design for large-area single-mode VCSELs", in Proc. *IEEE International Semiconductor Laser Conference*, pp. 57–58, Monterey, CA, USA, Sept., 2000.

[39] T. Ackemann, S. Barland, M. Cara, S. Balle, J.R. Tredicce, R. Jäger, M. Grabherr, M. Miller, and K.J. Ebeling, "Spatial mode structure of bottom-emitting broad-area vertical-cavity surface-emitting lasers", *J. Opt. B: Quantum Semiclass. Opt.*, vol. 2, pp. 406–412, 2000.

[40] T. Ackemann, S. Barland, M. Giudice, J.R. Tredicce, S. Balle, R. Jäger, M. Grabherr, M. Miller, and K.J. Ebeling, "Patterns in broad-area microcavities", *Phys. Stat. Sol. (b)*, vol. 221, pp. 133–136, 2000.

[41] T. Ackemann, S. Barland, J.R. Tredicce, M. Cara, S. Balle, R. Jäger, M. Grabherr, M. Miller, and K.J. Ebeling, "Spatial structure of broad-area vertical-cavity regenerative amplifiers", *Opt. Lett.*, vol. 25, pp. 814–816, 2000.

[42] C. Affolderbach, A. Nagel, S. Knappe, C. Jung, D. Wiedenmann, and R. Wynands, "Nonlinear spectroscopy with a vertical-cavity surface-emitting laser (VCSEL)", *Appl. Phys. B: Lasers and Optics*, vol. 70, pp. 407–413, 2000.

[43] P. Fischer, J. Christen, M. Zacharias, V. Schwegler, C. Kirchner, and M. Kamp, "Spatially resolved imaging of the spectral emission characteristic of an InGaN/GaN-MQW-light-emitting diode by scanning electroluminescence microscopy", *Jpn. J. Appl. Phys.*, vol. 39, pp. 2414–2416, 2000.

[44] G. Giaretta, R. Michalzik, and A.J. Ritger, "Long distance (2.8 km), short wavelength (0.85 μm) data transmission at 10 Gb/sec over new generation high bandwidth multi-mode fiber", in *Conference on Lasers and Electro-Optics, CLEO 2000,* postdeadline paper CPD13, San Francisco, CA, USA, May, 2000.

[45] J.-P. Hermier, I. Maurin, E. Giacobino, P. Schnitzer, R. Michalzik, K.J. Ebeling, A. Bramati, and A.Z. Khoury, "Quantum noise in VCSELs", *New Journal of Physics*, vol. 2, pp. 26.1–26.13, 2000.

[46] A. Oster, M. Zorn, H.J. Unold, J. Sebastian, H. Wenzel, W. John, M. Weyers, and G. Tränkle, "Development of 650 -emitting VCSELs for cw operation", in Proc. *COST, European VCSEL Workshop*, p. L2, Brussels, Belgium, Sept., 2000.

[47] A. Oster, M. Zorn, H.J. Unold, J. Sebastian, H. Wenzel, W. John, M. Weyers, and G. Tränkle, "Development of 650 nm-emitting VCSELs for cw operation", in *27th International Symposium of Compound Semiconductors 2000*, Oct., 2000.

[48] G. Salviati, N. Armani, C. Zanotti-Fregonara, E. Gombia, M. Albrecht, H. Strunk, M. Mayer, M. Kamp, and A. Gasparotto, "Deep level related yellow luminescence in p-type GaN grown by MBE on (0001) sapphire", *MRS Internet J. Nitride Semicond. Res.*, vol. 5S1, p. W11.50, 2000.

Submitted Publications and Conference Contributions

[1] E. Deichsel, F. Eberhard, R. Jäger, and P. Unger, "High-power laser diodes with dry-etched mirror facets and integrated monitor photodiodes", *IEEE J. Selected Topics Quantum Electron.*, 2001, in press.

[2] M. Golling, T. Knödl, A. Straub, M. Kicherer, and K.J. Ebeling, "Optimization strategies for diode cascade InGaAs VCSELs", in *Vertical Cavity Surface Emitting Lasers V, SPIE Proc.*, vol. 4286, San Jose, CA, USA, Jan., 2001.

[3] M. Kamp, A. Pelzmann, C. Kirchner, M. Mayer, and K.J. Ebeling, "Progress in GaN homoepitaxy", *Semiconductor Science and Technology,* (invited), 2001, in press.

[4] R. King, R. Michalzik, R. Jäger, and K.J. Ebeling, "32-VCSEL channel CMOS-based transmitter module for Gb/s data rates", in *Vertical Cavity Surface Emitting Lasers V, SPIE Proc.*, vol. 4286, San Jose, CA, USA, Jan., 2001.

[5] T. Knödl, M. Golling, A. Straub, and K.J. Ebeling, "Multi-diode cascade VCSEL with 130 % differential quantum efficiency at cw room temperature operation", *Electron. Lett.*, vol. 37, pp. 31–33, 2001.

[6] T. Knödl, A. Straub, M. Golling, and K.J. Ebeling, "Scaling behavior of bipolar cascade VCSELs", *IEEE Photon. Technol. Lett.*, 2001, submitted.

[7] F. Mederer, R. Jäger, H.J. Unold, A. Cheleg, R. Michalzik, K.J. Ebeling, S. Lehmacher, A. Neyer, and E. Griese, "Data transmission at 3 Gbit/s over PCB integrated polymer waveguides with GaAs VCSELs", *IEEE Photon. Technol. Lett.*, 2001, submitted.

[8] F. Mederer, R. Jäger, J. Joos, M. Kicherer, R. Michalzik, M. Riedl, H. Unold, A. Cheleg, and K.J. Ebeling, "Improved VCSEL structures for 10 Gigabit-Ethernet and next generation optical-integrated PC-boards", in Proc. *Electronic Components and Technology Conference, ECTC 2001*, May, 2001, in press.

[9] R. Michalzik, F. Mederer, R. King, M. Kicherer, R. Jäger, and K.J. Ebeling, "Very short reach optical interconnect applications of vertical-cavity surface-emitting laser diodes", *Kleinheubacher Berichte*, vol. 44, 2001, in press.

[10] R. Michalzik, R. King, F. Mederer, M. Kicherer, G. Giaretta, and K.J. Ebeling, "Short-wavelength VCSEL applications: from high throughput multimode fiber links to two-dimensional interchip interconnections", *Opt. Eng.*, vol. 40, 2001, in press.

[11] R. Michalzik, K.J. Ebeling, M. Kicherer, F. Mederer, R. King, H. Unold, and R. Jäger, "High-performance VCSELs for optical data links", *IEICE Trans. Electron.,* (invited), vol. E84-C, 2001, in press.

[12] M. Miller, M. Grabherr, R. Jäger, and K.J. Ebeling, "High-power VCSEL array for emission in the Watt regime at room temperature", *IEEE Photon. Technol. Lett.*, 2001, in press.

[13] M. Miller, M. Grabherr, R. King, R. Jäger, R. Michalzik, and K.J. Ebeling, "Improved output performance of high-power VCSELs", *IEEE J. Selected Topics Quantum Electron.*, 2001, in press.

[14] M. Scherer, V. Schwegler, M. Seyboth, C. Kirchner, M. Kamp, A. Pelzmann, and M. Drechsler, "Low resistive GaN using 2-step rapid thermal annealing processes", *Appl. Phys. Lett.*, 2001, submitted.

[15] W. Schmid, M. Scherer, R. Jäger, P. Strauß, K. Streubel, and K.J. Ebeling, "Efficient light-emitting diodes with radial outcoupling taper at 980 and 630 nm emission wavelength", in *Light-Emitting Diodes: Research, Manufacturing, and Applications V, SPIE Proc.*, vol. 4278, San Jose, CA, USA, Jan., 2001.

[16] H.J. Unold, S.W.Z. Mahmoud, R. Jäger, M. Grabherr, R. Michalzik, and K.J. Ebeling, "Large-area single-mode VCSELs and the self-aligned surface relief", *IEEE J. Selected Topics Quantum Electron.*, 2001, in press.

[17] H.J. Unold, M.C. Riedl, S.W.Z. Mahmoud, R. Jäger, and K.J. Ebeling, "Long monolithic cavity VCSEL for single-mode output power", *Electron. Lett.*, vol. 37, pp. 178–179, 2001.

[18] I. Daumiller, C. Kirchner, M. Kamp, K.J. Ebeling, J. Off, F. Scholz, and E. Kohn, "Material requirements for high temperature GaN based heterojunction FETs", *Mat. Sci. Eng. B*, 2001, submitted.

[19] I. Daumiller, C. Kirchner, M. Kamp, K.J. Ebeling, L. Pond, C.E. Wetzel, and E. Kohn, "Evaluation of AlGaN/GaN HFETs up to 750 °C", *Electron. Device Lett.*, 2001, submitted.

[20] J.-P. Hermier, A. Bramati, A.Z. Khoury, V. Josse, E. Giacobino, P. Schnitzer, R. Michalzik, and K.J. Ebeling, "Noise characteristics of oxide confined vertical-cavity surface emitting lasers", *IEEE J. Quantum Electron.*, vol. 37, pp. 89–91, 2001.

[21] M.B. Willemsen, A.S. van de Nes, M.P. van Exter, J.P. Woerdman, M. Kicherer, R. King, R. Jäger, and K.J. Ebeling, "Polarization-resolved linewidth-power product of a VCSEL", *Appl. Phys. Lett.*, 2001, submitted.